JRA4

BSMEM Test Report

Authors:
Fabien Baron <baron@mrao.cam.ac.uk> — University of Cambridge

Author: Fabien Baron	Signature:
Institute: University of Cambridge	Date: 04/10/2007
Approved by: Gilles Duvert	Signature:
Institute: LAOG/JMMC	Date: 10/10/2007
Released by: Gilles Duvert	Signature:
Institute: LAOG/JMMC	Date: 10/10/2007

Change record

Revision	Date	Authors	Sections/Pages affected
	Remarks		
1	20/12/2006	F. Baron	all
	Initial writing		

Table of contents

1 Introduction

1.1 Object

This document is part of the Cambridge image reconstruction software review. Its final purpose is to guide interferometer users to understand which level of confidence they should put into their MEM reconstructed images, and to guide them with BSMEM to achieve overall better performance.

We present here a test plan aiming at determining MEM code robustness for various representative difficult data sets, as well as the results of the related simulations.

1.2 Reference documents

[1] Gull, S. F. and Skilling, J., 'Quantified Maximum Entropy - Memsys5 Users' Manual', Maximum Entropy Data Consultants Ltd., South Hill, 42 Southgate Street, Bury St. Edmunds, IP33 2AZ, United Kingdom (1991).

[2] Buscher , D. F., 'Direct maximum-entropy image reconstruction from the bispectrum', in IAU Symp. 158: Very High Angular Resolution Imaging, Robertson, J. G. and Tango, W. J., eds., pp. 91 (1994).

[3] Lawson, P. R. et al., 'An interferometry imaging beauty contest', in New Frontiers in Stellar Interferometry, Proceedings of SPIE Volume 5491, Wesley A. Traub, ed., Bellingham, WA: The International Society for Optical Engineering, pp. 886 (2004).

[4] Lawson, P. R. et al., 'The 2004 Optical/IR Interferometry Imaging Beauty Contest', Bulletin of the American Astronomical Society, pp 1605 (2004).

[5] Thorsteinsson, H. and Buscher, D. F. and Young, J. S., 'The bispectrum in model-independent imaging', New Frontiers in Stellar Interferometry, Proceedings of SPIE Volume 5491. Edited by Wesley A. Traub. Bellingham, WA: The International Society for Optical Engineering, pp.1574 (2004).

[6] Lawson, P. R. et al., '2006 interferometry imaging beauty contest', in Advances in Stellar Interferometry, Monnier, John D.; Schöller, Markus; Danchi, William C.., eds., Proceedings of the SPIE, Volume 6268 (2006).

2 Presentation of Cambridge interferometry software package

The Cambridge image reconstruction package includes several interdependent softwares:

- BSMEM: image reconstruction;

- OBSTRAT and BSFAKE: fake observation/image simulation;

- BSTESTS: statistics tools developed specifically to test BSMEM on fake data.

2.1 BSMEM, the image reconstruction software

Cambridge software package has been dubbed BSMEM to stand for BiSpectrum Maximum Entropy Method. It was first written in Fortran and completed by David Buscher in 1992 to demonstrate direct maximum entropy reconstruction from optical aperture synthesis data [2]. BSMEM applies a fully Bayesian approach to the inverse problem of finding the most probable image given the evidence. BSMEM makes use of the MEMSYS library (from Maximum Entropy Data Consultants Ltd., www.maxent.co.uk) to implement a gradient descent algorithm for maximising the inference of an image. If the imaging equation is:

$$\boldsymbol{D} = \boldsymbol{RI} + \boldsymbol{\sigma} \tag{1}$$

where $\boldsymbol{I} = \boldsymbol{I}_1, ... \boldsymbol{I}_N$ is the image to reconstruct, $\boldsymbol{D} = \boldsymbol{D}_1, ... \boldsymbol{D}_M$ the data, $\boldsymbol{R}$ the instrumental model, and $\boldsymbol{\sigma}$ the noise, then Bayes's equation is:

$$\Pr(\boldsymbol{I}|\boldsymbol{D}) = \frac{\Pr(\boldsymbol{I})\Pr(\boldsymbol{D}|\boldsymbol{I})}{\Pr(\boldsymbol{D})} \tag{2}$$

where $\Pr(\boldsymbol{I}|\boldsymbol{D})$ is the posterior probability density (also called inference), $\Pr(\boldsymbol{D}|\boldsymbol{I})$ is the likelihood, $\Pr(\boldsymbol{I})$ the prior, and $\Pr(\boldsymbol{D})$ the evidence. In the case where $\boldsymbol{\sigma}$ is uncorrelated Gaussian noise, which we will assume here, the likelihood is:

$$\Pr(\boldsymbol{D}|\boldsymbol{I}) \propto \exp - \left\{ \sum_{n=1}^{N} \left(\frac{\boldsymbol{D}_n - (\boldsymbol{RI})_n}{2\sigma_n} \right)^2 \right\} = \exp\left\{ -\frac{\chi^2}{2} \right\} \tag{3}$$

where χ^2 is the usual RMS statistic. The prior is also shown to take the form:

$$\Pr(\boldsymbol{D}|\boldsymbol{I}) \propto \exp\left\{ \alpha H(\boldsymbol{I}) \right\} \tag{4}$$

so that maximising the inference becomes a problem of minimising the criterion:

$$J(\boldsymbol{I}) = \frac{\chi^2}{2} - \alpha H(\boldsymbol{I}) \tag{5}$$

where is α is called the regularization constant and H the prior function. The MEM approach considers prior functions which measure the entropy of the image. Maximising the entropy minimises the information contained in the reconstructed image, which in turn maximises the probability of having this image observed. There are several entropy function H used in the literature. BSMEM uses the Gull and Skilling one [1]:

$$H(\boldsymbol{I}) = \sum_{k=1}^{N} (\boldsymbol{I}_k - \boldsymbol{M}_k) - \boldsymbol{I}_k \ln(\frac{\boldsymbol{I}_k}{\boldsymbol{M}_k}) \tag{6}$$

where $\boldsymbol{M}$ is a given model. A flat or Gaussian model is generally used, though a user-made starting model can be defined by directly drawing in over the reconstructed image. In practise BSMEM reconstructions are nonetheless considered model-independent (see section 4.4). Note that this entropy function can be seen as the sum of two terms, one being the total flux difference between the reconstructed image and the model, and the other a Kullback-Leibler divergence between image and model.

The balance between the χ^2 and the entropy function depends on α, which takes a cut-off Jeffreys prior form:

$$\Pr(\alpha) = \frac{2\alpha_0}{\pi(\alpha^2 + \alpha_0^2)} \tag{7}$$

where α_0 is chosen to maximise the evidence $\Pr(\boldsymbol{D}|\alpha)$. The regularization constant is automatically estimated during the reconstruction, and J is then minimised using a conjugate gradient method without any kind of user supervision.

BSMEM has several advantages over its predecessors. The phase self-calibration procedure applied more conventionally in interferometry fails in most cases where the data is mostly composed of the powerspectrum with only a very few bispectrum points, as it relies on the bispectrum and powerspectrum components sharing common uv points. On the contrary BSMEM independently exploits the powerspectrum points, the triple product amplitudes, and the phase closures, it can handle all types of data sparseness (such as the frequent case of missing closures). Contrary to the CLEAN method, it only requires minimal user input, as it relies on an objective stopping criterion to determine whether the reconstruction can be considered as finished or not. Another advantage of BSMEM is its computational cheapness given its reliable treatment of the data. 256 x 256 pixels reconstruction from interferometric data sets of typical medium SNR take currently only a few minutes of processing on a modern computer.

From 2002 to 2006, while the core of the program has remained more or less unchanged, multiple improvements have been brought by H. Thorsteinsson and F. Baron. BSMEM has partly been ported to

C and C++, it has gained compatibility with the OIFITS format, and the reconstruction options and the user interface have been improved and expanded.

The two IAU Interferometry Imaging Beauty Contest, which took place in May 2004 [3, 4] and May 2006 [6] have been welcome opportunities to confront BSMEM to other widely used image reconstruction softwares and understand its strong points and weaknesses. BSMEM has been awarded the Grand Champion status in both installments of the contest. In 2004 the contest data sets were typical sources simulated as if taken from 6 stations (similar to the Navy Prototype Optical Interferometer) with low to medium SNR. BSMEM results have demonstrated good performance when dealing with this kind of data sets. The 2006 contest data sets were very noisy and exhibited poorer *uv* coverage, but BSMEM was still able to reconstruct the object, demonstrating that model independent imaging can be powerful even at low SNR.

However BSMEM is of course not perfect, and suffers from the main drawbacks of the MEM approach : an imperfect photometry, the difficulty to reconstruct both extended and compact sources on the same image, the tendency to smooth the edges of the objects, the absence of spatial correlation in the reconstructed image, and problems to estimate the signal under the background level. Another choice for the entropy function, the introduction of an intrinsic correlation function, and a bi-model approach could be envisioned for the future to improve these points, and Pyramid MEM or Multiscale MEM constitute other alternatives.

2.2 OBSTRAT and BSFAKE, the observation and image simulators

OBSTRAT and BSFAKE programs have the same global objective: to simulate fake data for BSMEM to reconstruct.

OBSTRAT generates fake instrumentation parameters, i.e. the size and layout of the aperture synthesis array and the sub-array size for beam combination. OBSTRAT used to be limited to Y configurations, but it has since been improved for this test plan, in order to accept any type of aperture configuration. OBSTRAT also allows to select a reduced number of independent baseline closures among the maximum possible one to study whether particular combinations of closures are more useful.

BSFAKE is used to define the observation parameters, i.e. the nature and position of the observed target, the number and times of observations, the nature and level of the noise on the visibility amplitudes and visibility phases, from which noises on bispectrum and powerspectrum are derived. Then BSFAKE generates an OIFITS compatible data-set, as well as a image of the target if required.

It should be noted that minor modifications have also been brought to BSFAKE and BSMEM to ease testing. One of the most important is the ability for BSFAKE to generate several OIFITS data files with different noise occurrences, i.e. different noise realization while the main noise levels remain constant. This allows testing the statistical properties such as the repeatability of a reconstruction for a fixed amount of noise.

2.3 BSTESTS, the IDL/scripts test package

The so-called BSTESTS procedures are mostly composed of IDL tools and shell scripts that were developed to specifically test BSMEM. Their objectives are mostly to execute planned scripts, launching BSFAKE/BSMEM with a wide amount of command line parameters. They also allow to compare the reconstructed images to the true image and then provide statistical analysis on these reconstructed images. In particular the bias and Mean Squared Error of the reconstructions are computed, as well as the standard deviations of these errors. All data corresponding to a simulation (except the images) are then collected into an IDL DAT file. Custom IDL export programs then draw the plots and convert them into EPS files. These latters were directly included in this report. Hence the whole process is rather straightforward and easy to automate.

3 Test plan overview

3.1 Objectives of the test plan

The test plan was meant to achieve a better understanding of BSMEM results when confronted to data sets which present one or several characteristics susceptible to make the reconstruction process harder. Namely:

1. low SNR data sets;

2. low uv coverage, as can be found in facilities not primarily intended for imaging;

3. missing bispectrum/powerspectrum data;

4. difficult source morphology, for example a source with an important amount of resolved flux, or special properties of symmetry which may affect the process of reconstruction.

3.2 Testing procedure steps

This section describes step by step the BSTESTS procedure which was followed to evaluate BSMEM, from the creation of the fake data sets needed to review all the previously defined objectives (fake instrument and targets simulation) to the reconstruction and the statistical analysis of the reconstructed images.

3.2.1 Simulation of the observation conditions

Four different array configurations have been used for reconstructions and are presented on figure 1).

The first one is the VLTI configuration with all four UTs telescopes, while others are configurations with more telescopes. Bootstrapping capability is strong advocacy for Y arrays, so such configurations are commonly considered for future interferometers. Hence the 6 telescope configuration is close to what could be obtained with the Magdalena Ridge Observatory Phase A, and VSI is planned to get a 8 telescope configuration. Most interferometers are not especially designed with imaging in mind, so the chosen configurations are not optimised for best imaging performance. On the contrary they are meant to give average and representative results : as a result the uv plane is decently covered for the 6 and 6 telescope arrays, but not too much either.

On the other hand, the 15 telescope case is meant to be the example of an exhaustive coverage of the uv plane. This latter configuration allows to study the importance of the object shape on reconstruction capabilities as the differences arising from the reconstruction process cannot be attributed to a lack of uv coverage but to a genuine MEM behaviour with respect to the object.

All Y configuration possess maximum baselines of about 170 meters, which is slightly greater than the maximum baseline of the VLTI one (about 130 m), but represents well the increased goals for future generation interferometer. The reader will understand that our goal was not to compare the VLTI to another array configuration of the same resolution, but more to a state of the art interferometer, and then determine in which cases the increased uv coverage brings major improvements.

To be consistent with existing instruments, all tests have been run in the near infrared bands ($\lambda \simeq 1.0\mu$m). The typical baseline range for the simulated instruments was around $40-200$m, thus approximatively defining a practical limit between resolved (> 1mas) and unresolved (< 0.1 mas) simulated objects.

The simulated observation strategy consisted in 16 simulated acquisitions every 15 minutes, so 4 hours total time. During each acquisition all available bispectrum and powerspectrum were measured.

3.2.2 Test targets

Six test targets have been selected and are presented in figure 2. Not all of them are meant to be realistic, as they were tailored to give insights about BSMEM behaviour. Some were chosen because it was expected that the overall resolved flux s well as the global symmetry of the object should have a major influence on performance.
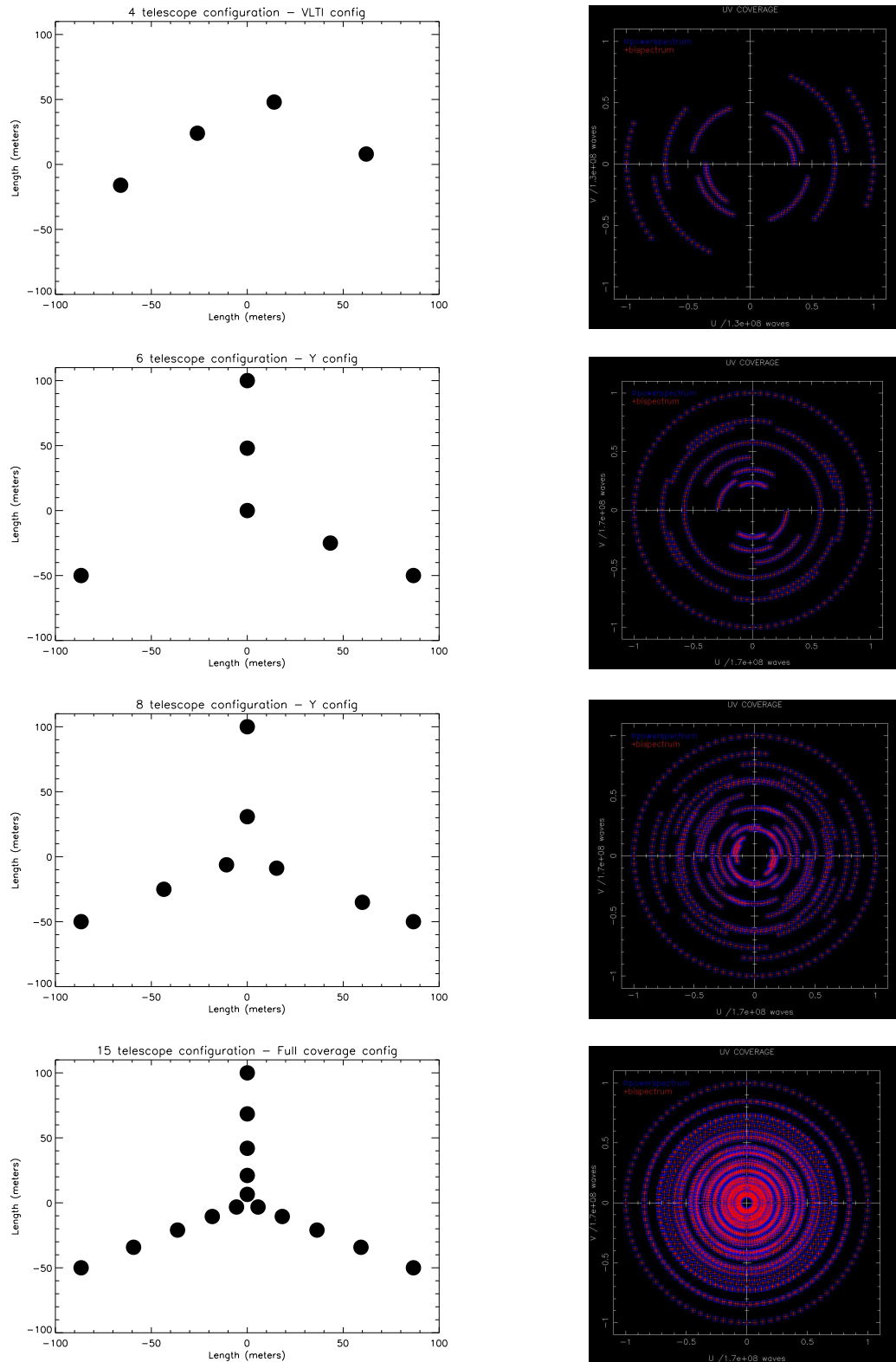
Figure 1: Array configurations and their *uv* coverage. From top to bottom : VLTI configuration, Y configurations with 6, 8, and 15 telescopes.
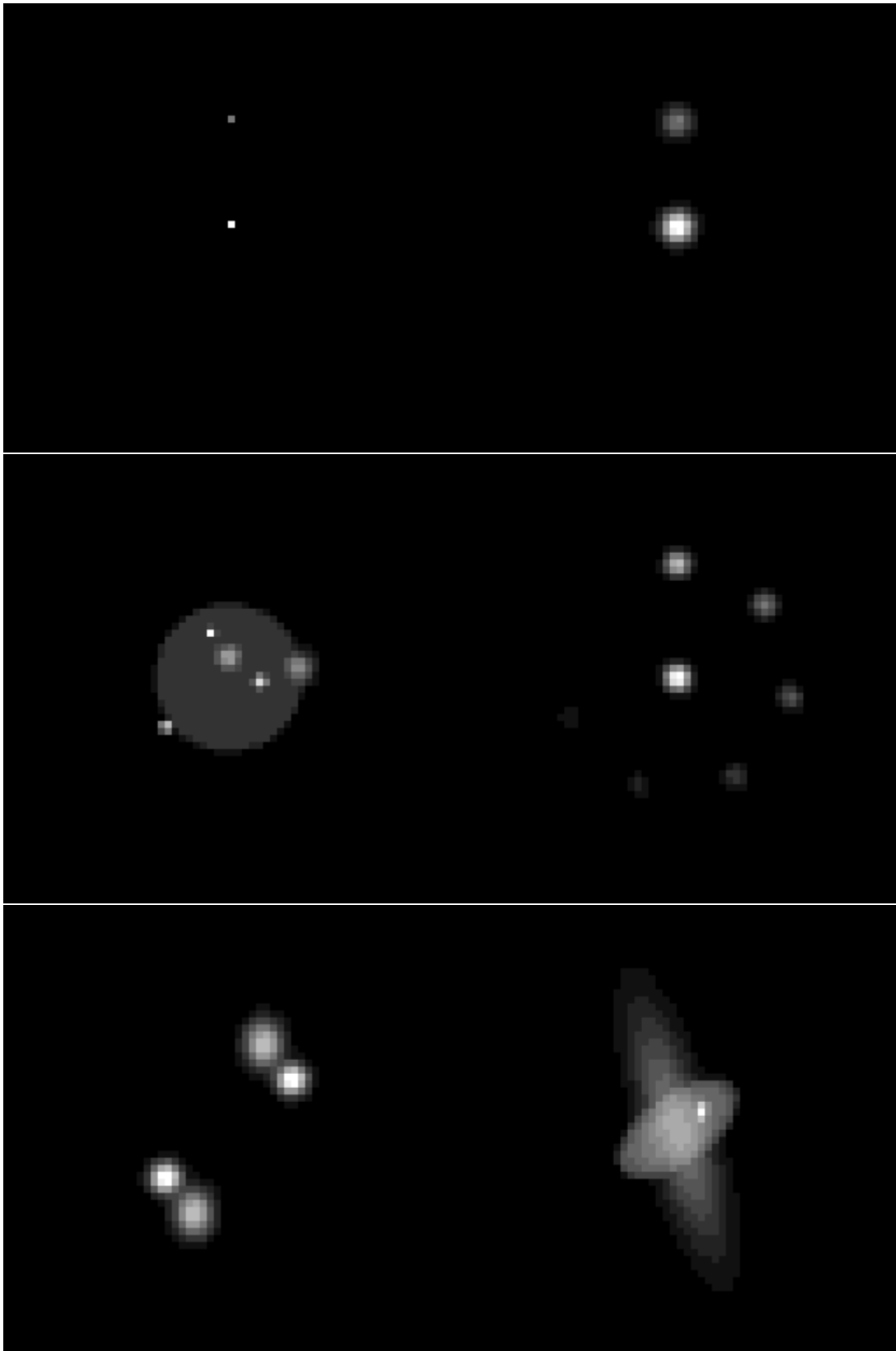
Figure 2: Object test cases : simple unresolved binary, simple resolved binary, asymmetric stellar disk, seven stars, symmetric stars, slightly asymmetric disk.

1. Object 1 is the simplest test case, an unresolved binary (Dirac functions) of flux ratio 1:5, separation 3 mas. This will be the reference *"easy"* object.

2. Object 2 is a resolved binary of flux ratio 1:5, same size 0.5 mas (Gaussian functions), and separation 3 mas.

3. Object 3 is a a typical object, a stellar disk (background totally resolved component) with several slightly resolved spots on it.

4. Object 4 is a object composed of seven resolved (0.4 mas) sources of different fluxes. With the brightest star taken as reference, the flux ratios are 50%, 20%, 10%, 5%, 2%, 1%. This is consequently a test case which allows very simply to check the photometric capability of the reconstruction.

5. Object 5 is a simple example of a perfectly point symmetric object.

6. Object 6 is almost symmetrical, except for a star component. This is an interesting case when dealing with situations where the symmetric part of the object is well reconstructed but not the asymmetric one.

3.2.3   Data and image simulation

Once the test target has been selected, target visibilities are straightforwardly computed for *uv* points derived from the telescope configuration and the observation time.

Then these visibilities are used to derive the powerspectrum and bispectrum data. Furthermore, noise is added to these last quantities. In practice, there are two independent types of noise on the data sets created by BSMEM: noise on visibility amplitudes, and noise on visibility phases. Consequently all studies had to consider these noises either independently (noise tests, section 4.1) or by supposing average values for both noise levels (powerspectrum/bispectrum coverage tests, section 4.2). As long baseline data do have poorer SNR than shorter ones, BSFAKE was configured to reproduce this behaviour.

For each data sets, OBSTRAT and BSFAKE procedures have been used to to simulate a large number ($\simeq 50 - 100$) of fake observations, each differing by its noise realization. One observation consisted of one OIFITS data file and one simulated reference image (or "true image") without noise.

3.2.4   Image reconstruction

The OIFITS file is then given as input to BSMEM, which reconstructs an image using the MEM entropy method. Excluding the data sets characteristics (noise level, *uv* coverage, etc.), reconstruction parameters that have a major influence one the final performance are the following:

- the entropy method. Several entropy methods are available in MEMSYS. However as we will show in section 4.3, the default entropy method is generally sufficient.

- the sampling and size of the reconstructed image: convergence speed and of course precision of the reconstruction are affected by those parameters. A satisfying automatic mode has been implemented into BSMEM by default.

- the stopping criterion. The iterative loops stops when either the user-defined maximum number of iteration is reached, or when a user defined stopping criterion is met. The default stopping criterion is based on MEMSYS internal variables and determines when the reconstructed entropy cloud matches the data one.

- the starting model. It acts as a weighted constraint on the image to be reconstructed. Typical examples are a flat starting model and Gaussian distribution centred in the field. While one of BSMEM goals is to be usable as a model independent software, an adequate starting model is sometimes necessary to converge faster. For very low SNR date, when the reconstruction fails with a generic starting model,

it can succeed with a more constraining model. This underlines the importance of having at least an initial idea of the target morphology.

3.2.5   Process of evaluation of reconstructed images

The fidelity of the reconstructed images to the reference image is analysed by the IMGDIFF routine from BSTESTS package:

- first both the reconstructed and the reference images are aligned by cross-correlation;

- the zones fit for comparison (rectangular and of the same size) are extracted from both images ;

- the extracted zones are normalised;

- the error of the reconstruction is computed and output to a storage file;

- if several images are passed, the standard deviation is also computed and added to the file;

- this file can then processed to create a graphic plot.

3.2.6   Statistics and graphical outputs

As we underlined previously, several noise occurrences have been generated to allow for a statistical study of BSMEM behaviour.

The main reason is that a decent number of noise realizations is necessary to determine the average performance on each data set. For each image the normalised Mean Squared Error of the reconstructed image $\widehat{I}$ versus the true image I is computed as follows :

$$MSE = \frac{\sum\limits_{k=1}^{N} (I - \widehat{I})^2}{\sum\limits_{k=1}^{N} I^2} \tag{8}$$

Then the error is given in percentage by $error = \sqrt{MSE} * 100$: an error of 100% means the reconstructed image is as far from the image as a null image, so that the reconstruction was probably not successful. Errors at about 20 to 50% generally denote a successful reconstruction in the sense it possesses some features also present on the target, and lower errors indicate a nearly flawless reconstruction.

When considering a whole data set, composed of images only differing by their noise occurrences, the actual error is computed as the square root of the averaged MSE.

Several noise realizations are also needed to compute the standard deviation of a set. For all parameters fixed, the standard deviation of the individual errors measures the repeatability of the algorithm at a determined noise level. Thus this constitutes a good indicator of the confidence the user can have in the reconstruction at this noise level :the lower the standard deviation, the more trustworthy the reconstruction is. This repeatability will be plotted beside the error, but will also appear as error bars on the error plots.

It can occur that MEM algorithm was not convergent, and that sometimes its internal routines got NaN values on variables which are critical for the converging process. In such cases the iteration process was automatically stopped, and the current reconstructed image was the one considered for error computation.

Finally, as BSTESTS is being mostly written in IDL, all IDL supported formats can be used to export graphics, most noteworthy are PNG, GIF and EPS formats. The EPS format was selected for this report.

4   Test results

4.1   Noise tests

Noise is obviously the most influential factor on reconstruction performance. This section aims at determining the importance of noise when reconstructing the test objects with our set of telescopes.

4.1.1 Noise levels : definition

BSFAKE allows the creation of simulated data sets with two noise parameters : the noise on visibility amplitudes, and the noise on visibility phases. We will show how BSMEM behaves with low noise on visibility but high noise on closure phase, and in the reverse case.

We can roughly define qualitative noise levels (on the shortest baselines) on a typical object of reference (object 1) for an interferometer, and then interpret the noise parameters of BSFAKE accordingly.

Noise levels are :

- Highest possible SNR: this would be useful if we were interested by maximum theoretical achievable performance. Unfortunately MEM currently has trouble with nearly noiseless data sets due to a bug in MEMSYS library. In practise we will assume 0.2% powerspectrum errors and 0.06° closure phase errors, corresponding to noise parameters of about 10^{-4} on visibility amplitudes and phases.

- High SNR: $1 - 2\%$ visibility errors, $1 - 2°$ closure phase errors (0.002 on visibility amplitudes and phases);

- Medium SNR: $5 - 10\%$ visibility errors, $5 - 10°$ closure phase errors (0.02 to 0.05 on visibility amplitudes and phases) ;

- Low SNR: visibility errors $\geq 15 - 20\%$, closure phase errors $\geq 20 - 30°$ (0.05 or higher on visibility amplitudes and phases).

Note that the longest baselines of the configuration will be assigned a poorer SNR in the simulation, as expected in a real interferometer.

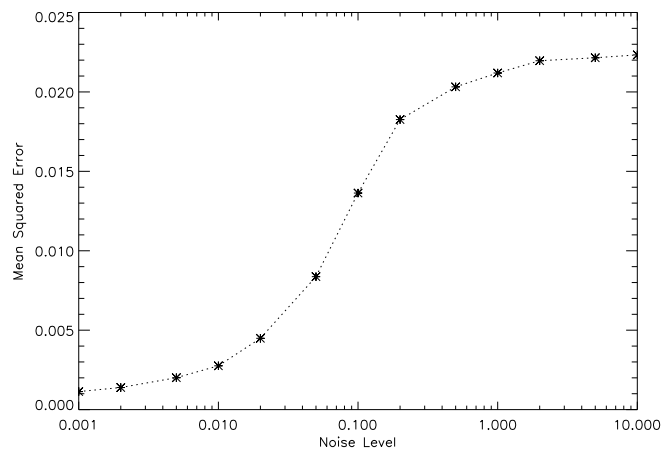### 4.1.2 Typical curve of a reconstruction

Figure 3: A typical curve of the reconstruction error versus the noise level. This curve results from the average of 100 noise occurrences on object 1, on a simulated interferometer with 15 telescopes.

Figure 3 shows a typical curve of a reconstruction dominated by the noise, which means the noise is the only cause of difficulty in this reconstruction. Thanks to the sampling and the high amount of noise occurrences per noise level, about 100, the curve is very smooth.

Three main parts can be distinguished. In the first part of the curve, for high SNR to medium SNR, the error is rather constant and low : this indicates the convergence to an image very similar to the object, thus a successful reconstruction. In the second part of the curve, for medium to low SNR, the error is raising with the SNR : BSMEM has difficulties distinguishing the object from the noise, however some real structures inherent to the object can still be found. In these cases a stronger prior helps enhancing the details. Finally,

in the third part of the curve, at low to very low SNR, the error remains high and constant. The noise level prevents the algorithm to recover the object, and BSMEM is unable to depart meaningfully from the prior.

4.1.3   Reconstructed images : noise parameters

Reconstructed images obtained by simulations on all targets and all array configurations are presented on figures 4 to 27.

At high and medium SNR on both noise parameters, MEM is always able to retrieve at least the main features of all targets. Of course the better the *uv* coverage is, the better the reconstruction gets (see next section 4.1.4), but both noises do also play major role.

Note that at 0.0001 noise on phases MEMSYS behaviour is bugged, with worse reconstructions than for 0.002. The origin of the problem is due to the way MEMSYS treats the phase errors (using inverse quantities) and is currently under investigations. Nearly noiseless reconstructions with BSMEM should be avoided for now. With this exception, reconstructions behaves as expected : noisier data sets produce poorer reconstructed images, and more compact objects (3, 5, and 6) are more difficult.

As a rule, and a good example is provided on figure 24 at 0.002 noise on phases, when the noise on visibility amplitudes increases at fixed noise on phases, MEM is initially able to reconstruct the image with slightly less fine details. Then visible noise appears on the reconstructed image, and finally a brutal rupture point arises, at which point the reconstruction of the target is not really possible anymore, and convergence is achieved on an image similar to the prior (Gaussian shape).

On the other hand, when the noise on visibility phases increases at fixed noise on amplitudes, the image is progressively affected by a more diffuse noise, but this does not prevent the target from being partially reconstructed. A simple explanation is that the phases are often seen are the quantities which allow the localisation of the flux (given by the amplitude) in the reconstruction. Noisier phases just lead MEM into putting flux in the wrong places, while noisier amplitudes prevent MEM from even retrieving the global shape of the target. An interesting illustration of this principle is on figure 23, at 0.02 amplitude noise. While the noise on phases remains low, both stars still appear separated, and as soon as the phases get noisier, their respective disks blend. Still on the same figure, at 0.2 amplitude noise, the reconstructed image is mostly derived from the prior. With low SNR on phases the reconstruction is approximatively a disk, while with high SNR on phases the principal axis of the target is still correctly retrieved.

4.1.4   Reconstructed images : array configurations

At reasonable SNR, the 15 telescope *uv* coverage gives nearly perfect images, and point source targets are particularly well rendered (figure 7). In comparison, on other configurations a certain amount of ghosting appears around the stars, slowly raising as the *uv* coverage gets worse. The stars themselves are not point-like anymore, though both components can perfectly be distinguished and are of the correct flux ratio. This situation remains unchanged on the resolved binary. Note that high SNR phases are more important than high SNR visibility amplitudes in order to distinguish the weakest star (figure 8).

The reconstruction of low level intensities is much harder with poorer *uv* coverage, as underlined by object 4 reconstructions (figures 16 to 19). When BSMEM successfully manages to reconstruct the target, from 5-7 of 7 stars are clearly visible with 15 telescopes, 4-7 with 8 telescopes, 3-7 with the 6 telescope one, and 3 to 4 for the 4 telescope one. As for this object star fluxes follow a progression of 50%, 20%, 10%, 5%, 2%, 1%, this roughly translates into doubled reconstruction sensitivity when going from the 4 telescope array to the 6, 8 and finally to the 15 one. It can be noted that phase noise alone can compromise the performance of an array, rendering it as sensitive as an array of lesser *uv* coverage. At the same level of noise on visibility amplitudes, a 4 telescope array with high SNR closure phases can perform better than a 8 telescope one with low SNR. This is a strong advocacy for decent SNR on closure phases.

Even if model-independent imaging seems difficult with the 4 telescope array, it should be noted that it generally succeeds in retrieving the main brightest features of all other targets. Object 3 is where this main feature – the central background disk – is the faintest compared to its other components and where the major improvement is brought by going from 4 to 6 telescopes. The 4 telescopes array can clearly reconstruct the

bright spots, but not the disk itself (figure 12) even at high SNR, while the 6 telescopes array (figure 13) can at medium SNR. Note that this is not due to *uv* coverage alone, but also to the additional bispectrum points for this configuration (see next sections). The 8 and 15 configurations further improves the results, reconstructing the object with the right shape even with low SNR phases.

Finally the point-symmetric object 5 and nearly point-symmetric object 6 underline an interesting behaviour of BSMEM. These are difficult objects, in particular because phases do not bring much useful information (see the bispectrum/powerspectrum tests in section 4.2). At low to medium SNR BSMEM cannot reconstruct these targets even with the 15 telescopes *uv* coverage. Object 5 is composed of two symmetric systems of binaries : one task of the reconstruction is to separate these two systems with the correct sizes. At high SNR all configurations are able to do so. On the contrary, at lower SNR the greater arrays have difficulties to converge to a satisfying solution, as if they could not depart from the prior. Quite unexpectedly, the 4 telescope array still allow a correct estimation of the size of each system (visibility amplitude noise of 0.05, on figures 20, 21, 22 and 23). The other reconstruction task is to retrieve the binaries inside each system. Reconstructions with 4 telescopes never accomplish this. The other configurations are equally good at high SNR, but the 8 telescope one is the best performer overall : it can depart from the prior at medium SNR while the 15 telescope one cannot and the 6 telescope one strongly suffers from noise.

The same situation arises with reconstructions from object 6 : at medium SNR (visibility amplitude noise of 0.02) they seem slightly better with 4 telescopes on figure 24 than, by example, with 15 on figure 27. A probable explanation is that BSMEM has more difficulties departing from the prior when using huge noisy data sets than when using smaller ones (or better ones). In this case the choice of a less neutral prior would be highly advised to remedy this convergence issue.

4.1.5   Error and standard deviation of reconstruction

Figures 28 and 29 show the average error of reconstruction versus both noise parameters for all array configurations and all targets. In addition, the standard deviation, which measures the repeatability of the reconstruction at the same noise levels and thus is related to the confidence the user can have in it, is presented on figures 30 and 31.

As acquiring each error point is very time consuming, all simulations were realized with 20 noise occurrences, which is a lower amount than on figure 3 but sufficient for our purpose. The sampling was also reduced so that errors were only computed at noise levels 0.0001, 0.002, 0.02, 0.05, 0.1 and 0.2.

On figure 28 and 30 different levels of phase noise have been assigned different colours while visibility amplitude noise increases along the x axis. The 24 plots inside each figure are mostly similar to each other. Thus on figure 28 the first part of each plot is a performance platter whose height is determined by the phase noise, then all curves join as the visibility noise becomes dominant and reconstruction begins to converge to prior-like solutions. There is a clear degradation of all reconstructions as the visibility noise goes to the highest levels. Standard deviations on figure 30 also back up this observation. There is a defined point at which the standard deviation discrepancy between reconstructions with the same amplitude noise but different phase noises becomes minimal, meaning phase noise is no longer relevant in the success of the reconstruction.

On figure 29 and 31, this time the amplitude noise levels are the one in colour, while phase noise increases along the x axis. Plots on figure 29 present nearly horizontal curves, corresponding to reconstructions in which visibility noise is dominant, so that the amount of phase noise does not change the final result by a significant amount (convergence to prior-like images). Most other curves are U-shaped. At very low phase noise but normal visibility noise the convergence is difficult. The discrepancy between phase and amplitude noise produces thin entropy clouds, which results into convergence problems. As we saw previously on images with a level of 0.0001 phase noise, performance is poor. Then, as phase noise increases to reach typical interferometric levels, we enter the domain of normal reconstructions in which BSMEM gives very satisfying results : the curve slowly reaching an optimum in performance. Finally the phase noise reaches levels at which it begins to degrade the reconstruction (delocalised noise on the image), and the curve raises more abruptly. Overall standard deviation are relatively predictable on figure 31, remaining mostly stable
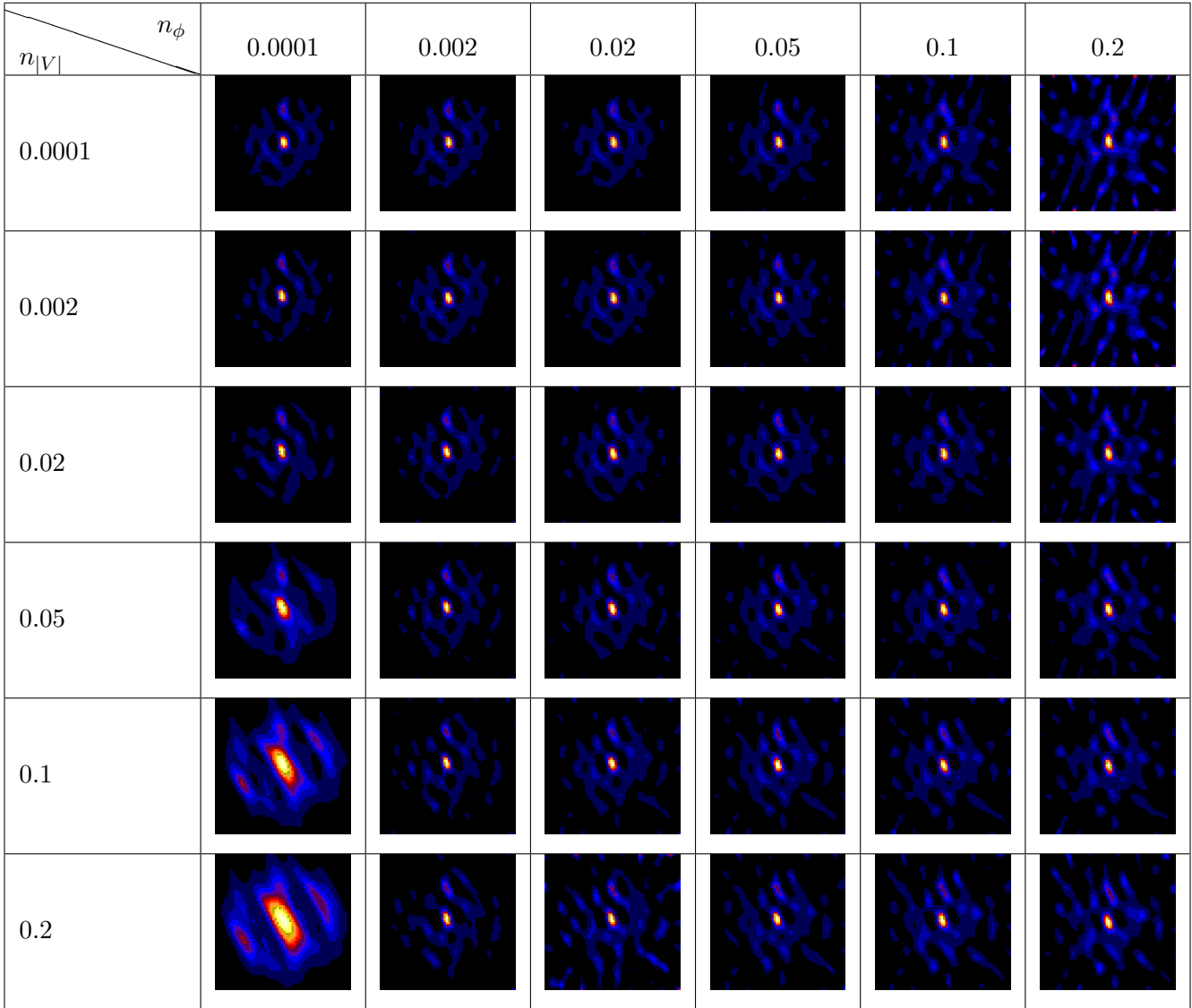
$n_{|V|}$ \ n_ϕ	0.0001	0.002	0.02	0.05	0.1	0.2
0.0001						
0.002						
0.02						
0.05						
0.1						
0.2						

Figure 4: Reconstructed object 1 for several noise parameters, array configuration with 4 telescopes.

or slowly raising with phase noise.

4.1.6 Conclusion on performance with noisy datasets

Although the selected panel of test targets can be considered hard cases, the presented model-independent reconstructions have been successful at noise ranges commonly dealt with in current facilities. Imaging with 4 telescopes is difficult but possible for unresolved or slightly resolved targets. Results show that even with a small number of bispectrum, like in the 4 telescope case, information about the source symmetry is still retrieved. Compared to the ideal situation of 15 telescopes, the 6 and 8 telescope cases lead to noisier reconstructions, but these latter do include all the features of the sources when the SNR stays within the acceptable limits of today's interferometers. The 8 telescope array is particularly impressive, and practically nothing (except a slight noise reduction) is gained from adding other stations.

Unless extreme, noise on visibility phases rarely prevents a successful reconstruction, so that the brightest components of the targets or at least its global shape can still be identified. Noise on visibility amplitudes, though, strongly degrades the performance, up to a point where convergence is hard to achieve and lead to reconstructed images very similar to the prior. Both noise types will hinder the sensitivity of an array, and a noise threshold exists below which an array cannot reach the full potential detained by its uv coverage.
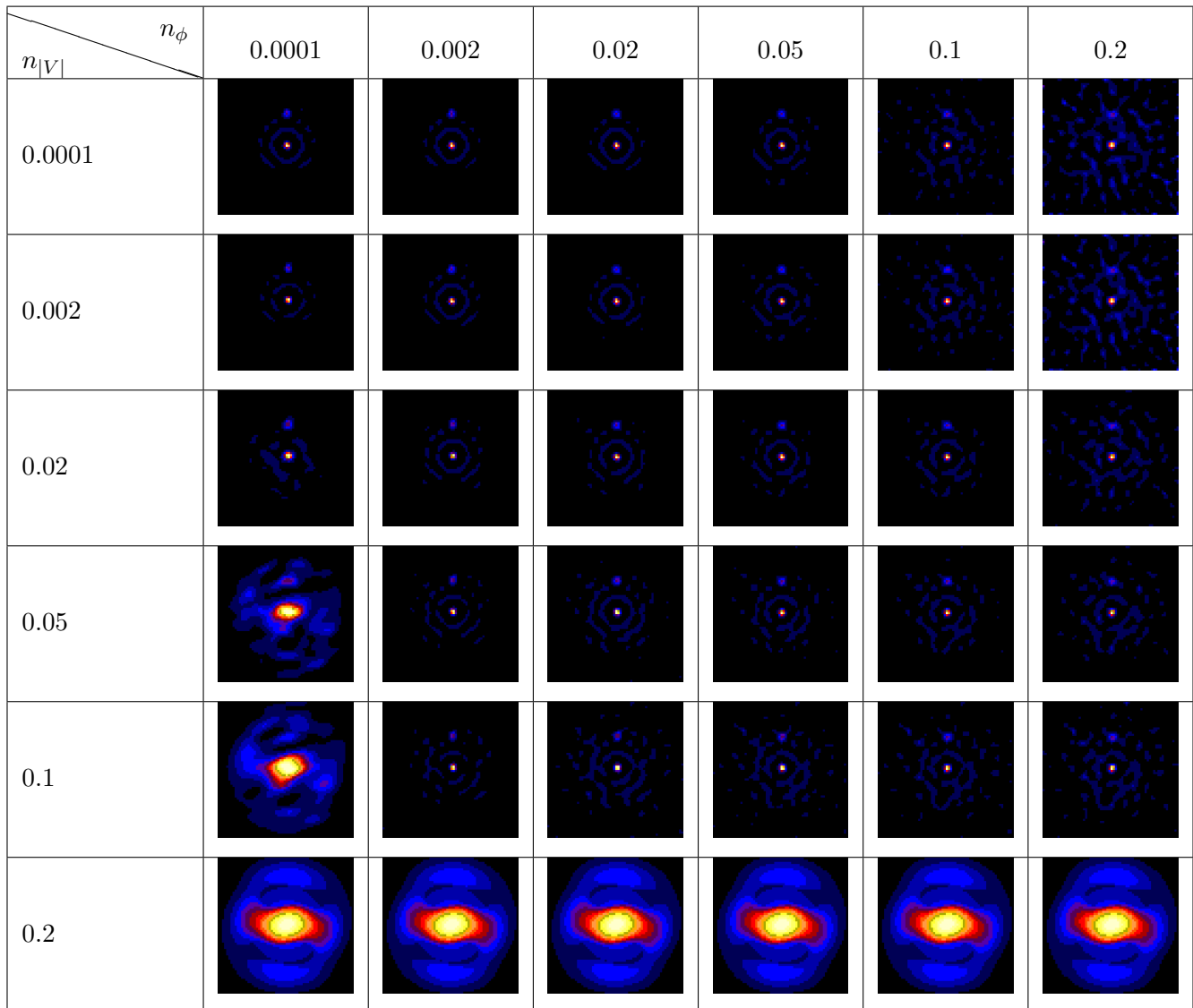
$n_{|V|}$ \ n_ϕ	0.0001	0.002	0.02	0.05	0.1	0.2
0.0001						
0.002						
0.02						
0.05						
0.1						
0.2						

Figure 5: Reconstructed object 1 for several noise parameters, array configuration with 6 telescopes.

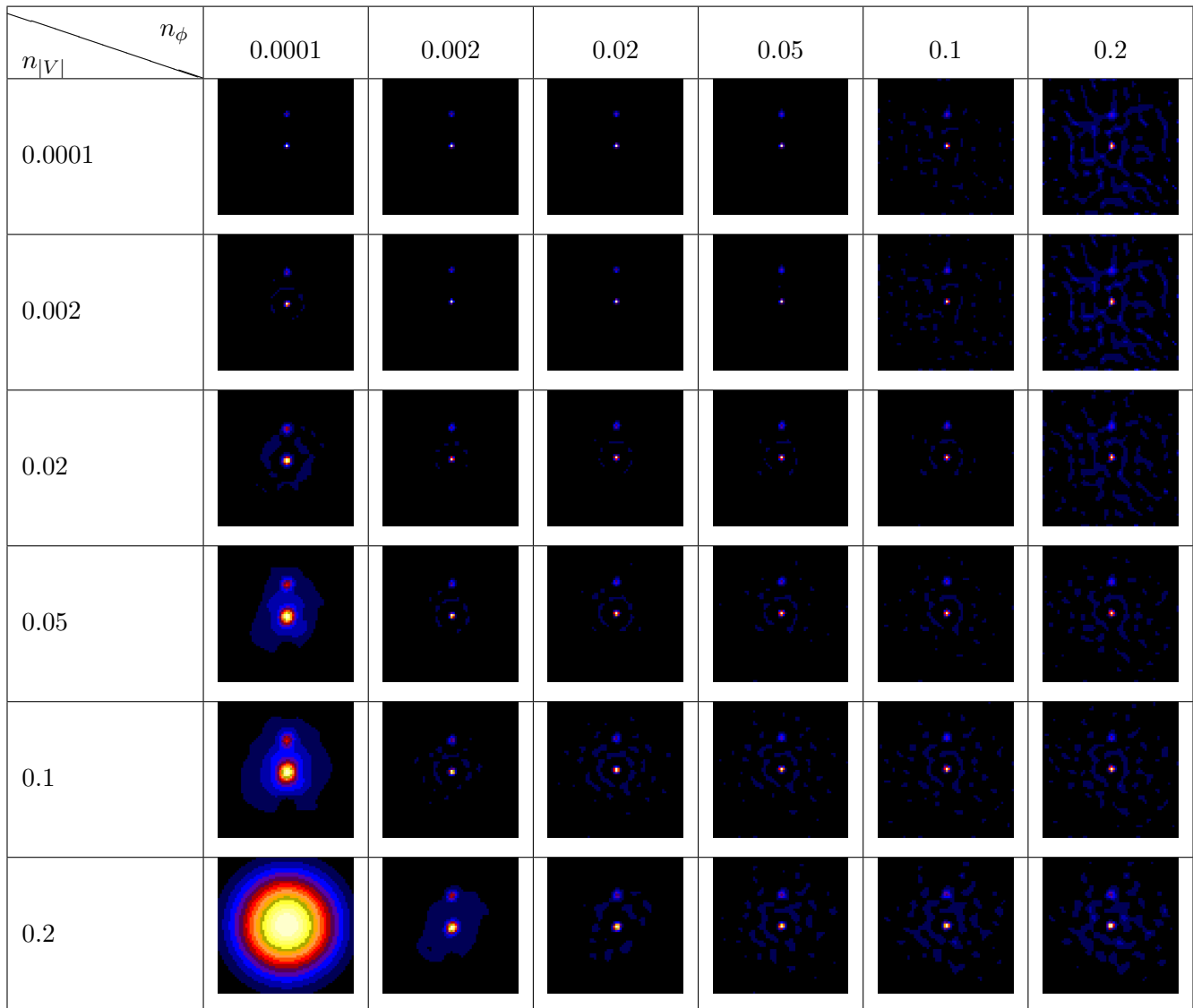| $n_{|V|}$ \ n_ϕ	0.0001	0.002	0.02	0.05	0.1	0.2
0.0001						
0.002						
0.02						
0.05						
0.1						
0.2						

Figure 6: Reconstructed object 1 for several noise parameters, array configuration with 8 telescopes.
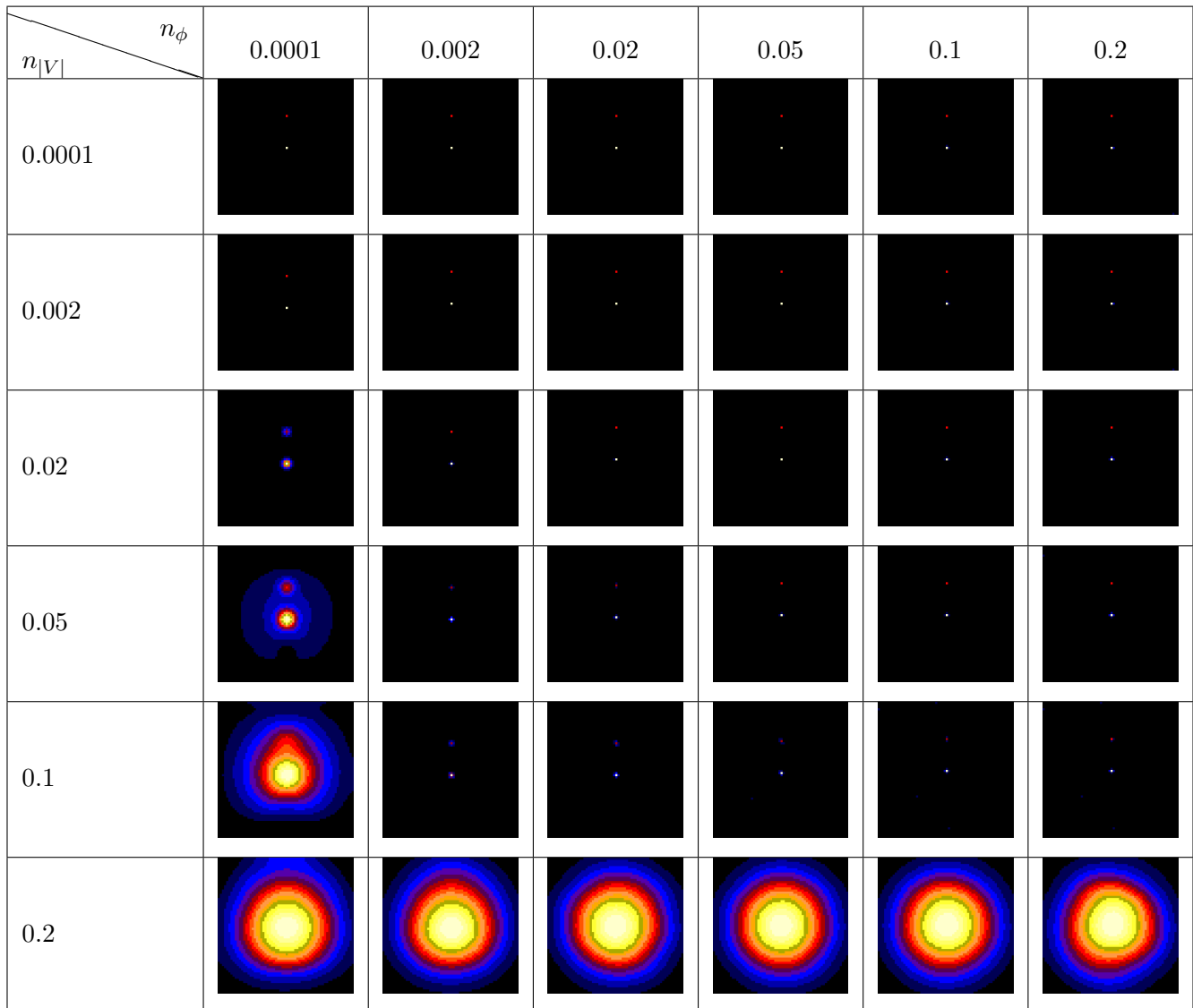
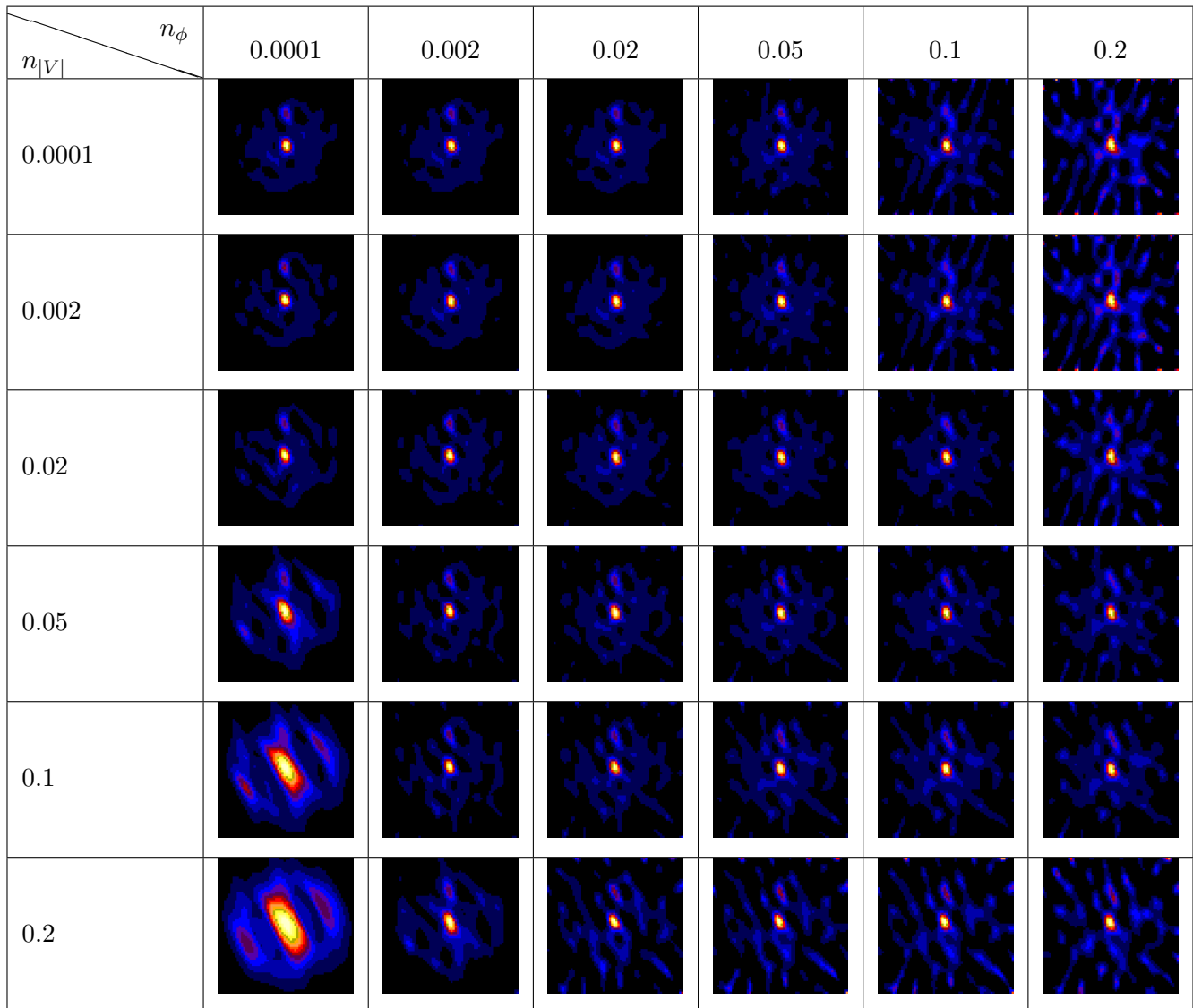Figure 7: Reconstructed object 1 for several noise parameters, array configuration with 15 telescopes.

Figure 8: Reconstructed object 2 for several noise parameters, array configuration with 4 telescopes.
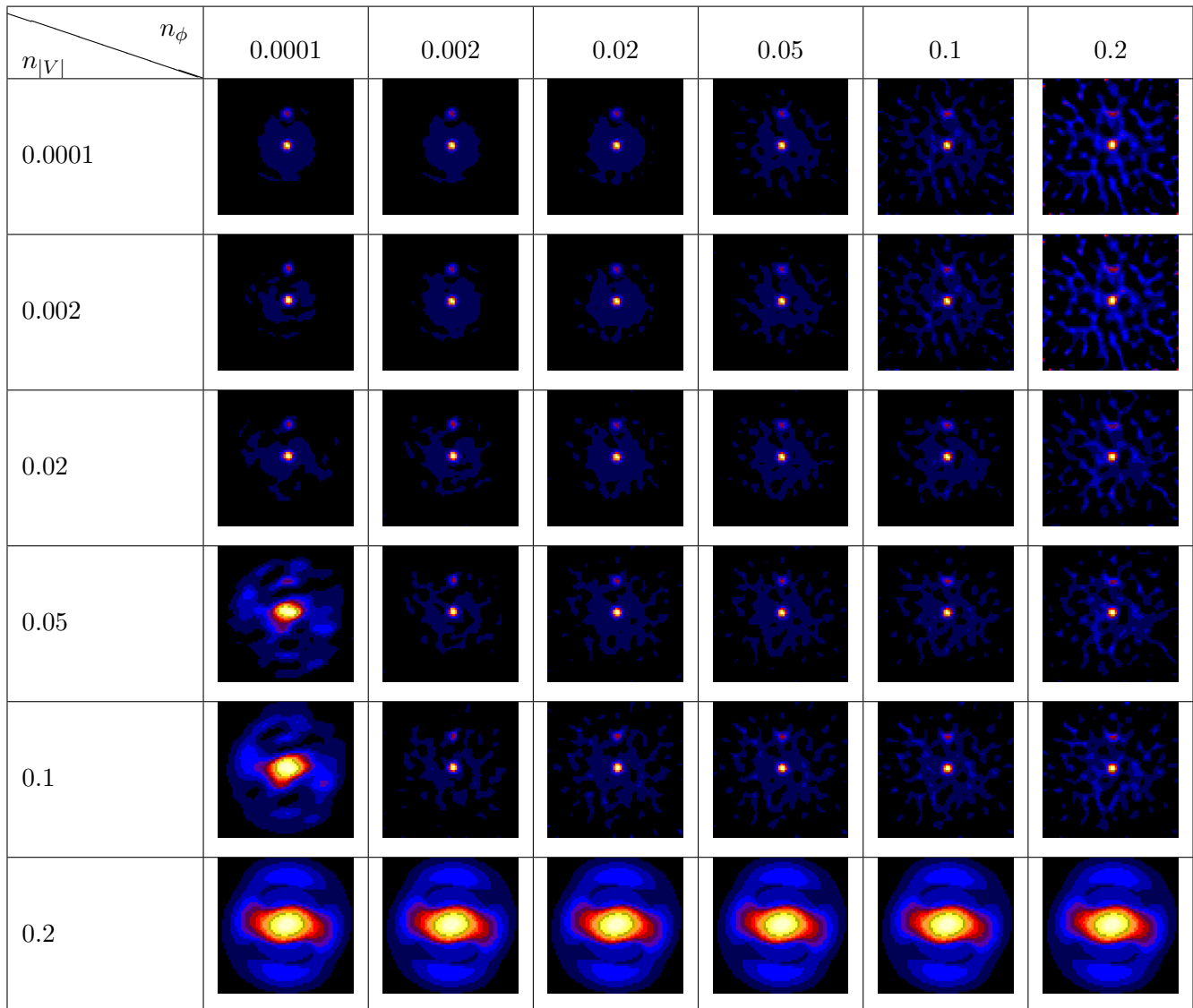
$n_{|V|}$ \ n_ϕ	0.0001	0.002	0.02	0.05	0.1	0.2
0.0001						
0.002						
0.02						
0.05						
0.1						
0.2						

Figure 9: Reconstructed object 2 for several noise parameters, array configuration with 6 telescopes.

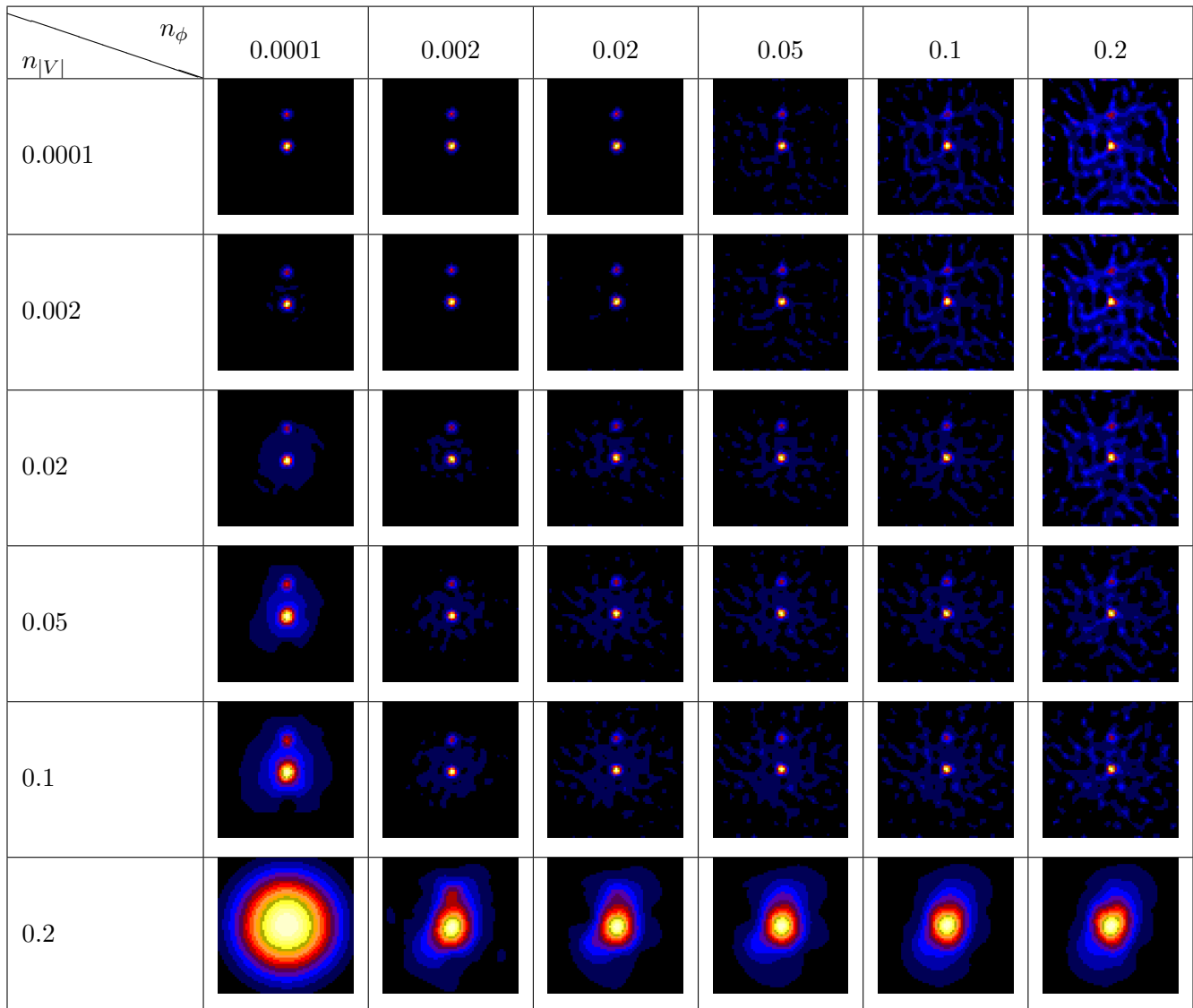| $n_{|V|}$ \ n_ϕ	0.0001	0.002	0.02	0.05	0.1	0.2
0.0001						
0.002						
0.02						
0.05						
0.1						
0.2						

Figure 10: Reconstructed object 2 for several noise parameters, array configuration with 8 telescopes.

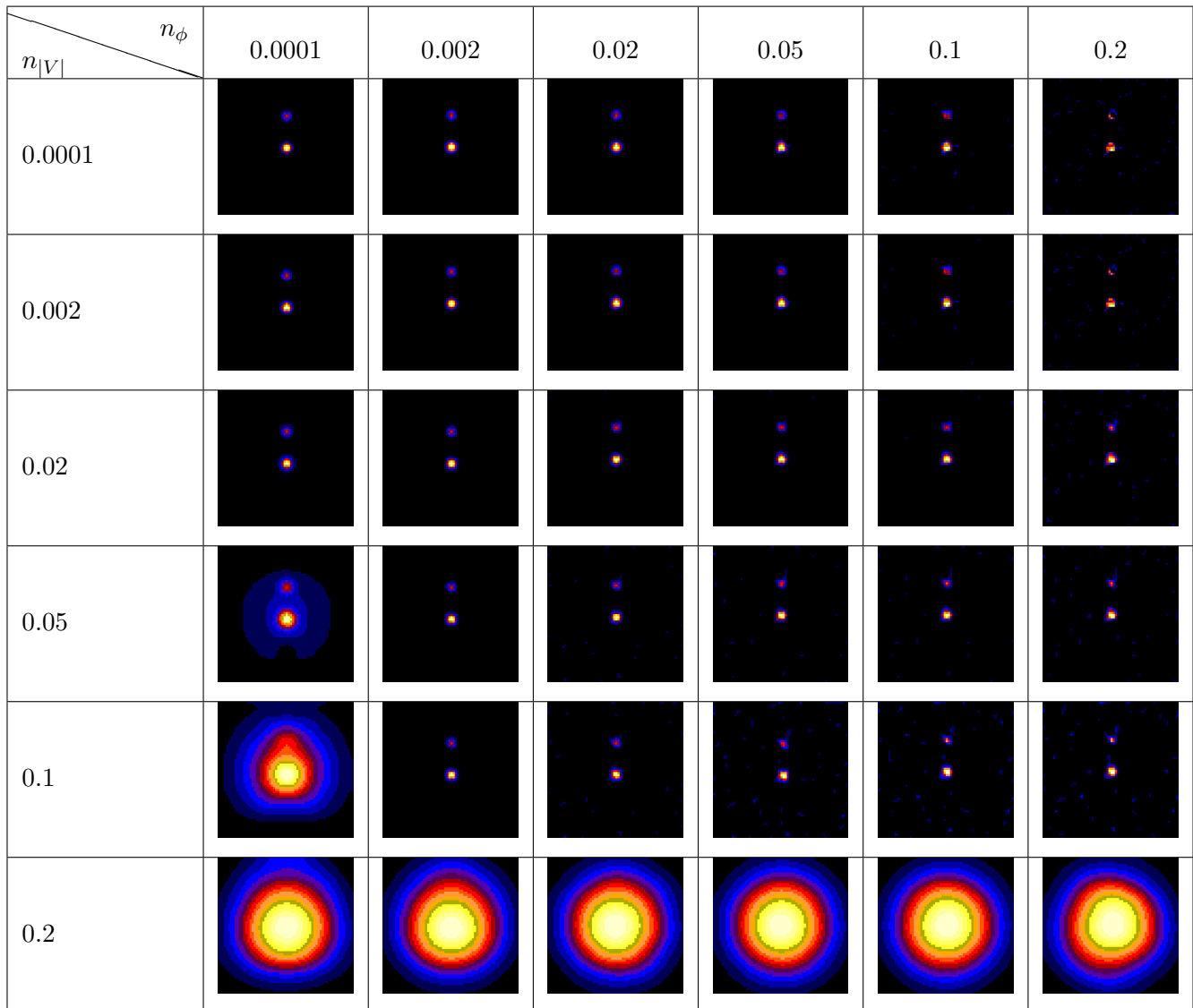Figure 11: Reconstructed object 2 for several noise parameters, array configuration with 15 telescopes.

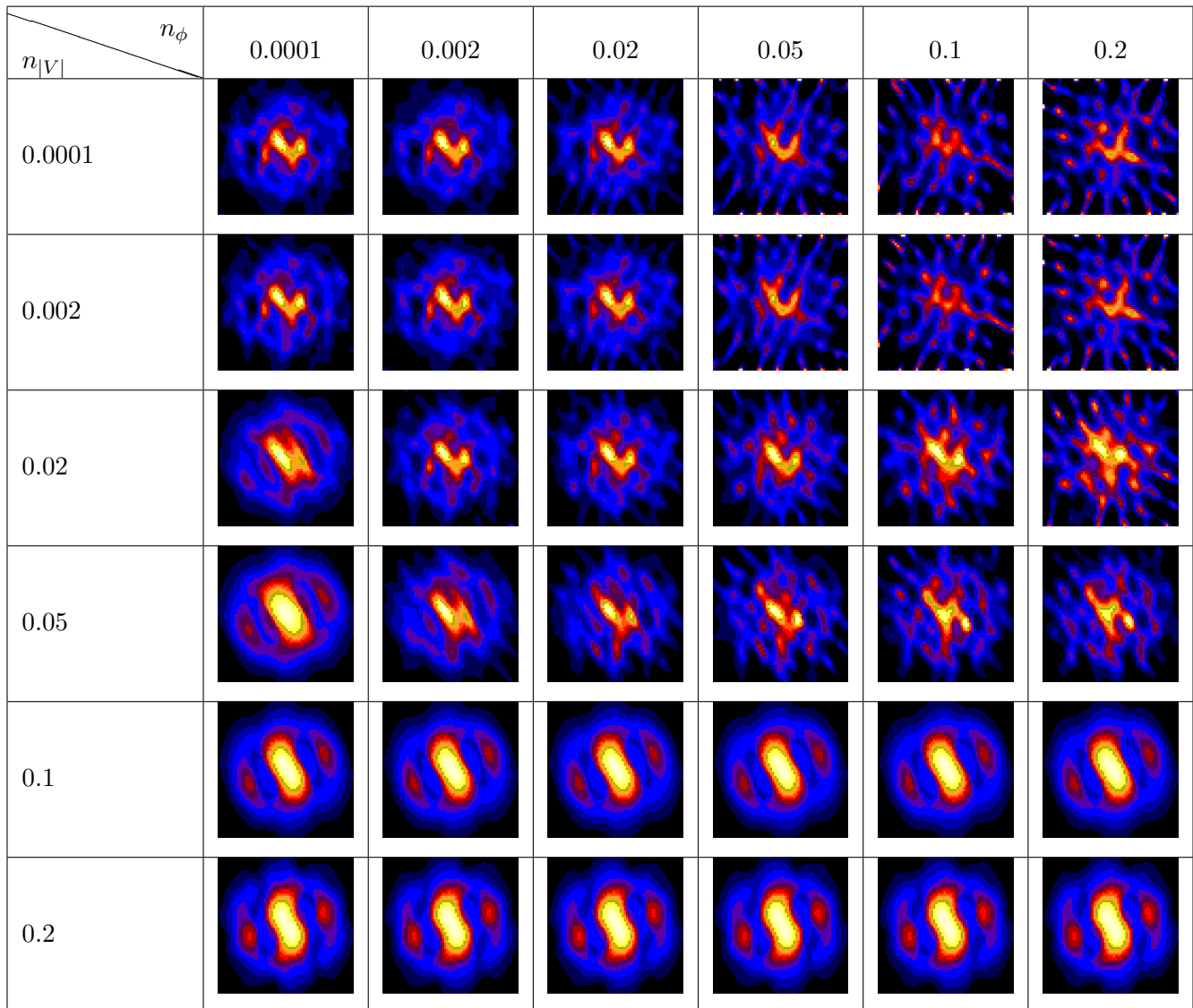| $n_{|V|}$ \\ n_ϕ	0.0001	0.002	0.02	0.05	0.1	0.2
0.0001						
0.002						
0.02						
0.05						
0.1						
0.2						

Figure 12: Reconstructed object 3 for several noise parameters, array configuration with 4 telescopes.
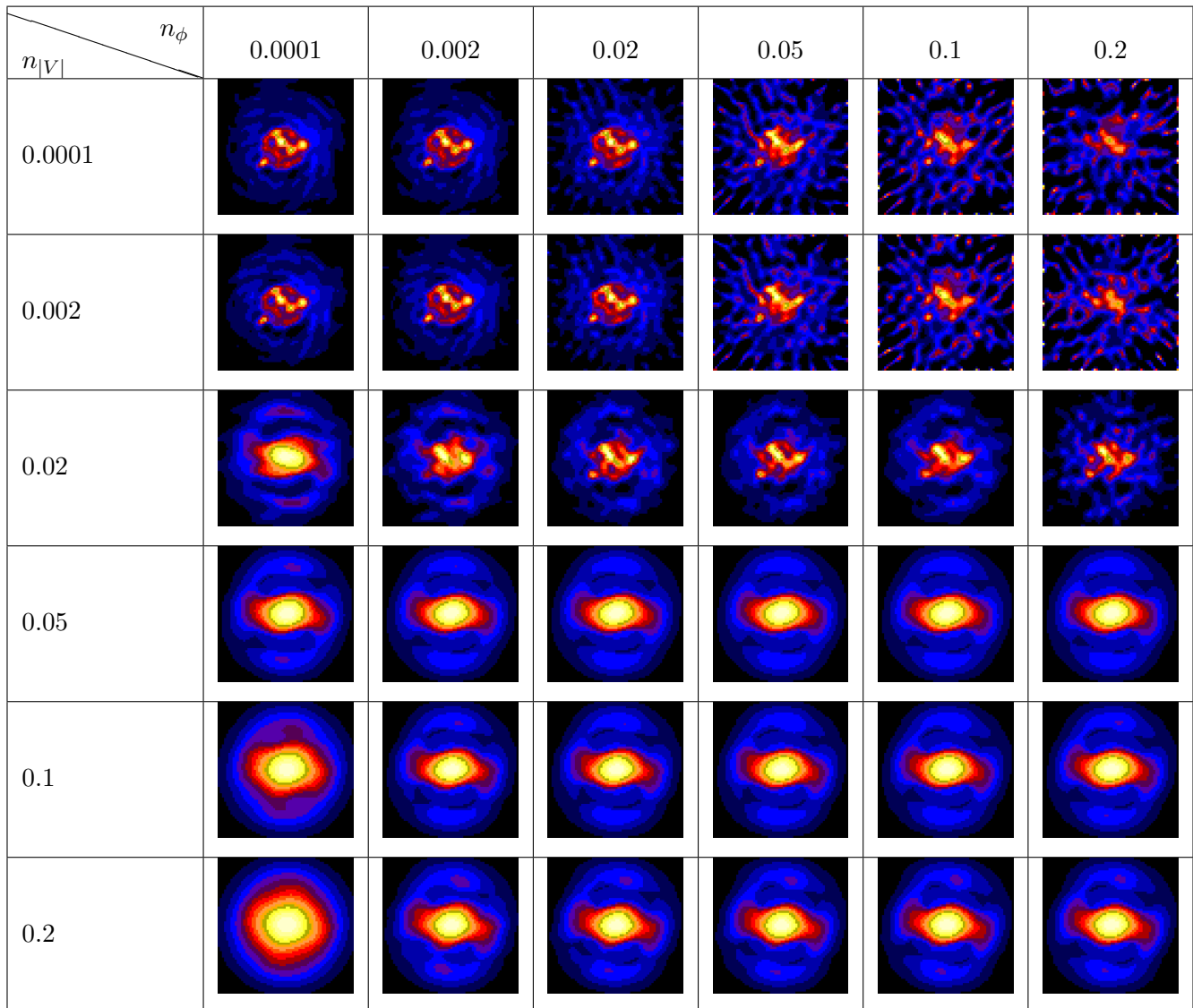
Figure 13: Reconstructed object 3 for several noise parameters, array configuration with 6 telescopes.

Figure 14: Reconstructed object 3 for several noise parameters, array configuration with 8 telescopes.

Figure 15: Reconstructed object 3 for several noise parameters, array configuration with 15 telescopes.

n_ϕ / $n_{|V|}$	0.0001	0.002	0.02	0.05	0.1	0.2
0.0001						
0.002						
0.02						
0.05						
0.1						
0.2						

Figure 16: Reconstructed object 4 for several noise parameters, array configuration with 4 telescopes.

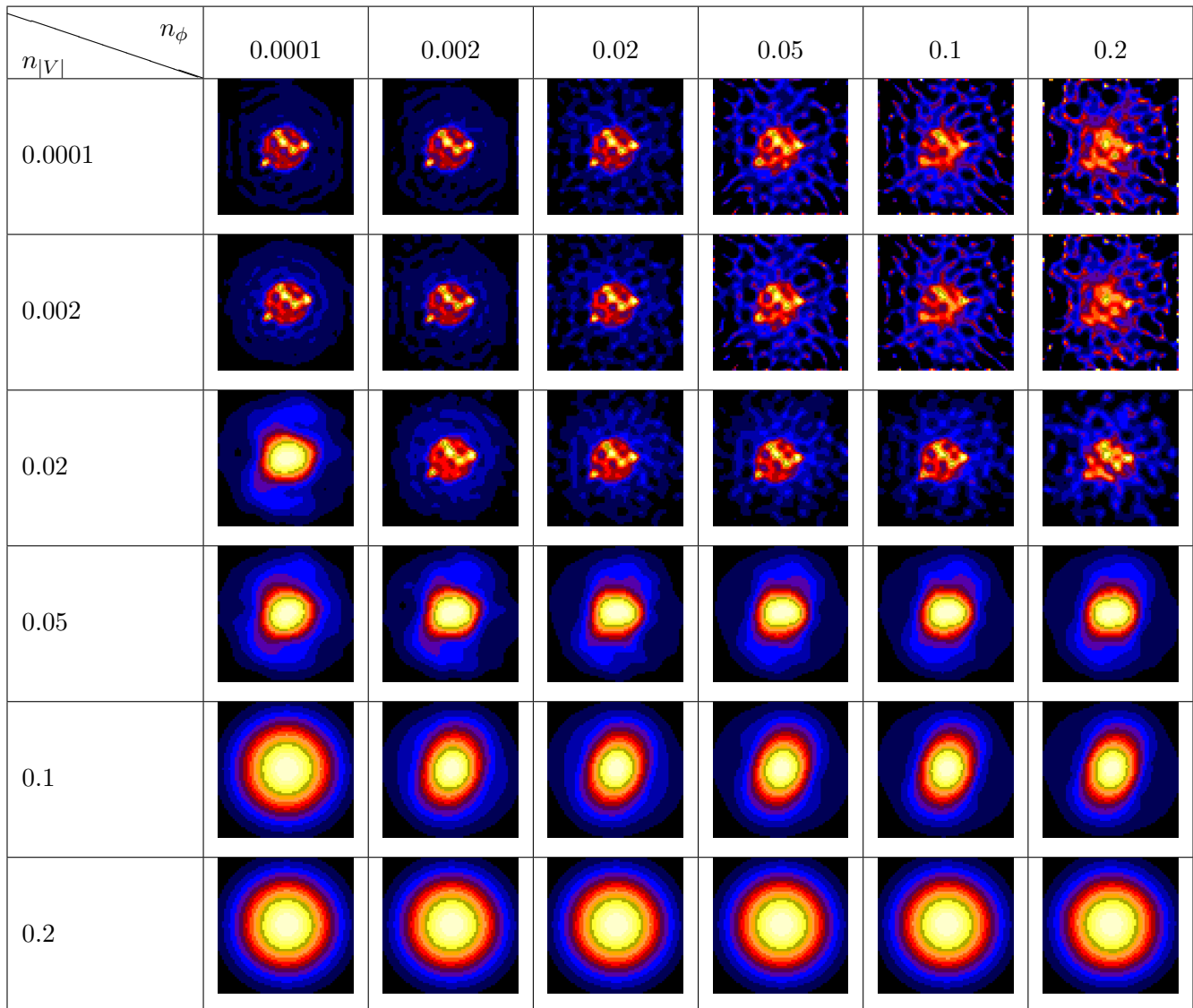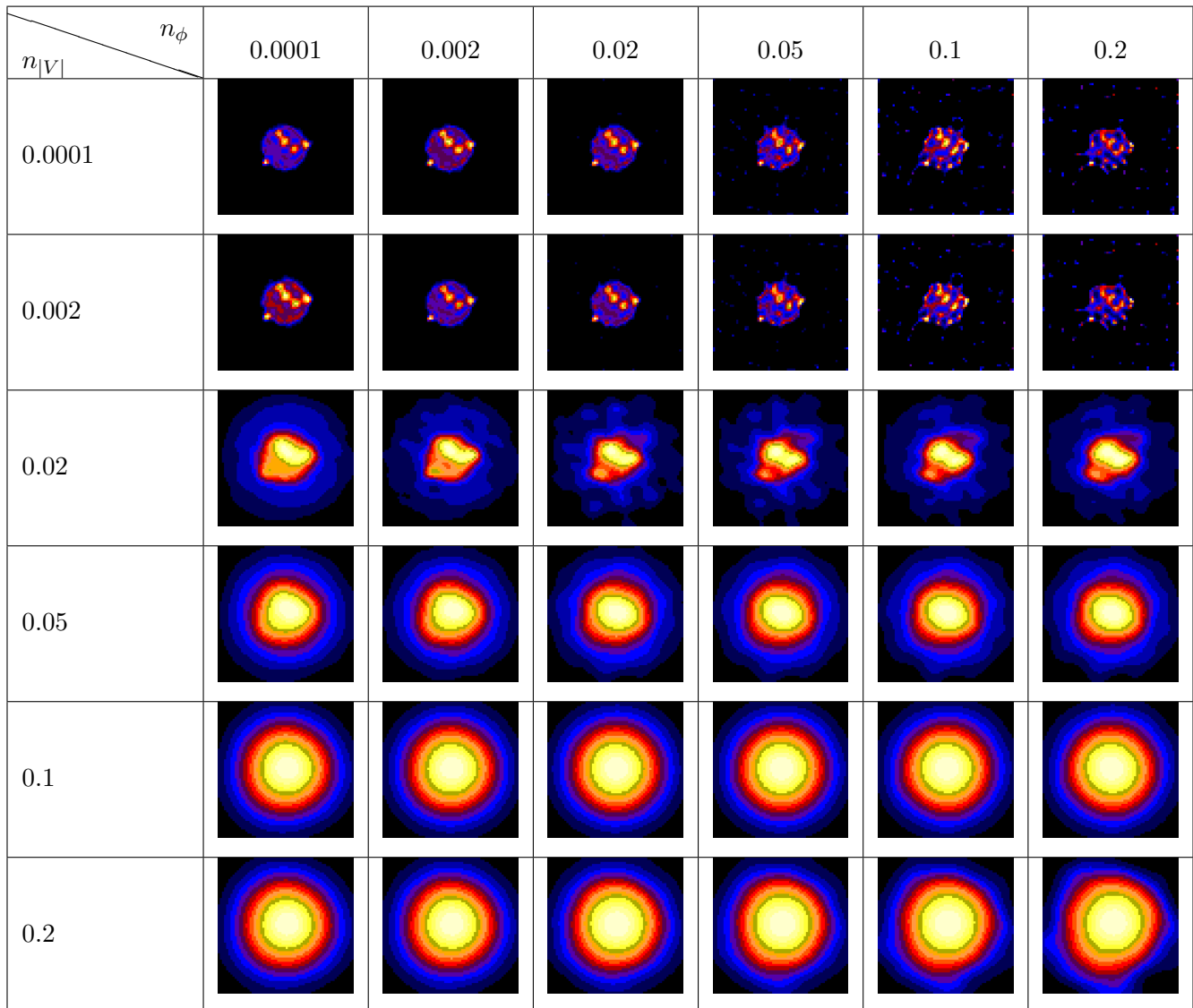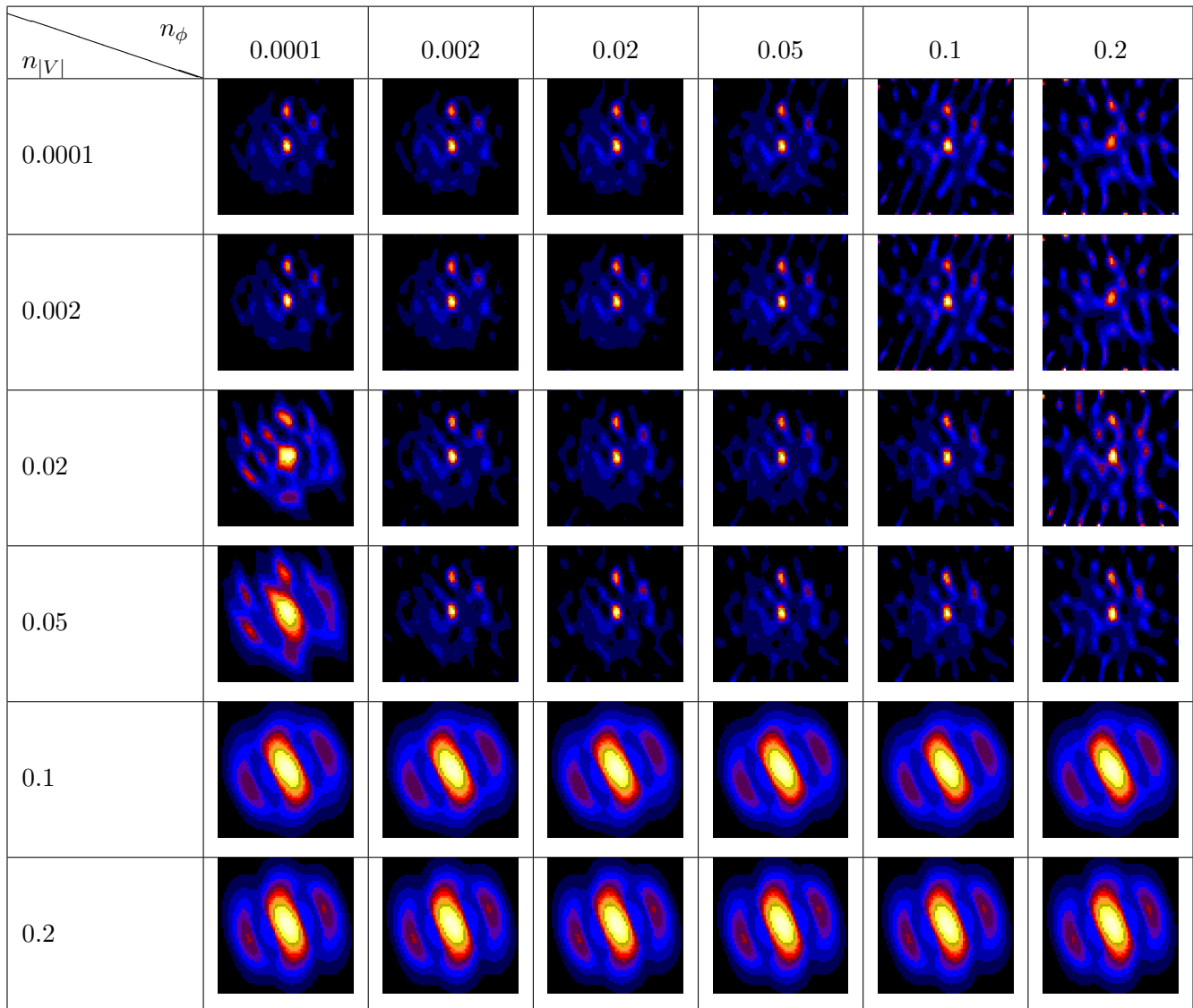Figure 17: Reconstructed object 4 for several noise parameters, array configuration with 6 telescopes.

$n_{|V|}$ \\ n_ϕ	0.0001	0.002	0.02	0.05	0.1	0.2
0.0001						
0.002						
0.02						
0.05						
0.1						
0.2						

Figure 18: Reconstructed object 4 for several noise parameters, array configuration with 8 telescopes.

$n_{|V|}$ \ n_ϕ	0.0001	0.002	0.02	0.05	0.1	0.2
0.0001						
0.002						
0.02						
0.05						
0.1						
0.2						

Figure 19: Reconstructed object 4 for several noise parameters, array configuration with 15 telescopes.

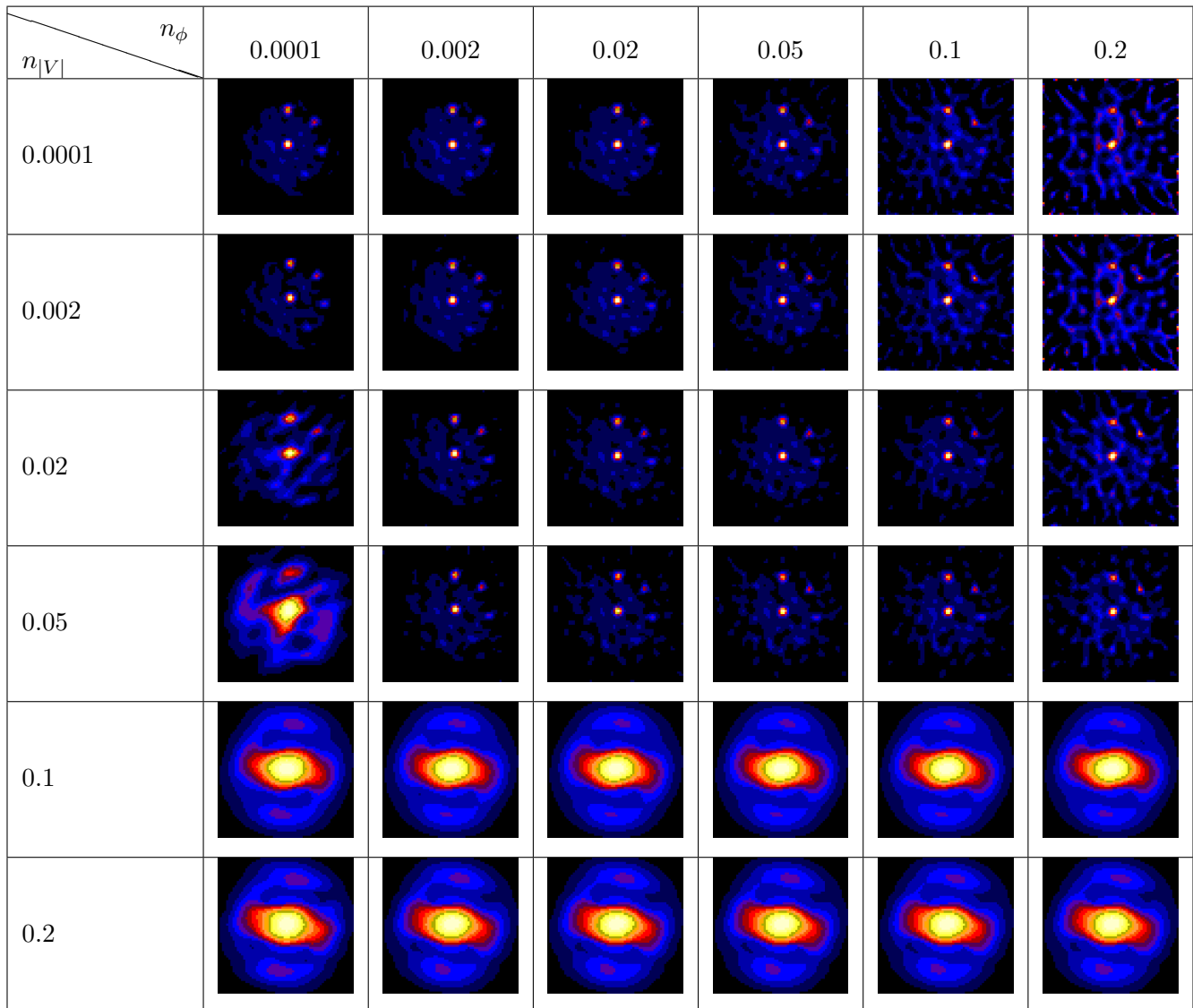Figure 20: Reconstructed object 5 for several noise parameters, array configuration with 4 telescopes.

Figure 21: Reconstructed object 5 for several noise parameters, array configuration with 6 telescopes.
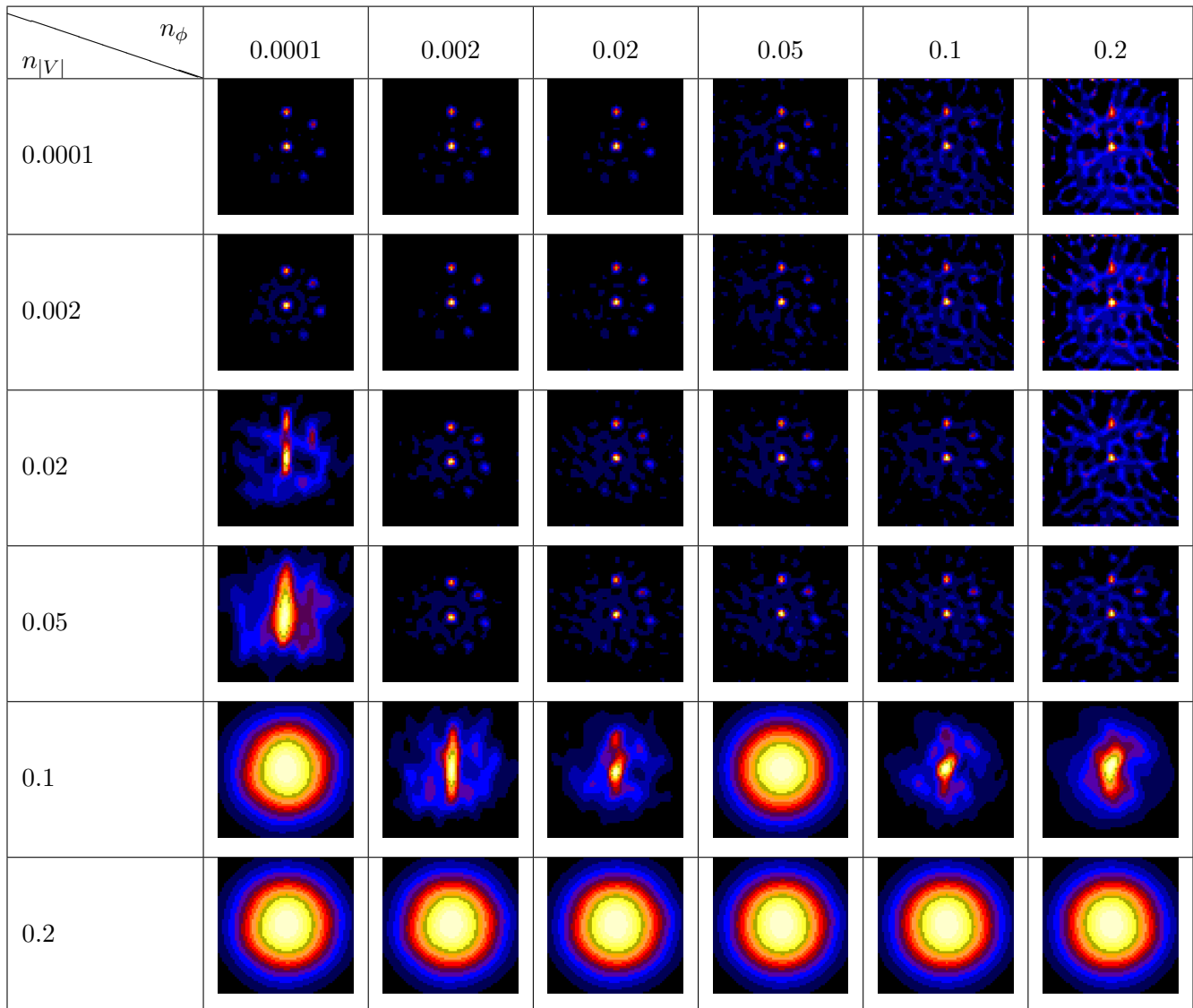
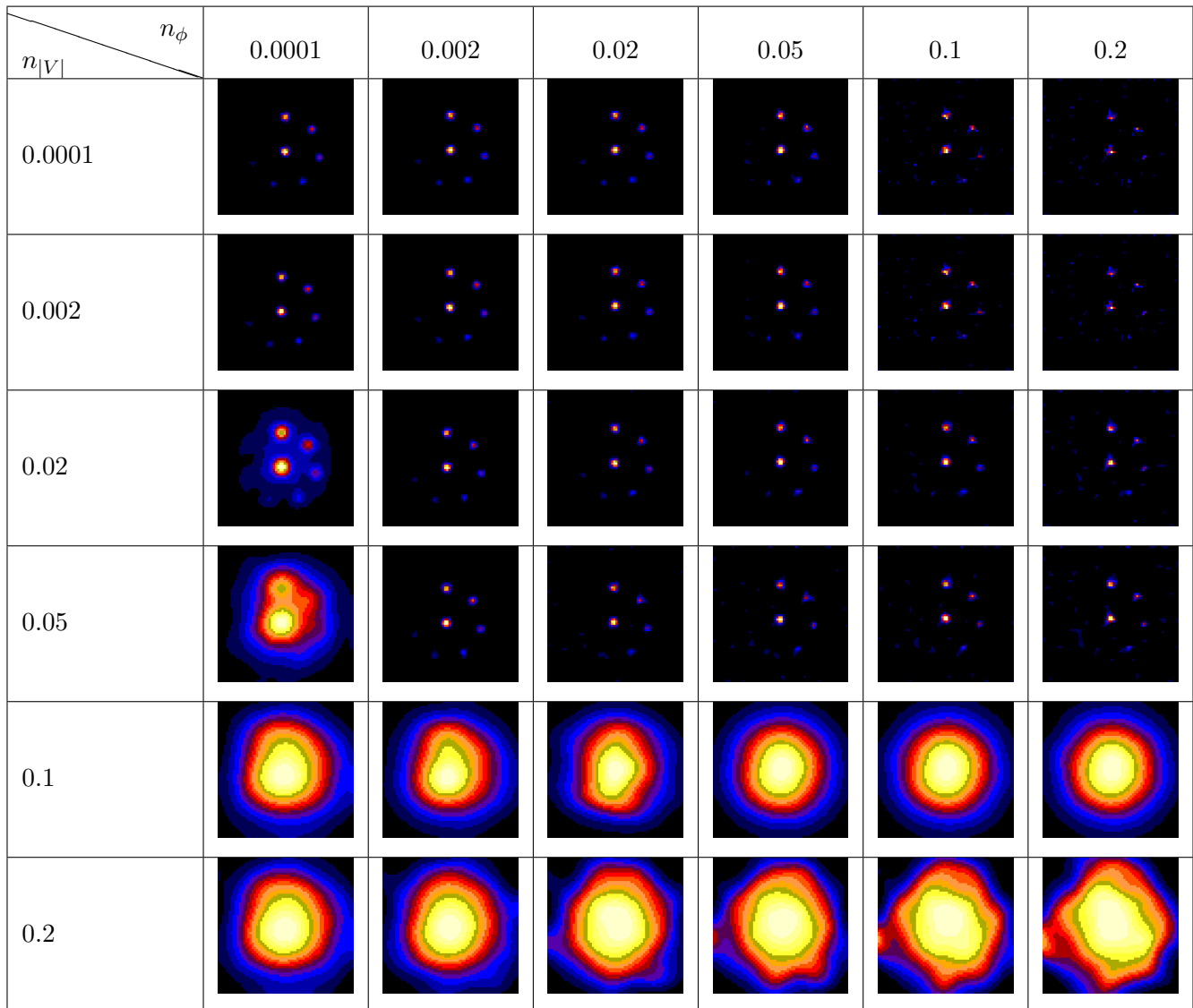Figure 22: Reconstructed object 5 for several noise parameters, array configuration with 8 telescopes.

n_ϕ $n_{|V|}$	0.0001	0.002	0.02	0.05	0.1	0.2
0.0001						
0.002						
0.02						
0.05						
0.1						
0.2						

Figure 23: Reconstructed object 5 for several noise parameters, array configuration with 15 telescopes.
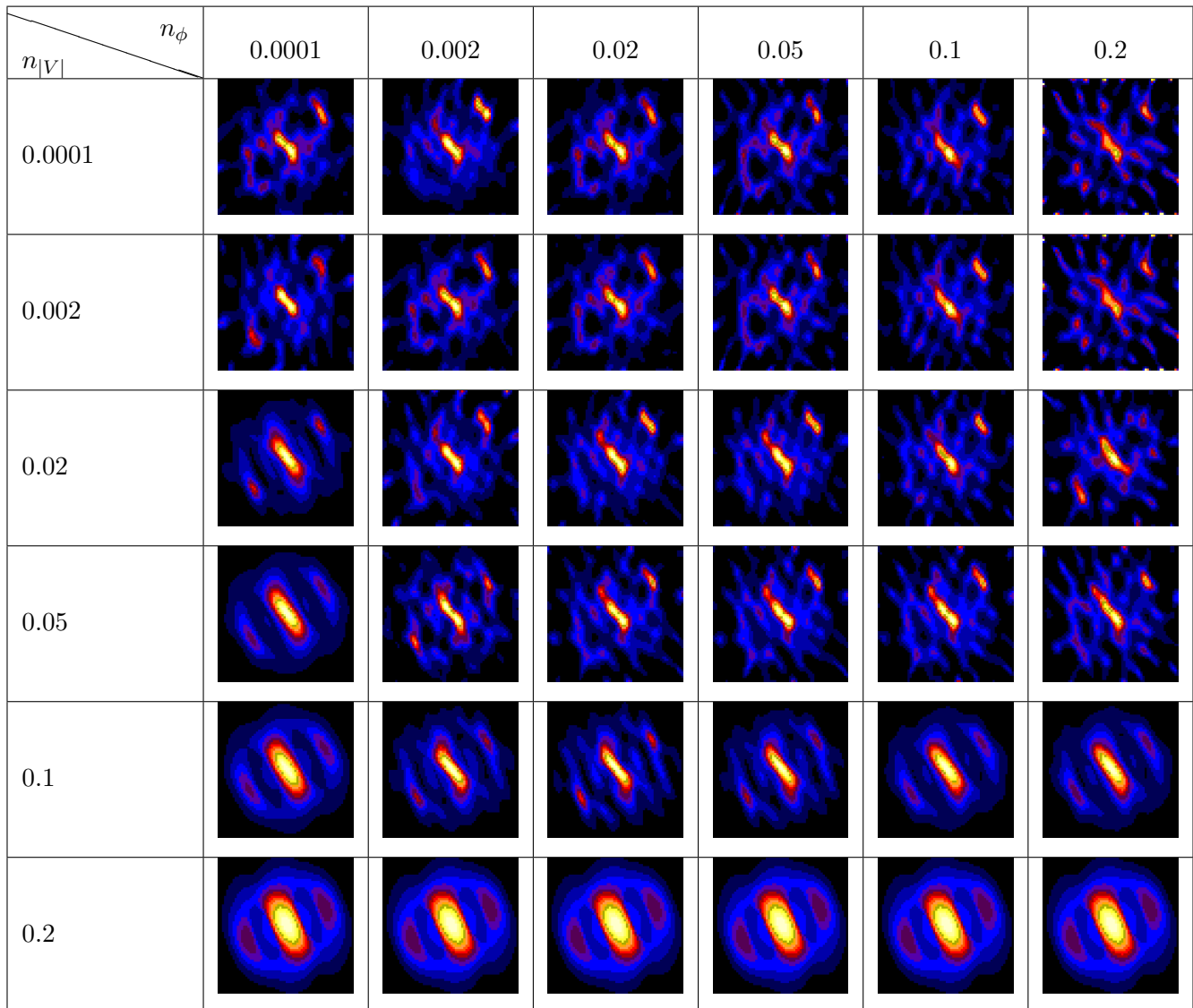
Figure 24: Reconstructed object 6 for several noise parameters, array configuration with 4 telescopes.
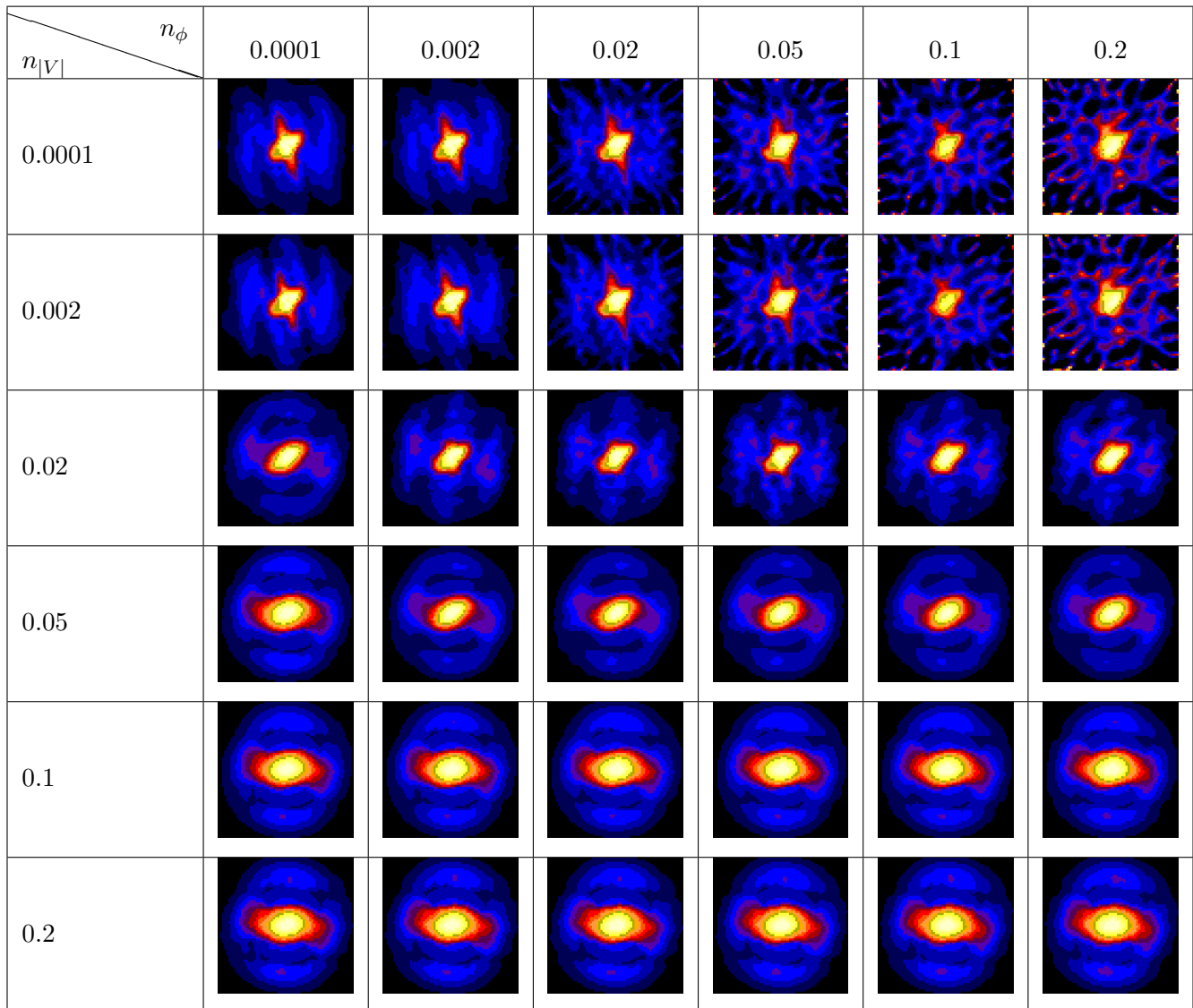
Figure 25: Reconstructed object 6 for several noise parameters, array configuration with 6 telescopes.

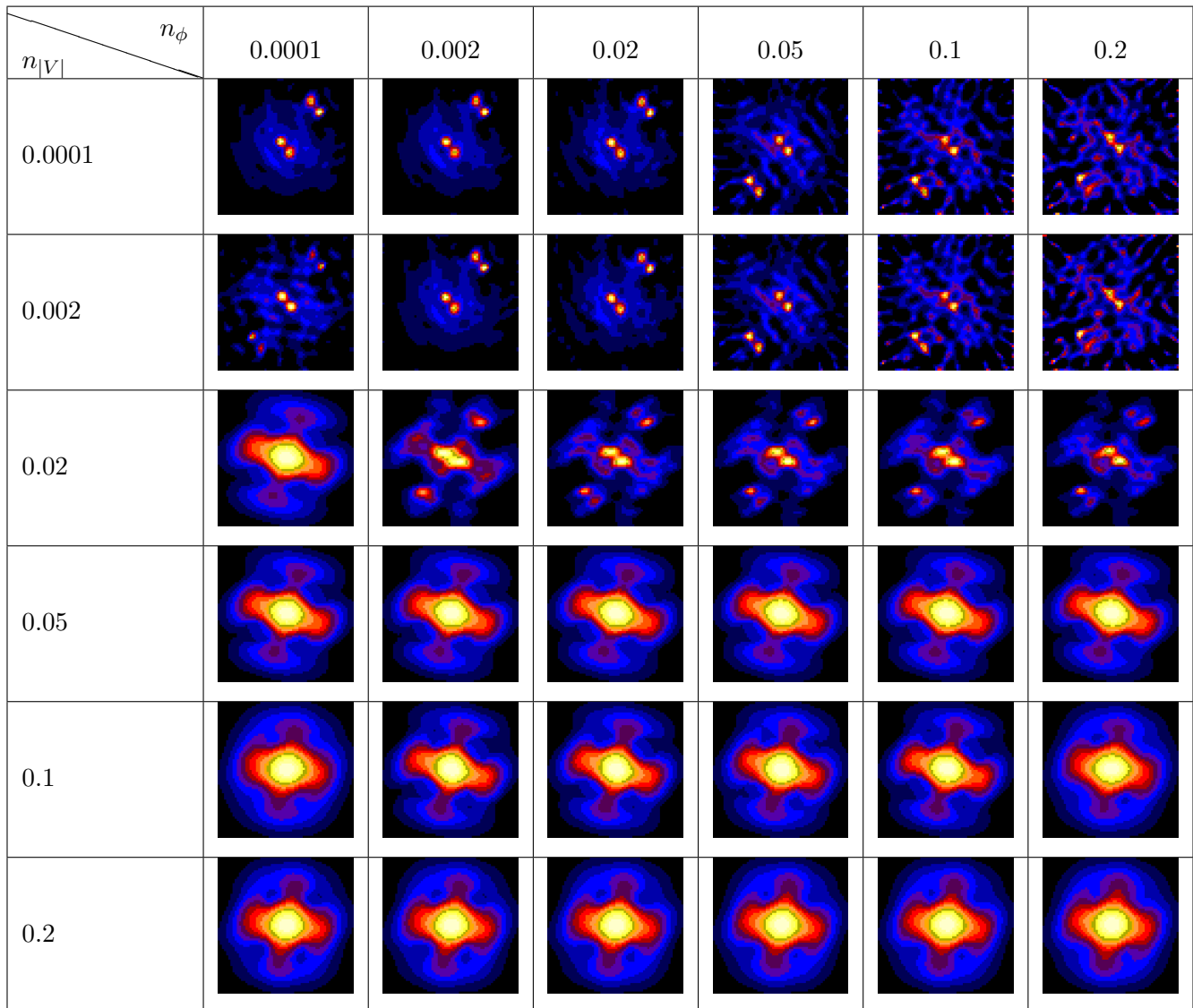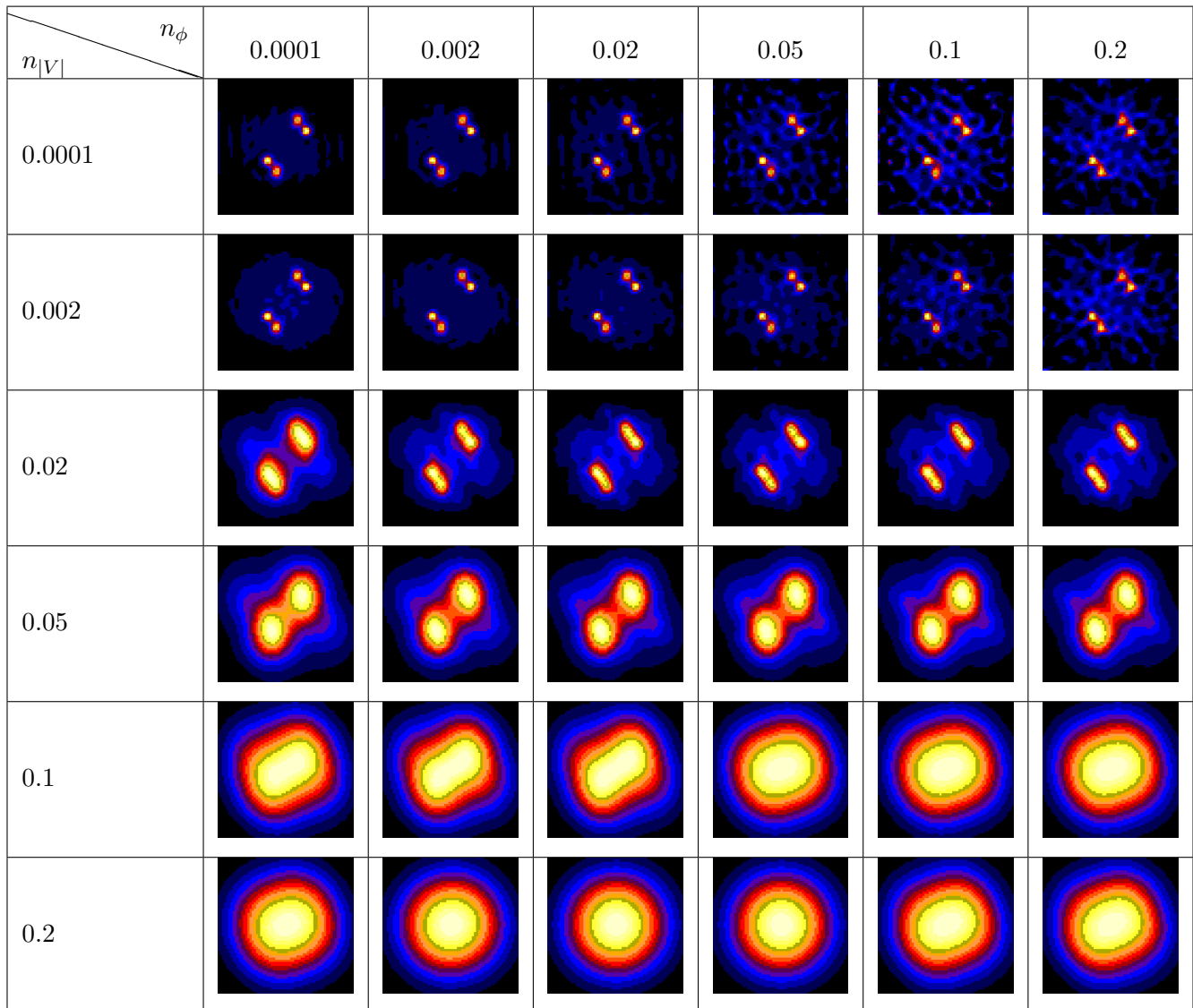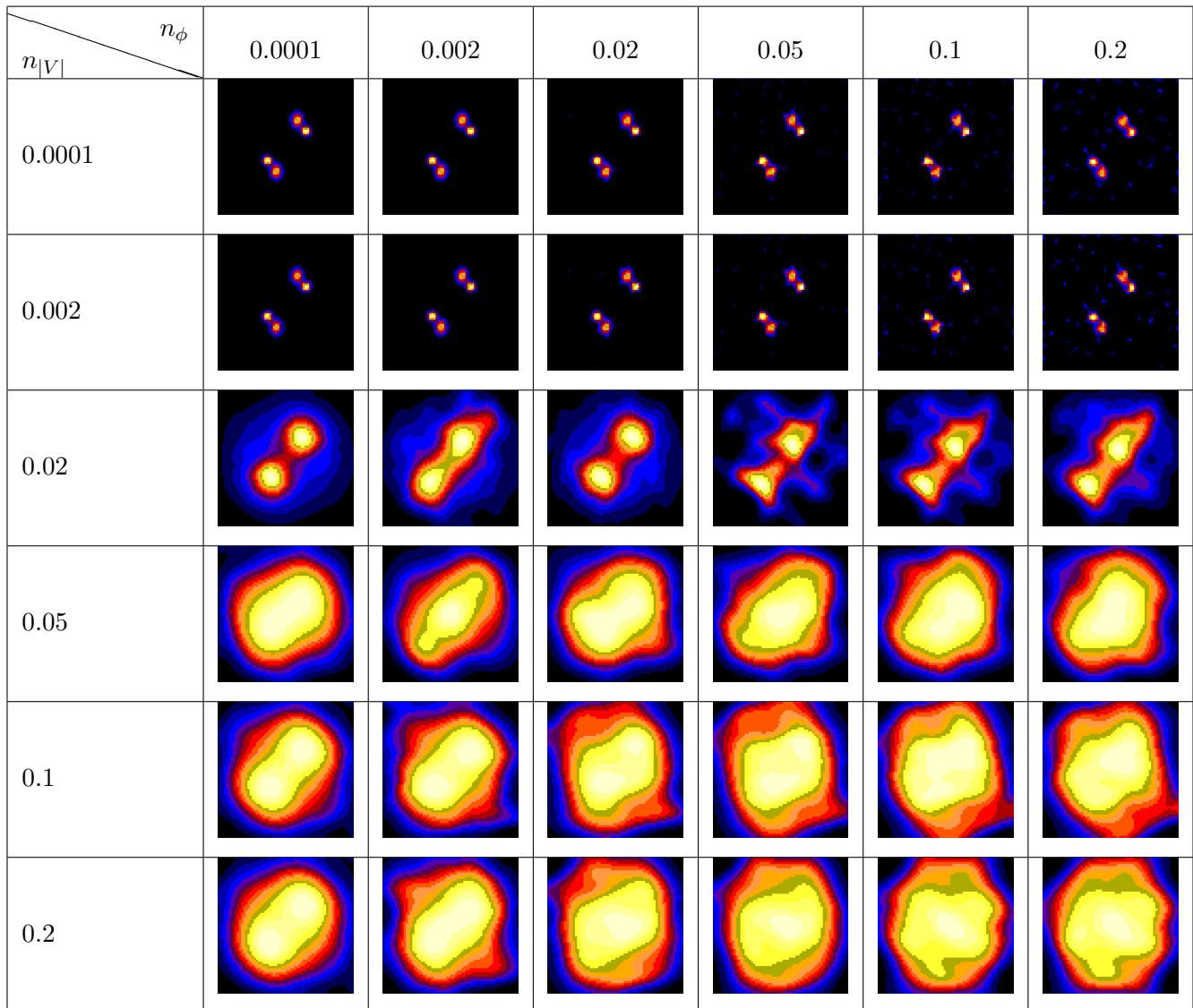| n_ϕ $n_{|V|}$	0.0001	0.002	0.02	0.05	0.1	0.2
0.0001						
0.002						
0.02						
0.05						
0.1						
0.2						
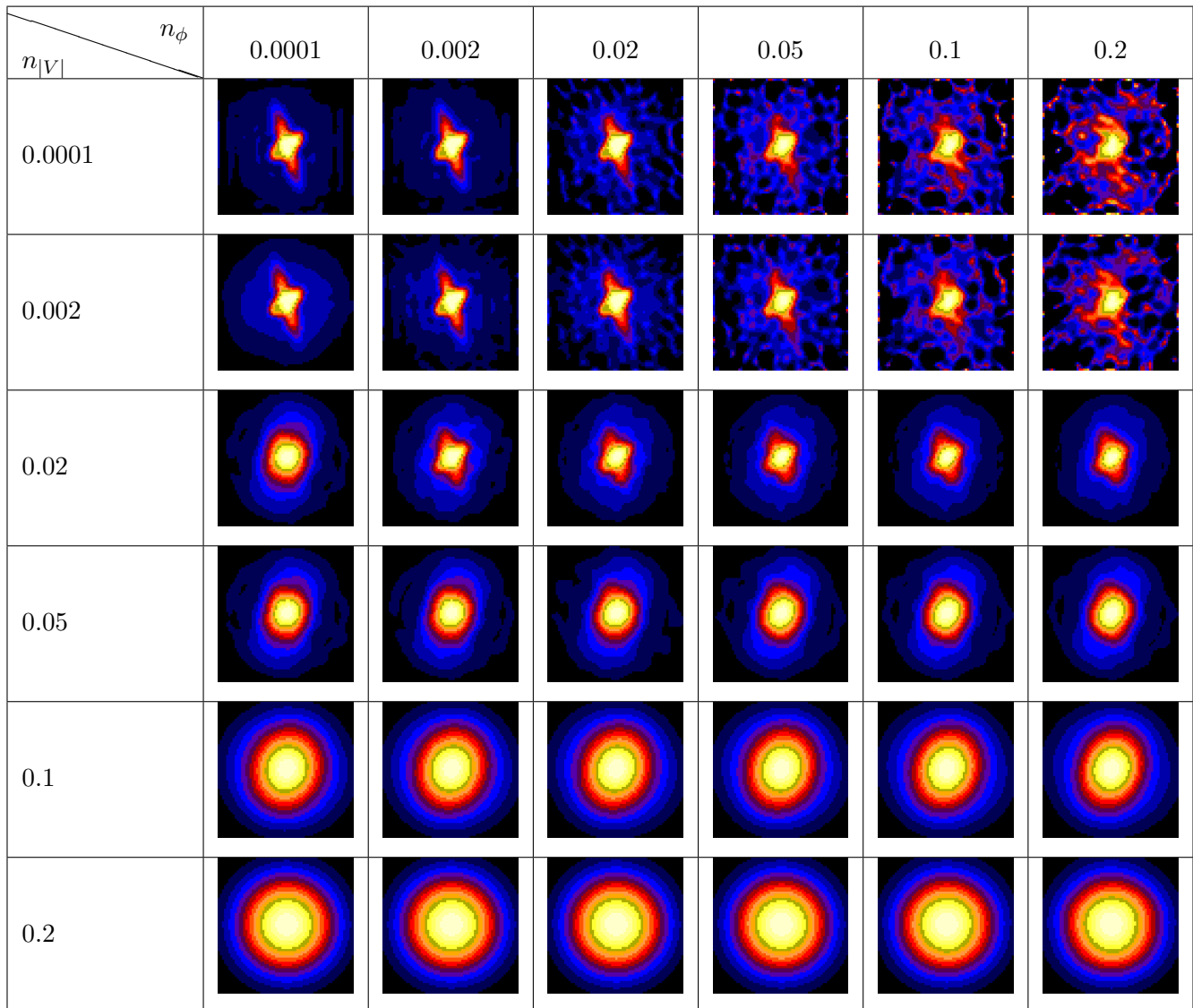
Figure 26: Reconstructed object 6 for several noise parameters, array configuration with 8 telescopes.

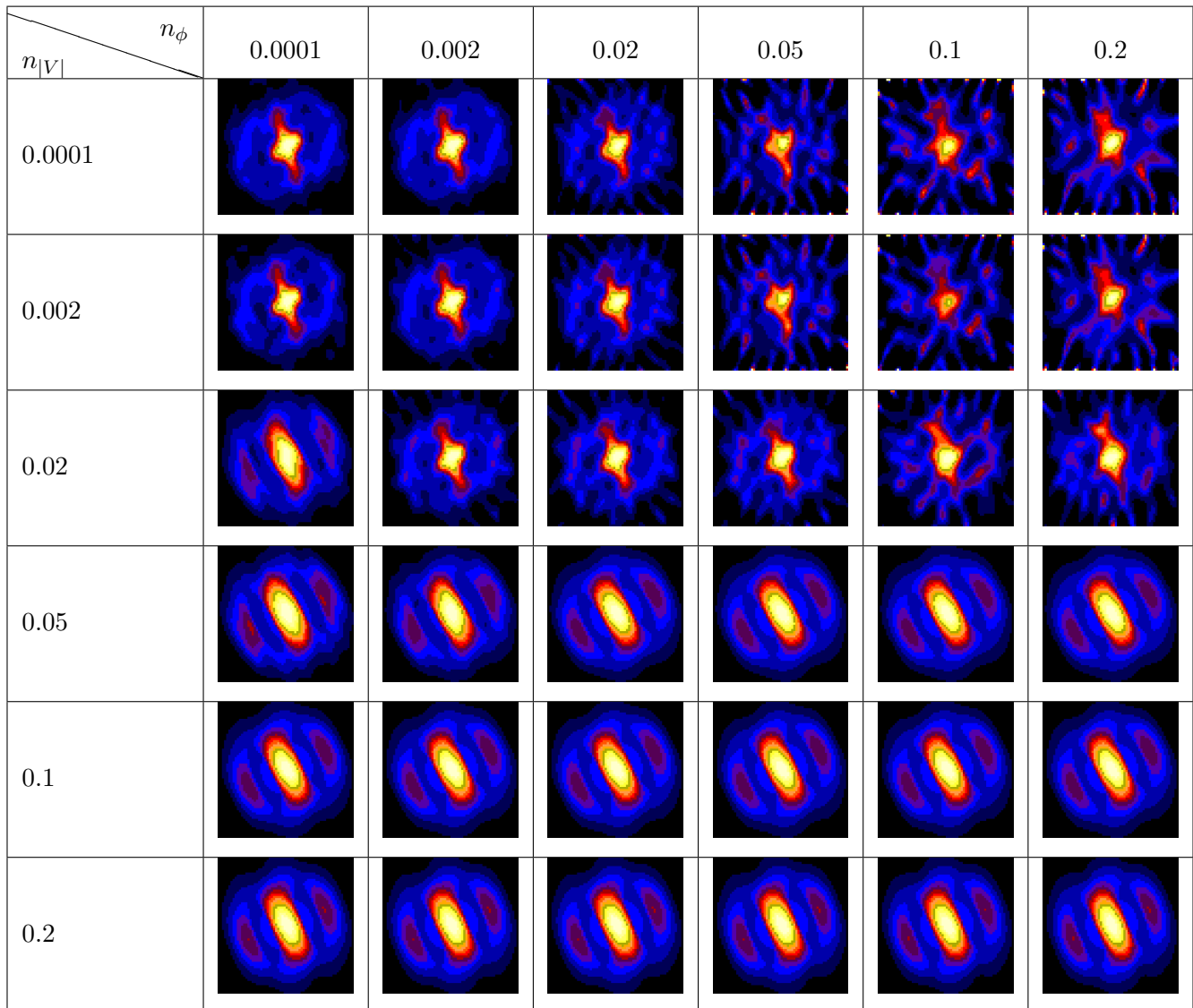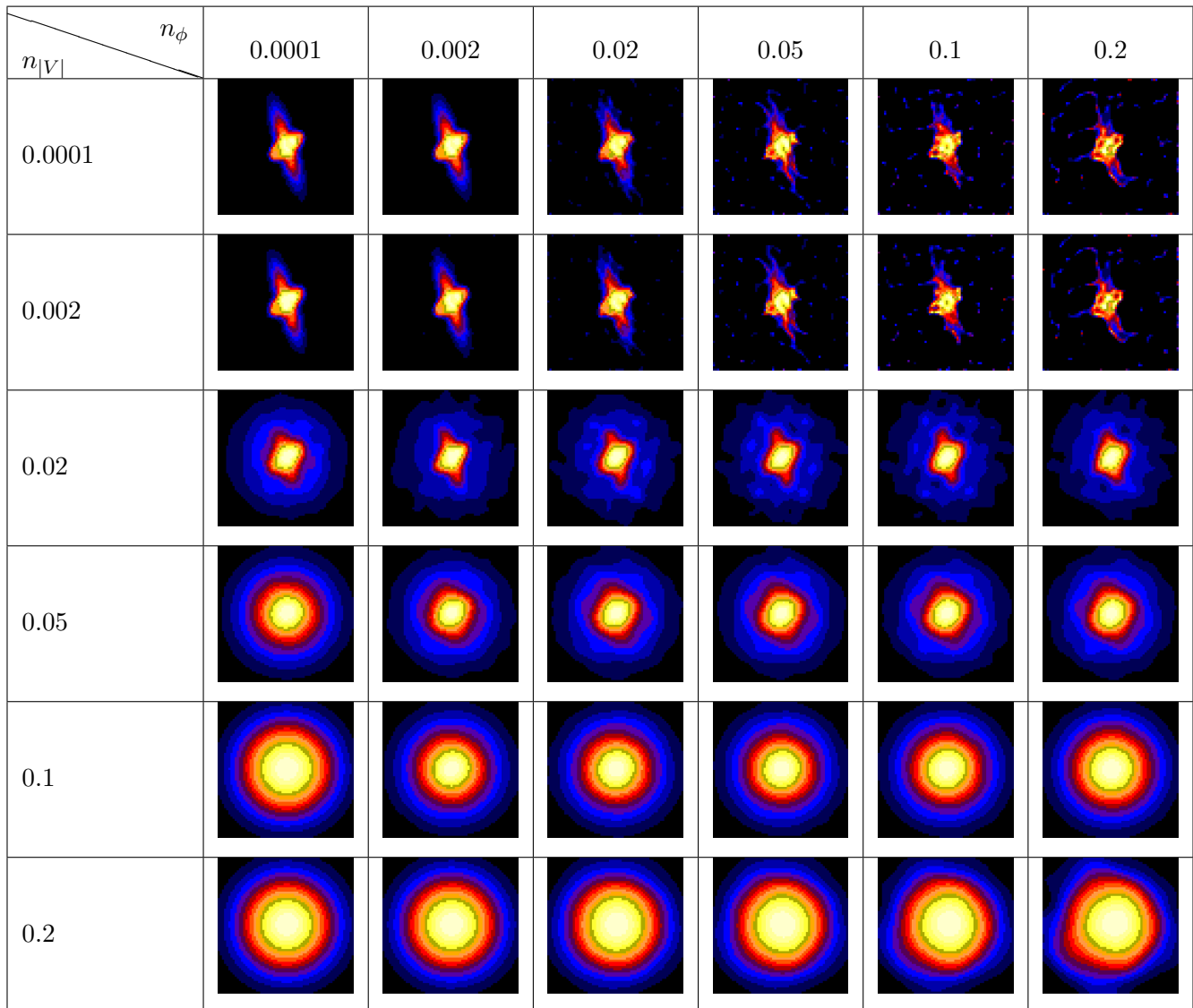Figure 27: Reconstructed object 6 for several noise parameters, array configuration with 15 telescopes.
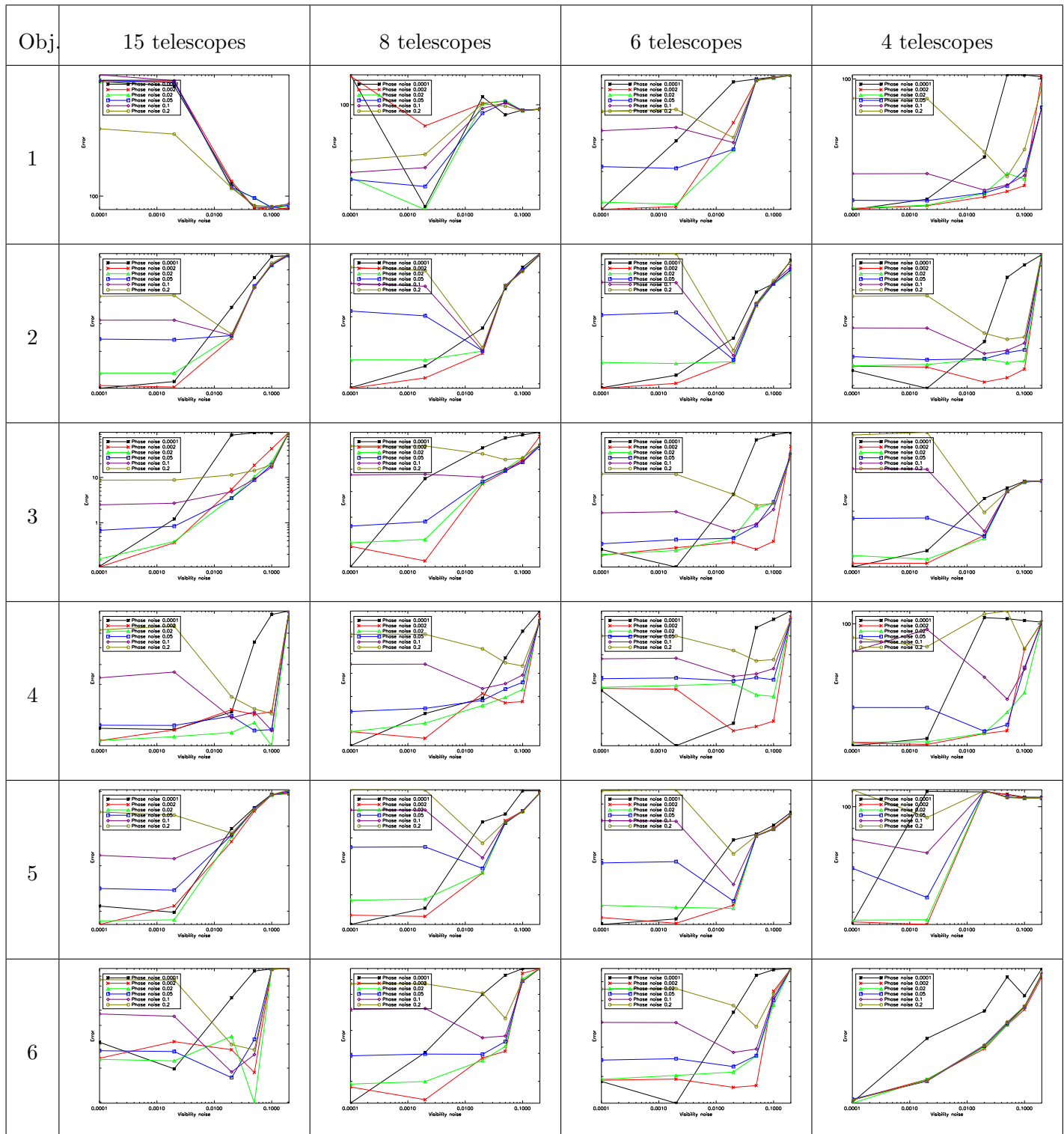
Figure 28: Error vs amplitude noise.

Obj.	15 telescopes	8 telescopes	6 telescopes	4 telescopes
1				
2				
3				
4				
5				
6				
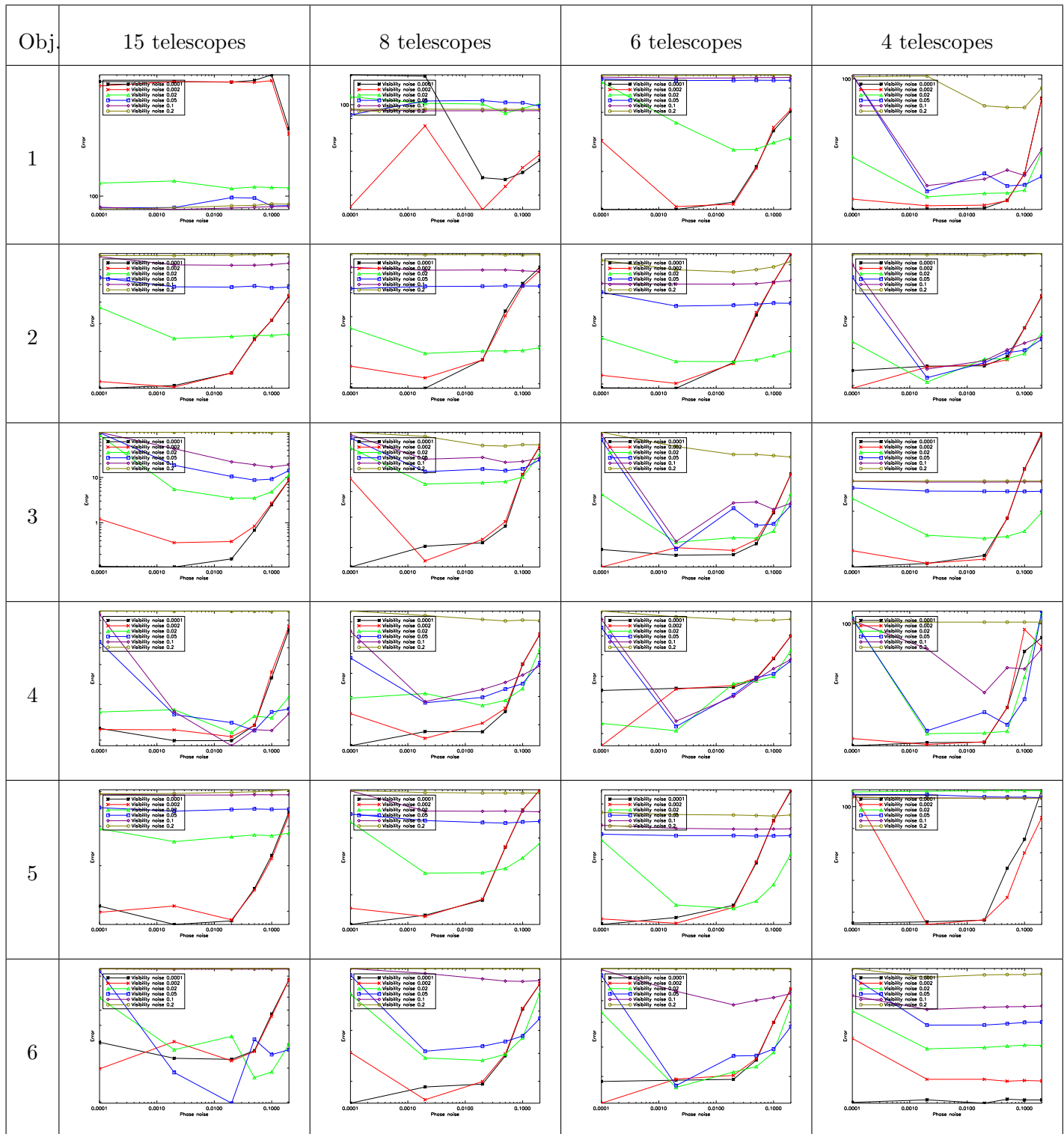
Figure 29: Error vs phase noise.

Obj.	15 telescopes	8 telescopes	6 telescopes	4 telescopes
1				
2				
3				
4				
5				
6				

Figure 30: Standard deviation vs amplitude noise.
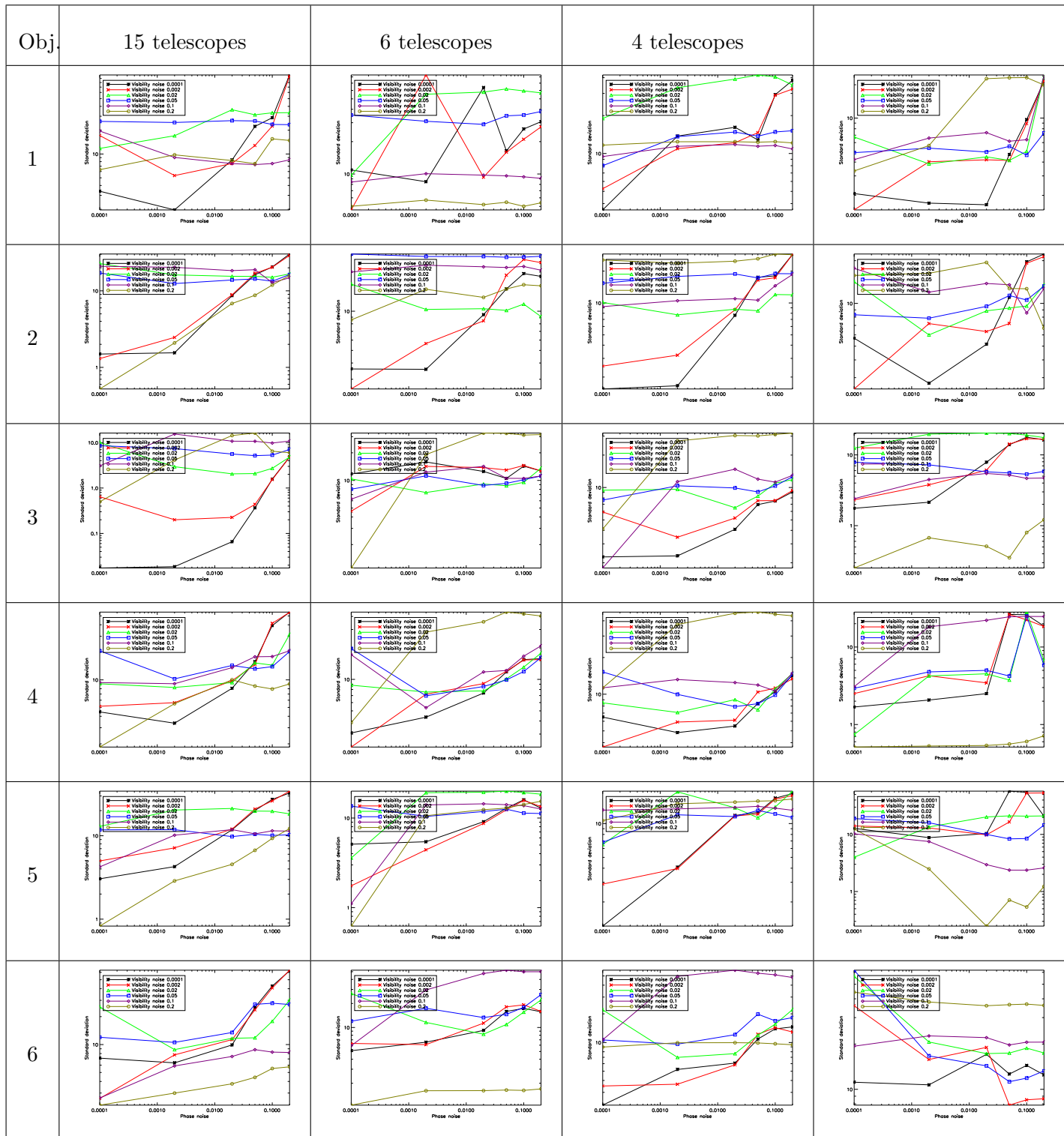
Figure 31: Standard deviation vs phase noise.

4.2 Effect of missing powerspectrum/bispectrum

The following simulations show how reconstruction is affected by missing data, and the relative importance of bispectrum and powerspectrum for the reconstruction for all telescope configurations.

Observations conditions were made by supposing for each array the complete acquisition of bispectrum/powerspectrum in 15 minutes. If n is the number of telescopes of the current array configuration, then there are $n(n-1)/2$ powerspectrum and $(n-1)(n-2)/2$ bispectrum points in each of these acquisitions. The simulated observation was assumed extending on a period of 4 hours, during which 16 sets of powerspectrum/bispectrum would be acquired.

During the reconstruction only a fraction of the total bispectrum (resp. powerspectrum) was used with values at 0%, 25%, 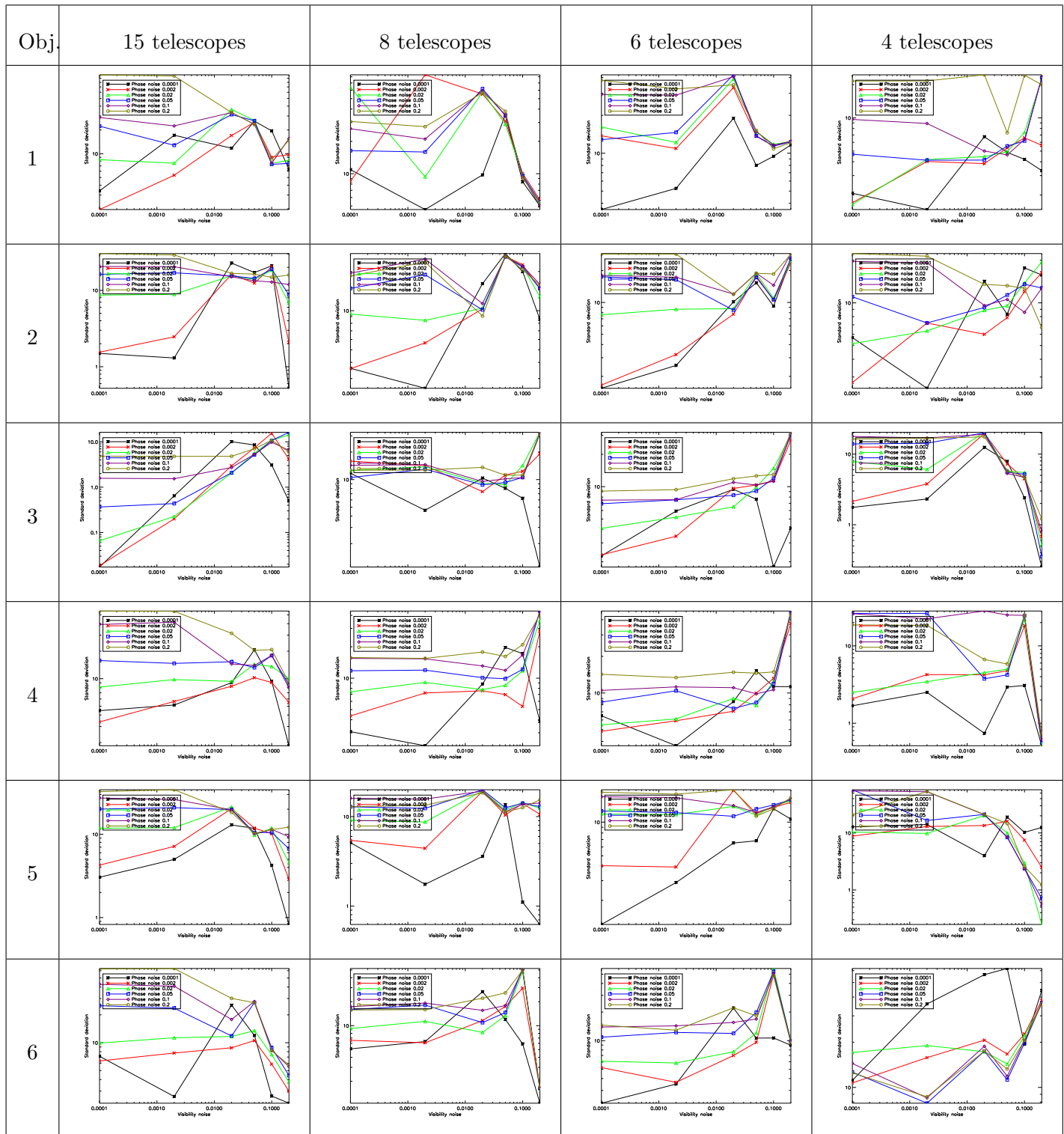50%, 75%, 100%, while using all the powerspectrum (resp. bispectrum) data. Part of the reconstructed images (one per set of parameter) are shown on the next pages with a colour table enhancing their main features in warmer colours.

Performance graphs related to these simulations are also shown on figure 32 33 and 34 to underline unobvious improvements (to the eye) on the reconstruction. On each graph two error curves are presented, respectively the error vs the bispectrum percentage used for reconstruction (in red) and the error vs the powerspectrum percentage (in black). Without noise discrepancy between bispectrum and powerspectrum, the reconstruction error would be a decreasing monotonous function of the bispectrum and powerspectrum percentages. However the SNR of each sort of data can influence the performance, which will be discussed in section 4.2.2. To determine this effect, several noise levels were chosen for visibility amplitudes (affecting mainly powerspectrum and bispectrum amplitudes) and visibility phases (affecting closure phases). Figure 32 is for reasonably high SNR on visibility amplitudes and phases. Figure 33 is for high SNR on visibility amplitudes and low SNR on phases. Figure 33 is for low SNR on visibility amplitudes and high SNR on phases.

In a real interferometer, bispectrum points are expected to be more difficult to acquire than powerspectrum, so the main feature of the graphs is the red curve (though the black one is still useful to improve our understanding of BSMEM behaviour). The bispectrum curve and the powerspectrum curve share a common point at 100%, corresponding to the use of the full data set. Thus at 0% the performance of reconstructions using only powerspectrum (red curve at 0%) and only bispectrum (black curve at 0%) can be compared.

In general the plots show that performance remains stable after a 50% threshold, meaning that in most cases less than 50% of bispectrum (or powerspectrum) are really needed when the other kind of data is fully available.

4.2.1 Influence of target symmetry

Bispectrum and powerspectrum relative importance for a given reconstruction is strongly linked to the amount of symmetry the observed target displays. Visibilities for a symmetric object are real, and when thus bispectrum do not really provide additional information to powerspectrum data.

Thus one might think powerspectrum on its own is enough to reconstruct point-symmetric sources, and that bispectrum data become relevant only when the target is asymmetric. However such statements are based on the assumption that you know the degree of symmetry of your source, which is only possible if any least some phases have been secured on this target (or if the target shape was previously partially known). Data sets containing predominantly powerspectrum but with a few bispectrum data points contains often enough information about the source asymmetries to ensure a correct reconstruction.

In general – keeping in mind that natural sources are never perfectly point-symmetric – the powerspectrum data can be considered as an indication of the amount of flux present in the symmetrized object, while the bispectrum provides the exact localisation of this flux in its non-symmetric parts. As expected, simulation results on the point-symmetric test objects (5 and 6) show that reconstructions using only powerspectrum always give better performance than those using bispectrum only.

When reconstructing a non-symmetric object, however, the situation is different. The problem of reconstruction from powerspectrum only is mathematically undetermined so that both the image of the target and the symmetric image can be indifferently retrieved (or an image sharing characteristics with both).

This is the case for example of object 4 at 0% bispectrum in figure 44. Examination of the reconstructions on figure 38 clearly reveals that with very few bispectrum points (0% and 25%) the reconstructed image is a superposition of the true solution with its symmetric. Even a full *uv* coverage is unable to prevent this effect (figure 39).

Thus a reconstruction from bispectrum only is generally preferable to a reconstruction from powerspectrum only. Off course, as more bispectrum are used, the indetermination is progressively lifted, so that a set containing mostly powerspectrum plus a few bispectrum becomes equivalent performance-wise to a set containing mostly bispectrum plus a few bispectrum. An interesting comparison between the results of figure 41 and figure 59 shows that the disk structure (though inherently symmetric) appears sooner when using mostly bispectrum information.

4.2.2 Influence of the SNR

In the previous noise study (section 4.1) an increasing phase noise was shown to degrade the reconstruction by creating delocalised noise on the image, but without ever preventing the convergence to a solution. If bispectrum are noisier (in fact the phases of the bispectrum) than the corresponding powerspectrum (visibility amplitudes), will their use still improve the reconstruction ? If yes, in which proportion can they be used ? These questions become important when very few bispectrum points are available on an object, or are known to be partially incorrect.

In simulations, performance on punctual objects (or nearly punctual, those are objects 1, 2, and 4) do not vary much, which demonstrates that high SNR on either the bispectrum or the powerspectrum is sufficient to insure a good reconstruction (as long as the symmetry ambiguity is lifted). One can note that, on object 4, reconstruction with high SNR on powerspectrum and low SNR on bispectrum (figure 46) is more precise than the reverse case (figure 45), with a faint additional star visible.

On other objects a minor improvement in reconstruction quality is noted as low SNR bispectrum are progressively added to high SNR powerspectrum (figure 43, especially on the 6 telescope example). On the other hand, there is a dramatic degradation when high SNR bispectrum are added to low powerspectrum SNR, up to the point where the spot are not visible any more (figure 43, figure 52). The situation is different with powerspectrum : whichever their SNR relatively to closure phases, performance is improved overall.

4.2.3 Conclusion on bispectrum/powerspectrum study

As expected, and as confirmed by section 4.1.4, the overall *uv* coverage is the most determining factor in final performance of the reconstruction. However requirements on bispectrum and powerspectrum coverage do vary with the nature of the observed target. Securing bispectrum points is of the utmost importance with targets known to be strongly asymmetric, while on the contrary powerspectrum should be the priority on objects thought to be roughly point-symmetric.

The reconstruction error is not always a monotonous function of bispectrum/powerspectrum percentage, therefore a reconstruction with optimal bispectrum coverage but average *uv* coverage may be superior to one obtained with better *uv* coverage but with a poor bispectrum sampling.

A small amount of bispectrum is definitely required to remove the symmetry ambiguity which exists in non point-symmetric targets. Closure phases of reasonable SNR are sufficient, as contrary to the intuition, closure phases of much higher SNR than the powerspectrum do not necessarily improve the reconstruction, and can sometimes prevent BSMEM from converging.
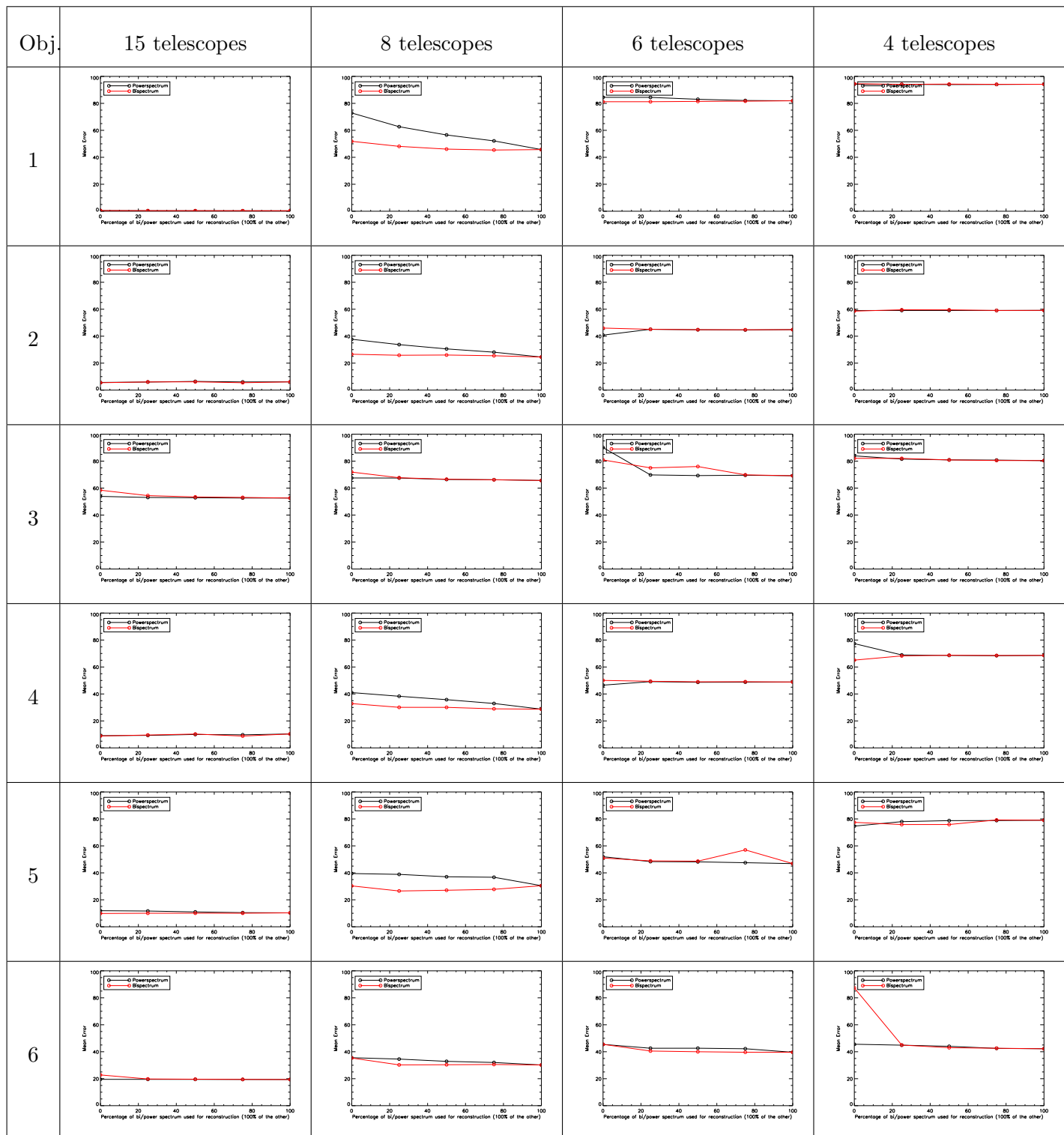
Figure 32: Bispectrum and Powerspectrum influences. High SNR on visibility amplitude and phase.
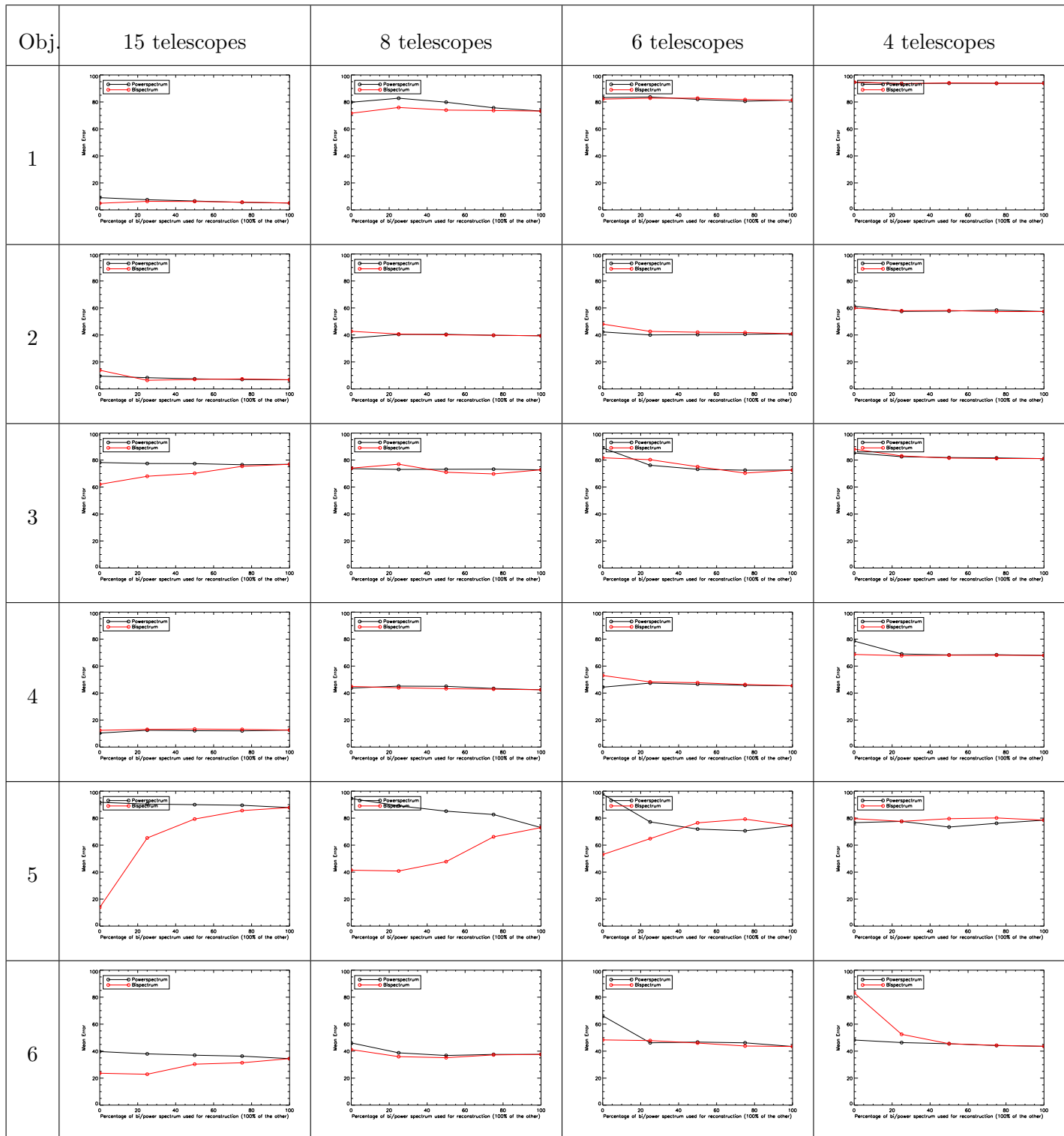
Figure 33: Bispectrum and Powerspectrum influences. Low SNR on amplitudes, high SNR on phases.
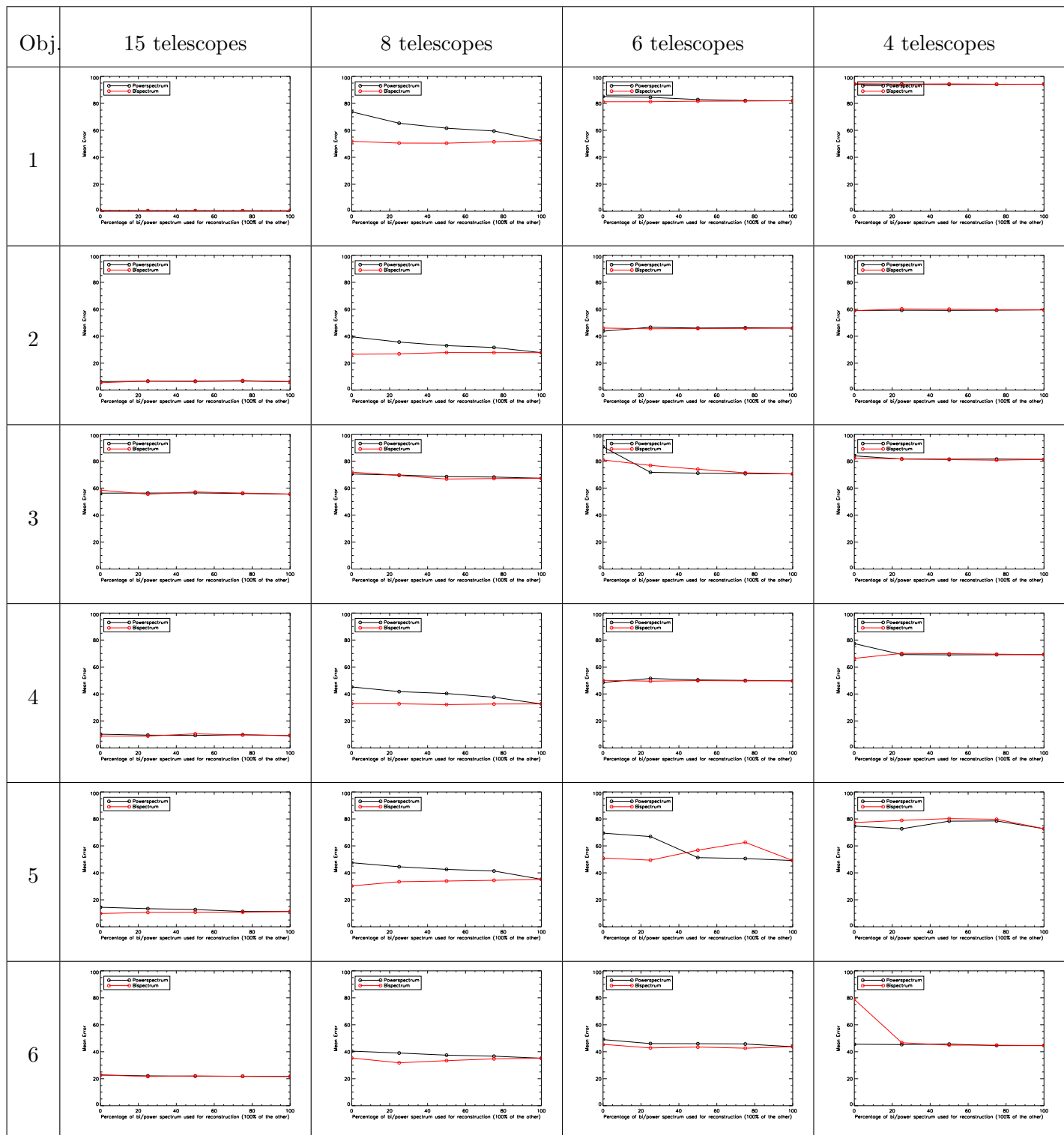
Figure 34: Bispectrum and Powerspectrum influences. Good SNR on amplitudes, low SNR on phases.

Bis.	15 telescopes	8 telescopes	6 telescopes	4 telescopes
0%				
25%				
50%				
75%				
100%				
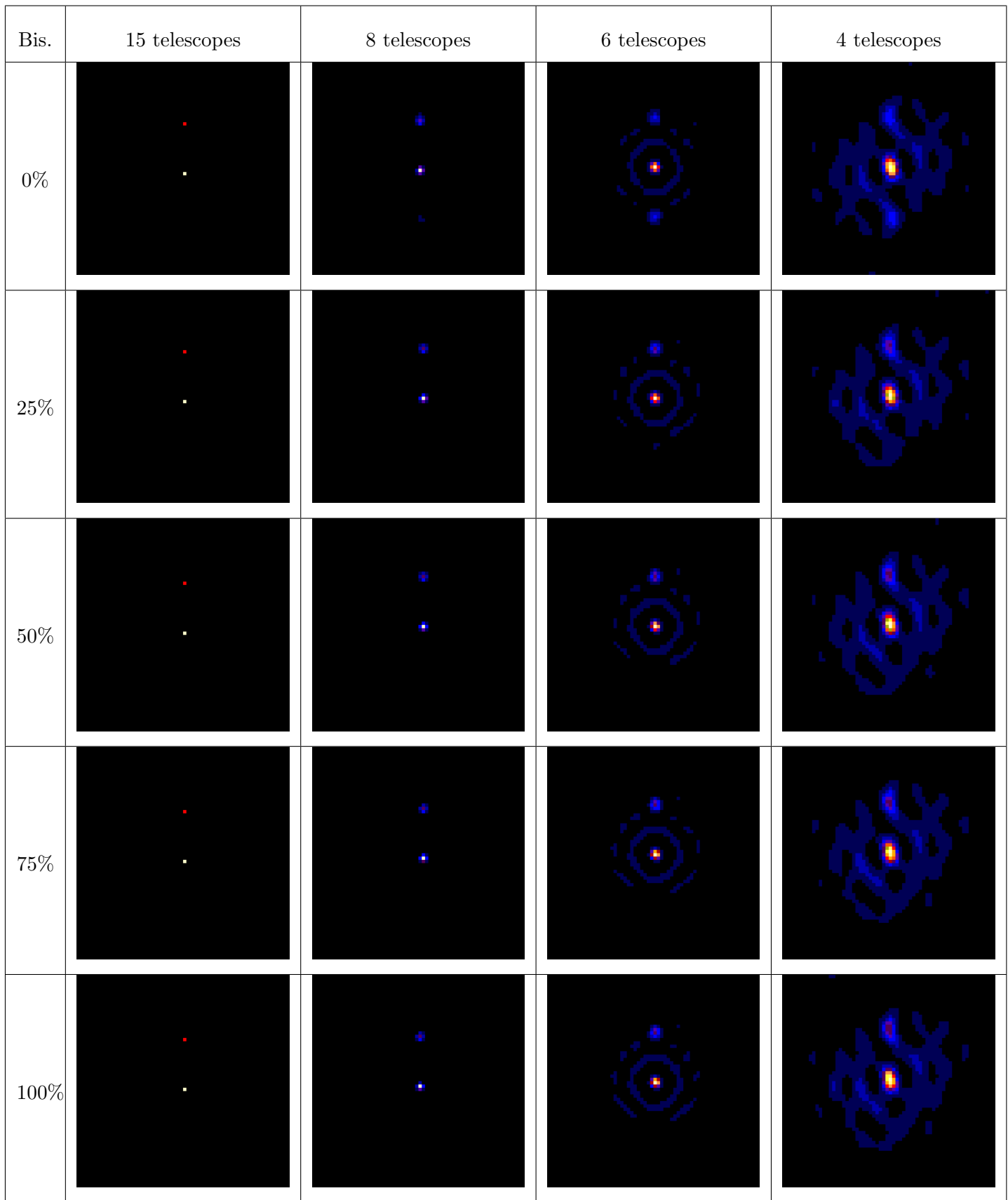
Figure 35: Object 1 at high SNR.

Bis.	15 telescopes	8 telescopes	6 telescopes	4 telescopes
0%				
25%				
50%				
75%				
100%				
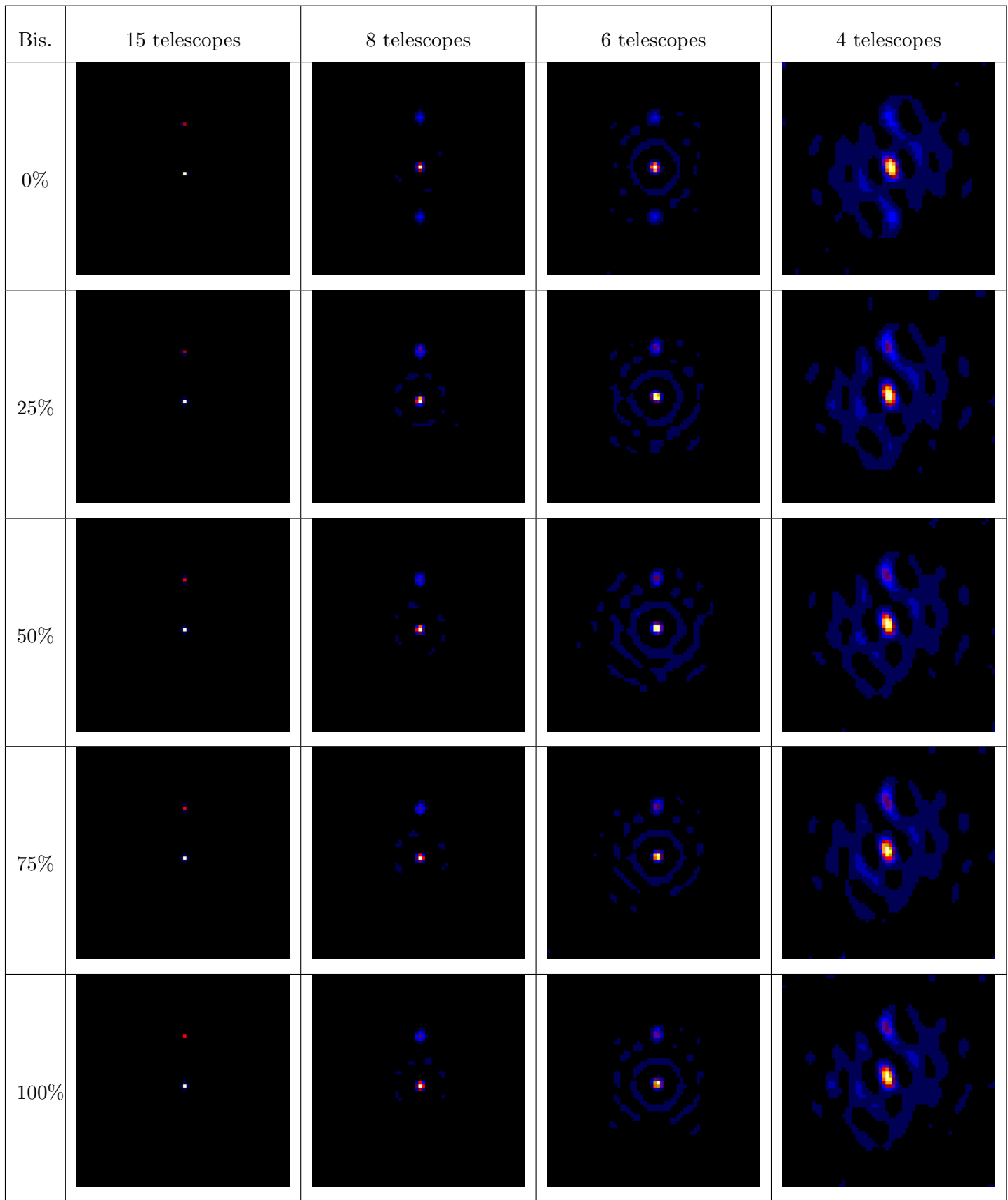
Figure 36: Object 1, low SNR on powerspectrum and high SNR on bispectrum phases.

Bis.	15 telescopes	8 telescopes	6 telescopes	4 telescopes
0%				
25%				
50%				
75%				
100%				
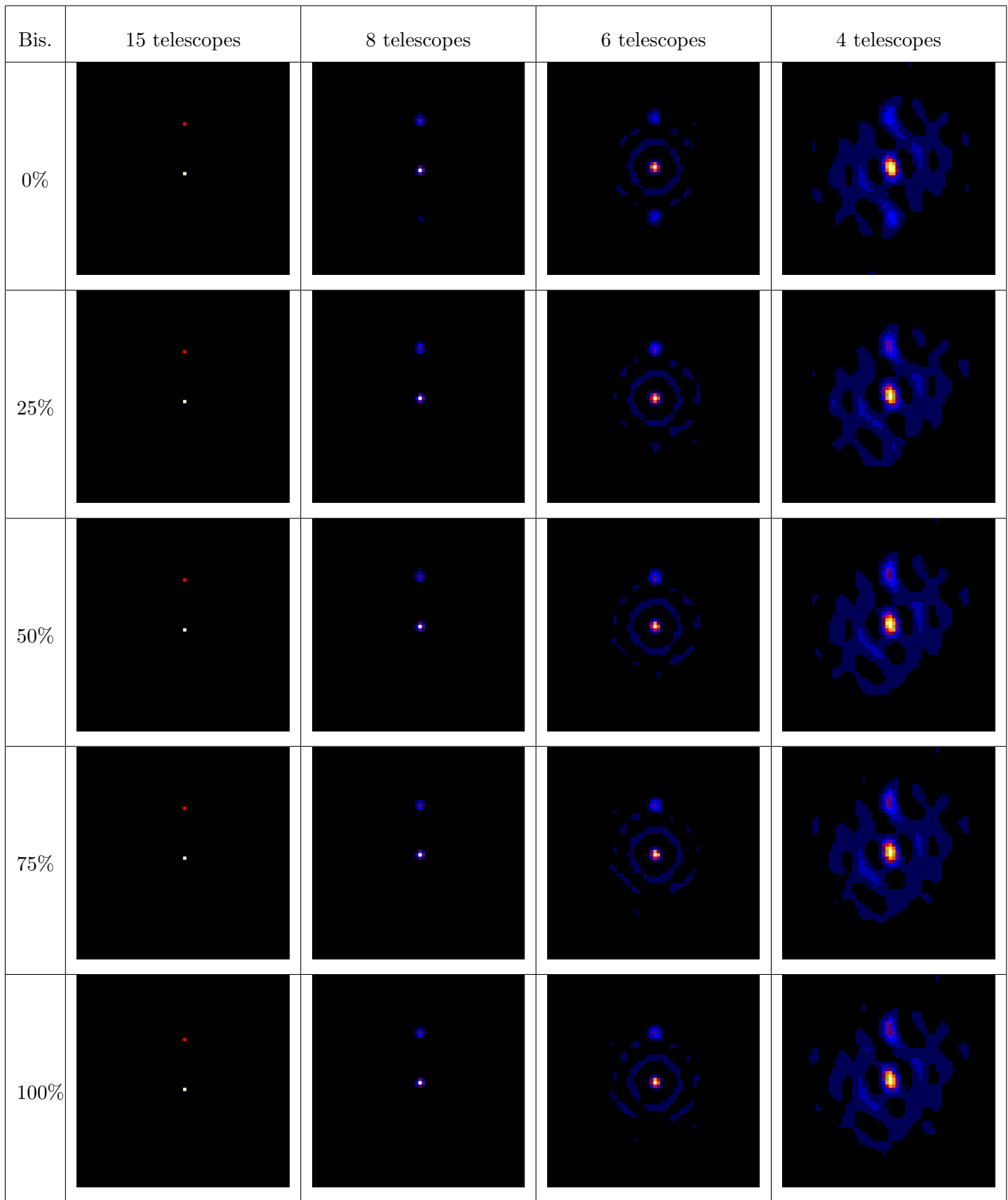
Figure 37: Object 1, high SNR on powerspectrum and low SNR on bispectrum phases.

Bis.	15 telescopes	8 telescopes	6 telescopes	4 telescopes
0%				
25%				
50%				
75%				
100%				
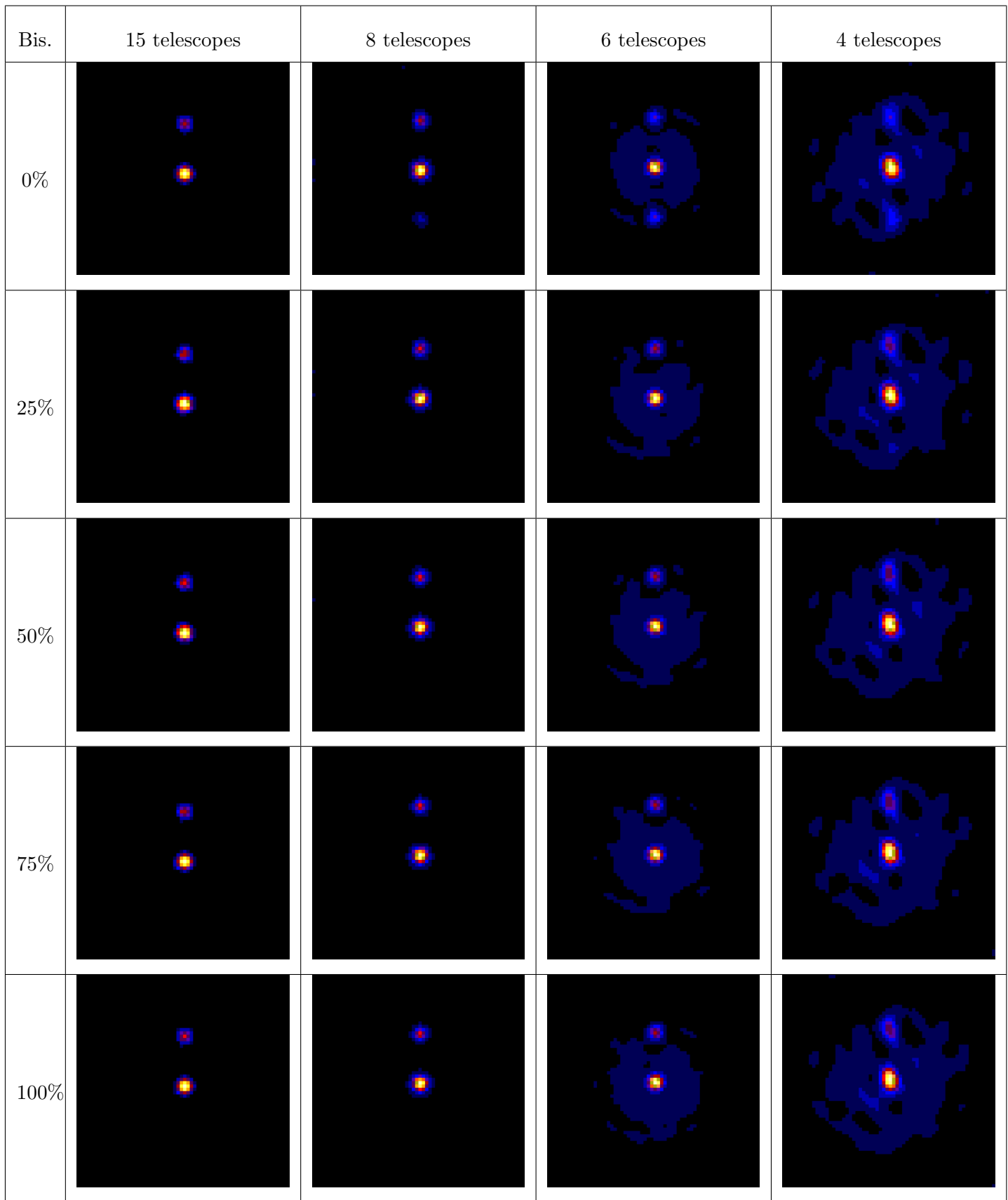
Figure 38: Object 2 at high SNR.
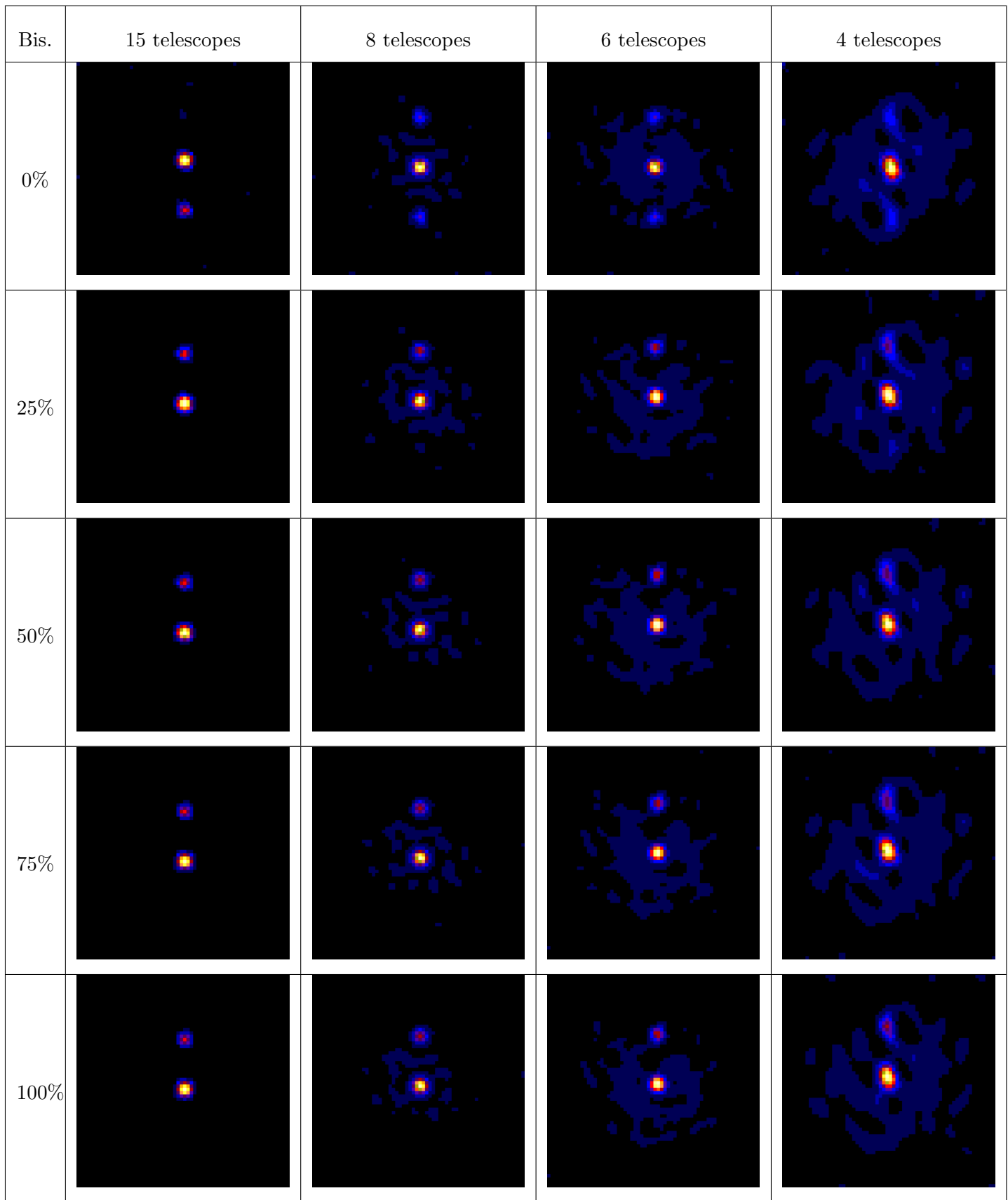
Figure 39: Object 2, low SNR on powerspectrum and high SNR on bispectrum phases.

Bis.	15 telescopes	8 telescopes	6 telescopes	4 telescopes
0%				
25%				
50%				
75%				
100%				
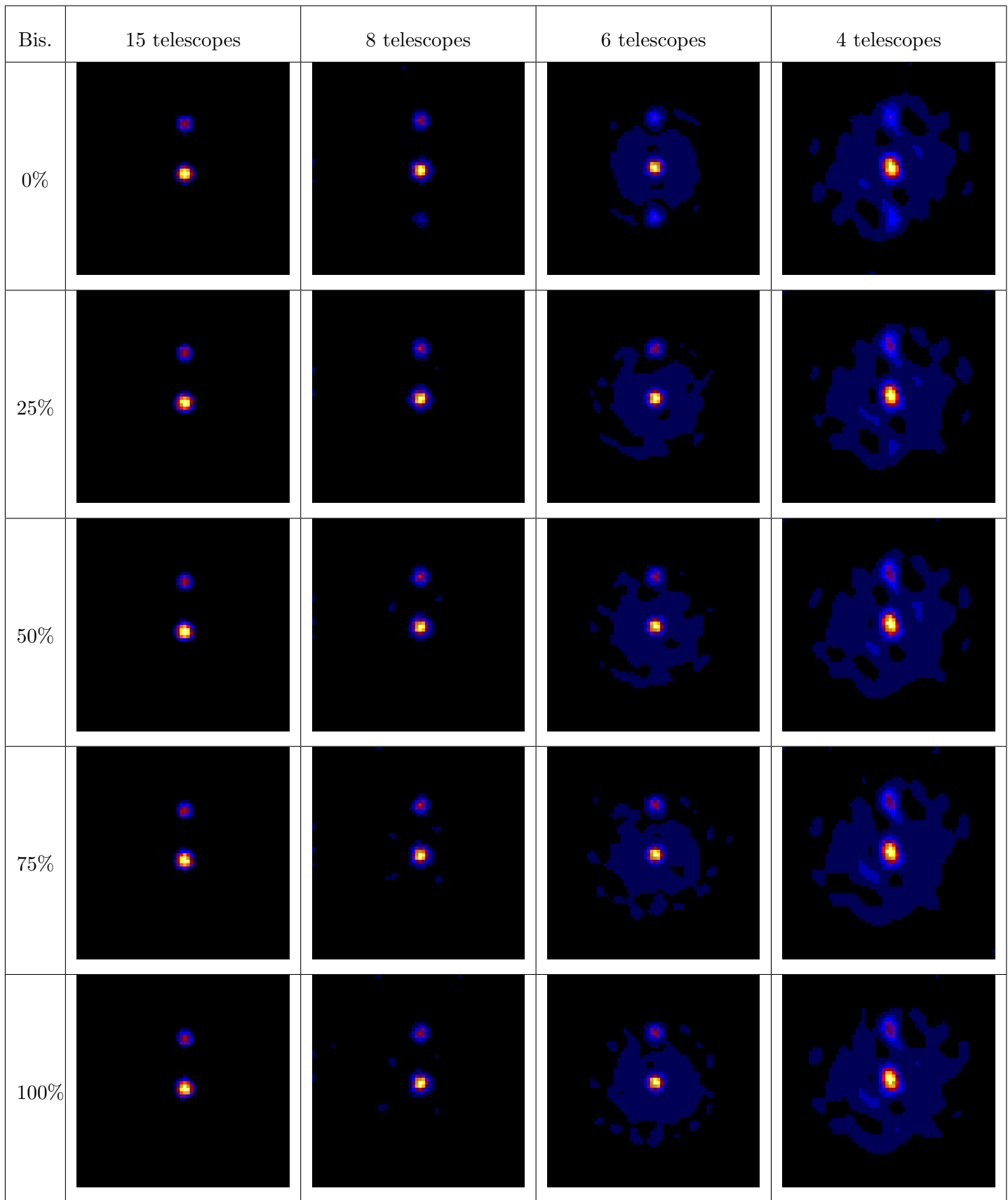
Figure 40: Object 2, high SNR on powerspectrum and low SNR on bispectrum phases.

Bis.	15 telescopes	8 telescopes	6 telescopes	4 telescopes
0%				
25%				
50%				
75%				
100%				
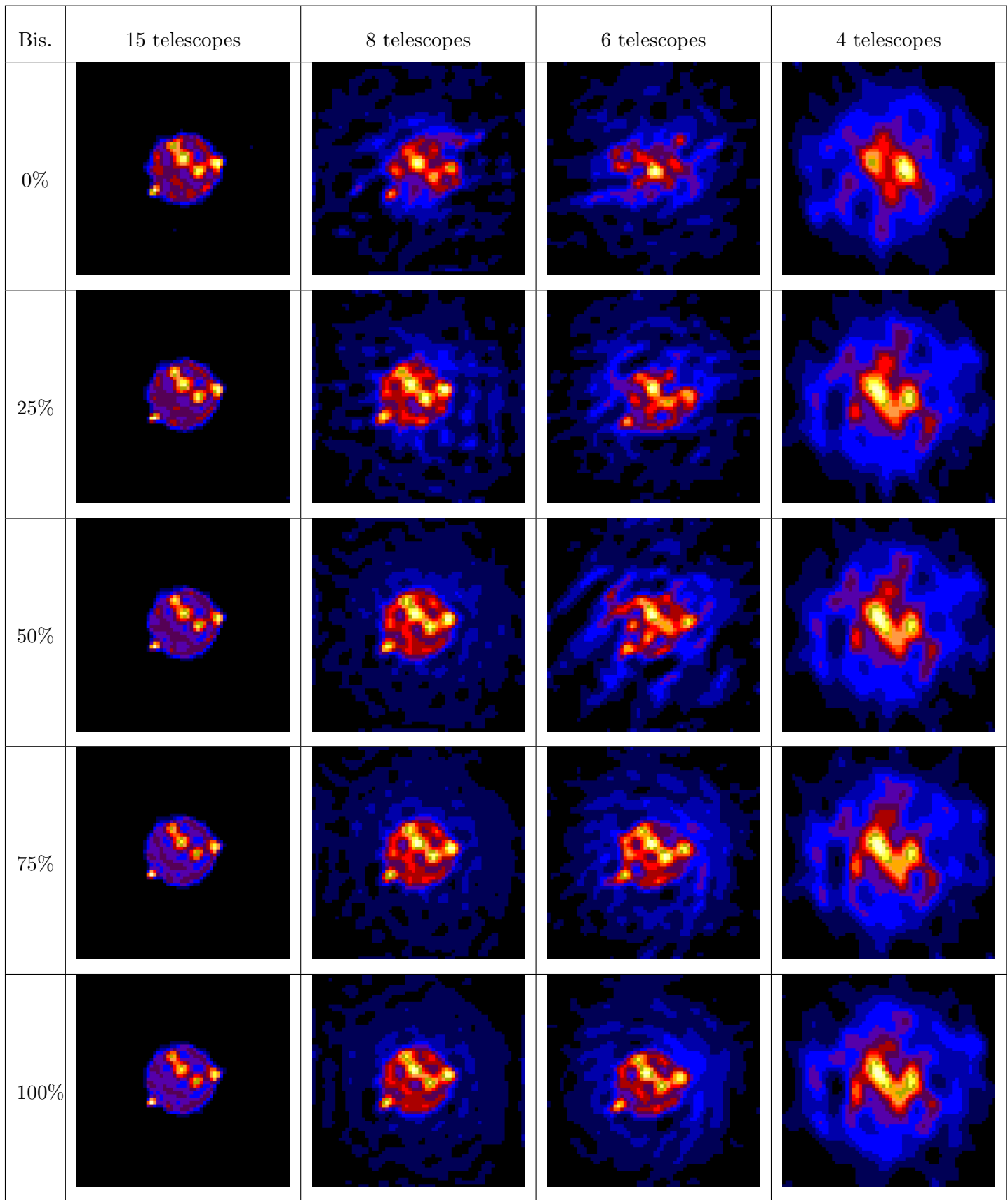
Figure 41: Object 3 at high SNR.

Bis.	15 telescopes	8 telescopes	6 telescopes	4 telescopes
0%				
25%				
50%				
75%				
100%				
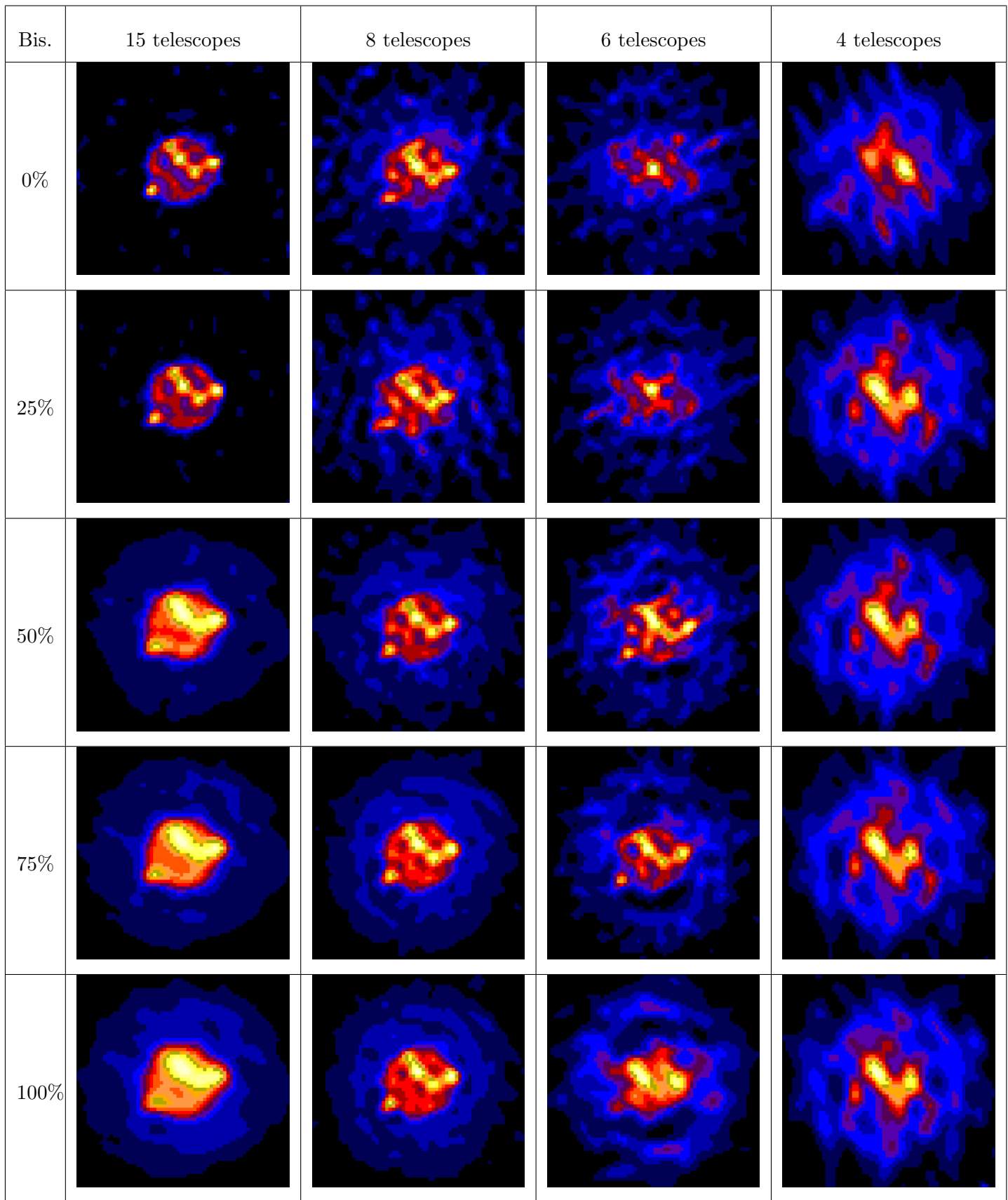
Figure 42: Object 3, low SNR on powerspectrum and high SNR on bispectrum phases.

Bis.	15 telescopes	8 telescopes	6 telescopes	4 telescopes
0%				
25%				
50%				
75%				
100%				
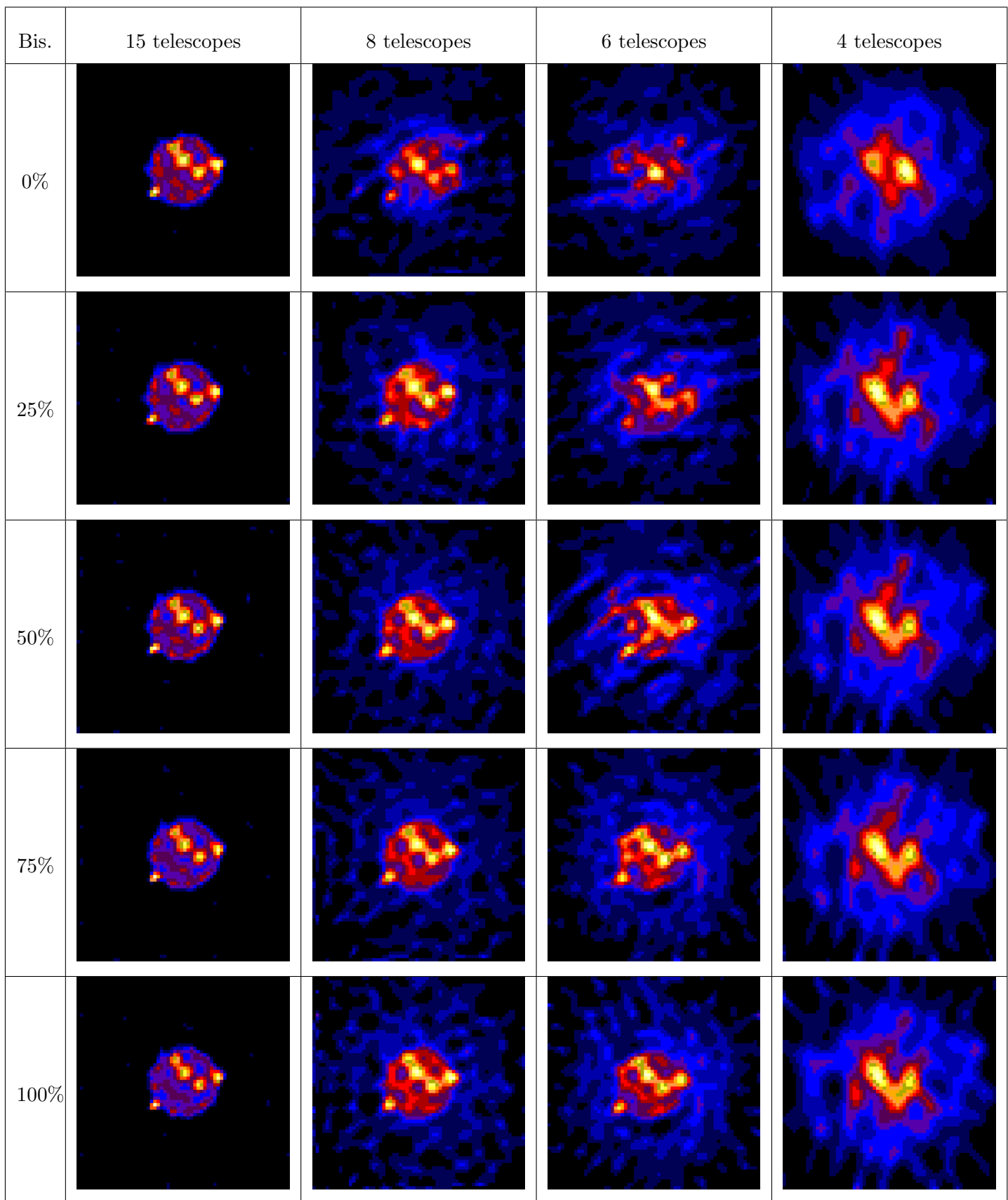
Figure 43: Object 3, high SNR on powerspectrum and low SNR on bispectrum phases.

Bis.	15 telescopes	8 telescopes	6 telescopes	4 telescopes
0%				
25%				
50%				
75%				
100%				
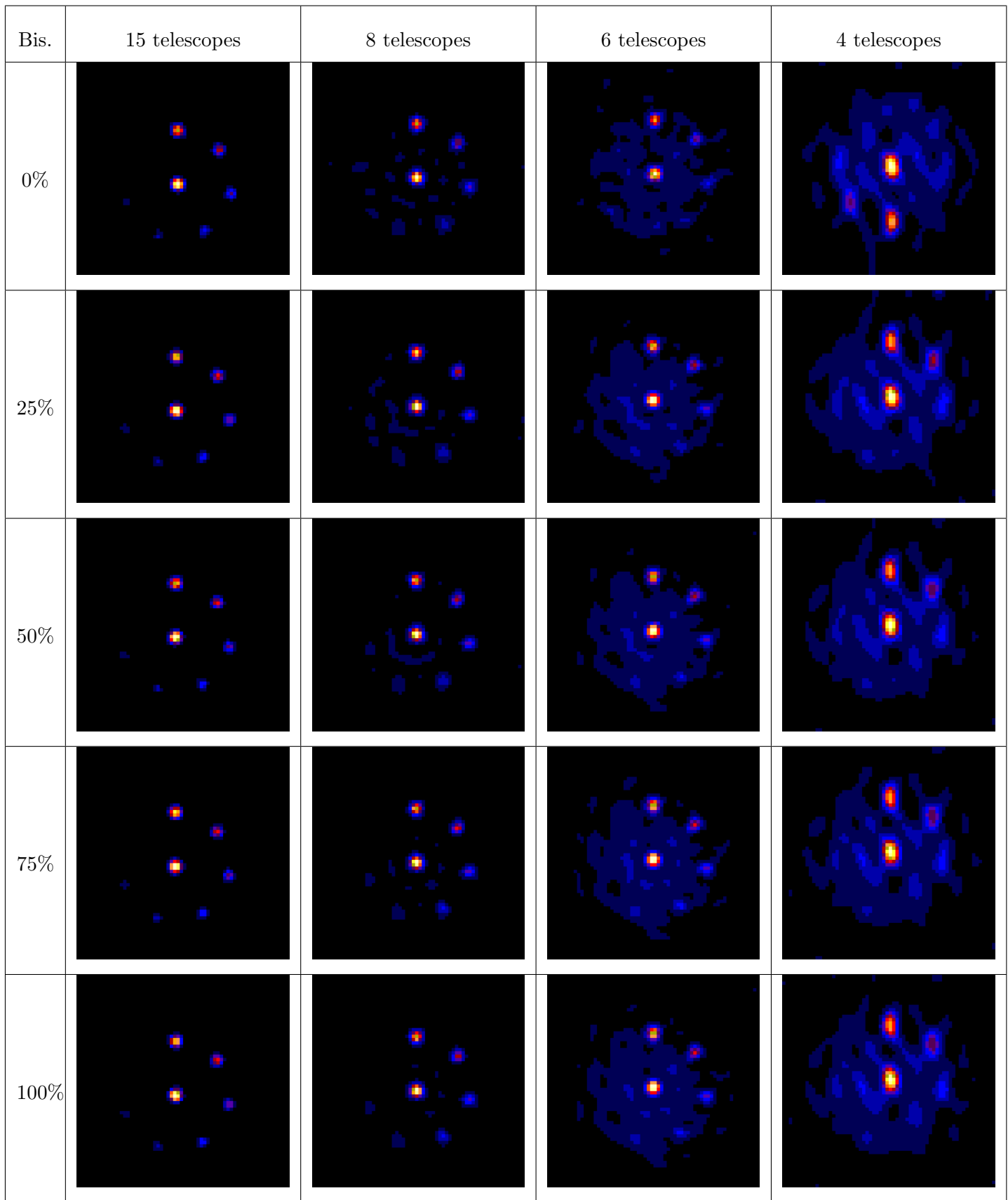
Figure 44: Object 4 at high SNR.

Bis.	15 telescopes	8 telescopes	6 telescopes	4 telescopes
0%				
25%				
50%				
75%				
100%				
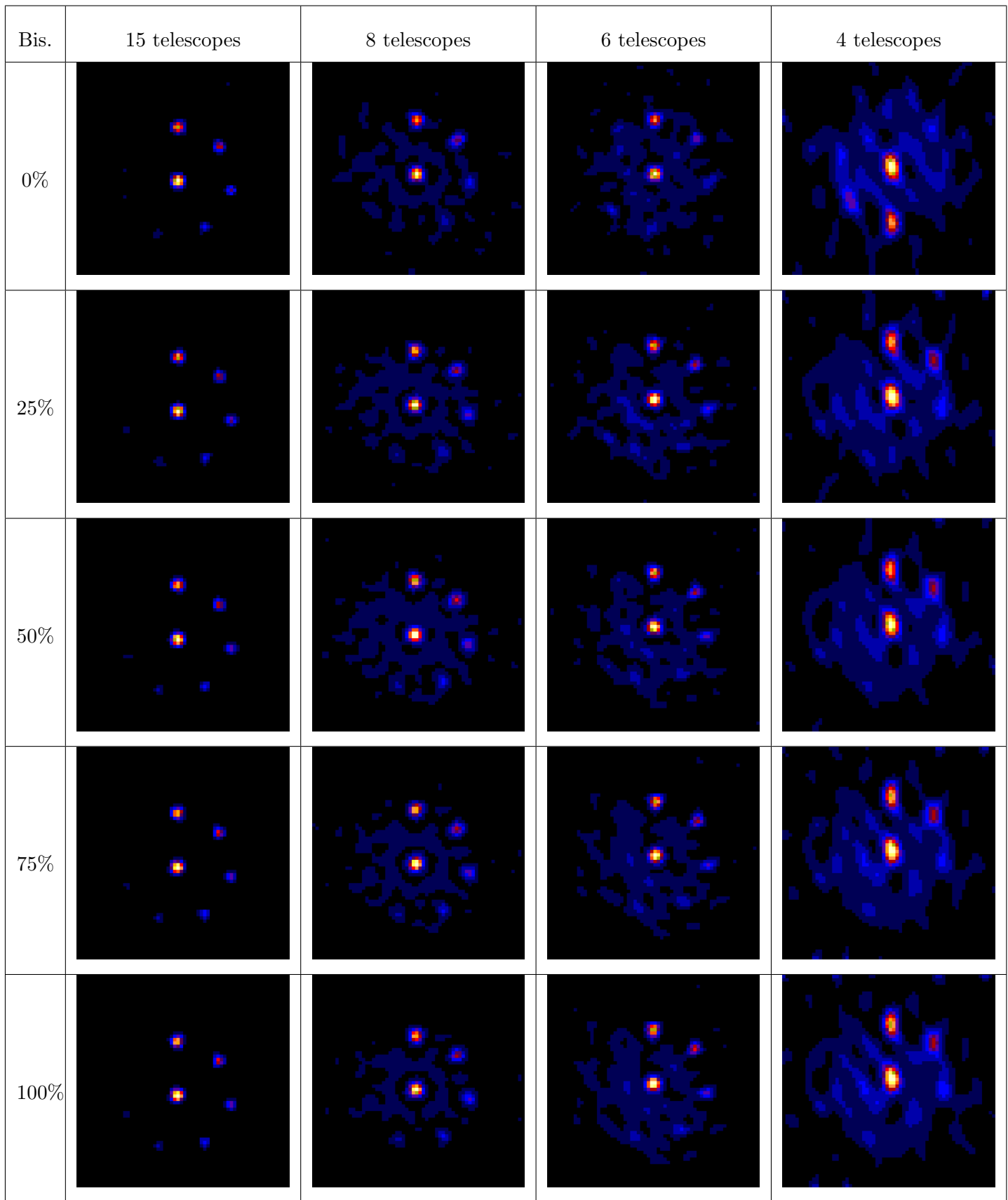
Figure 45: Object 4, low SNR on powerspectrum and high SNR on bispectrum.

Bis.	15 telescopes	8 telescopes	6 telescopes	4 telescopes
0%				
25%				
50%				
75%				
100%				
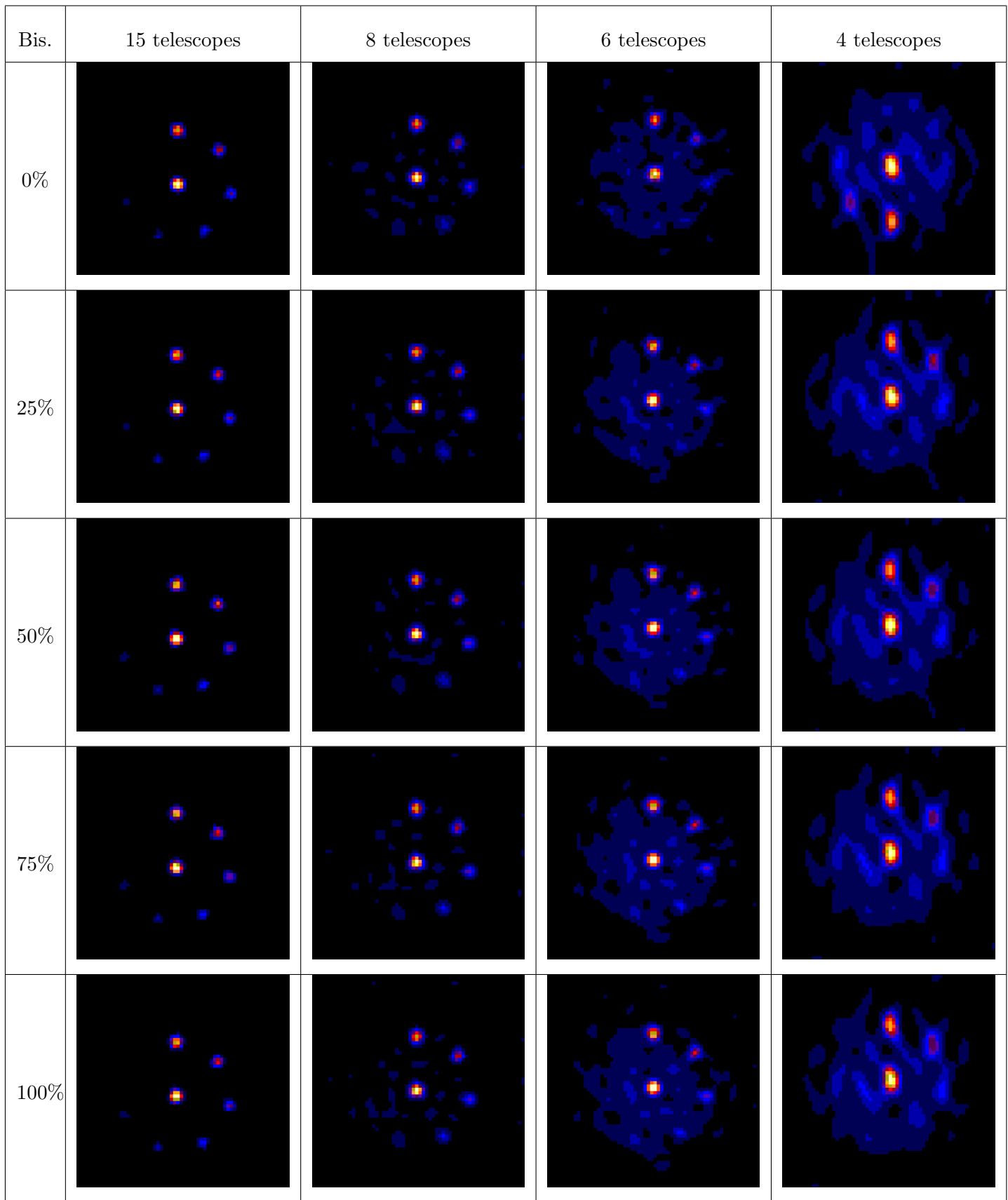
Figure 46: Object 4, high SNR on powerspectrum and low SNR on bispectrum phases.

Bis.	15 telescopes	8 telescopes	6 telescopes	4 telescopes
0%				
25%				
50%				
75%				
100%				
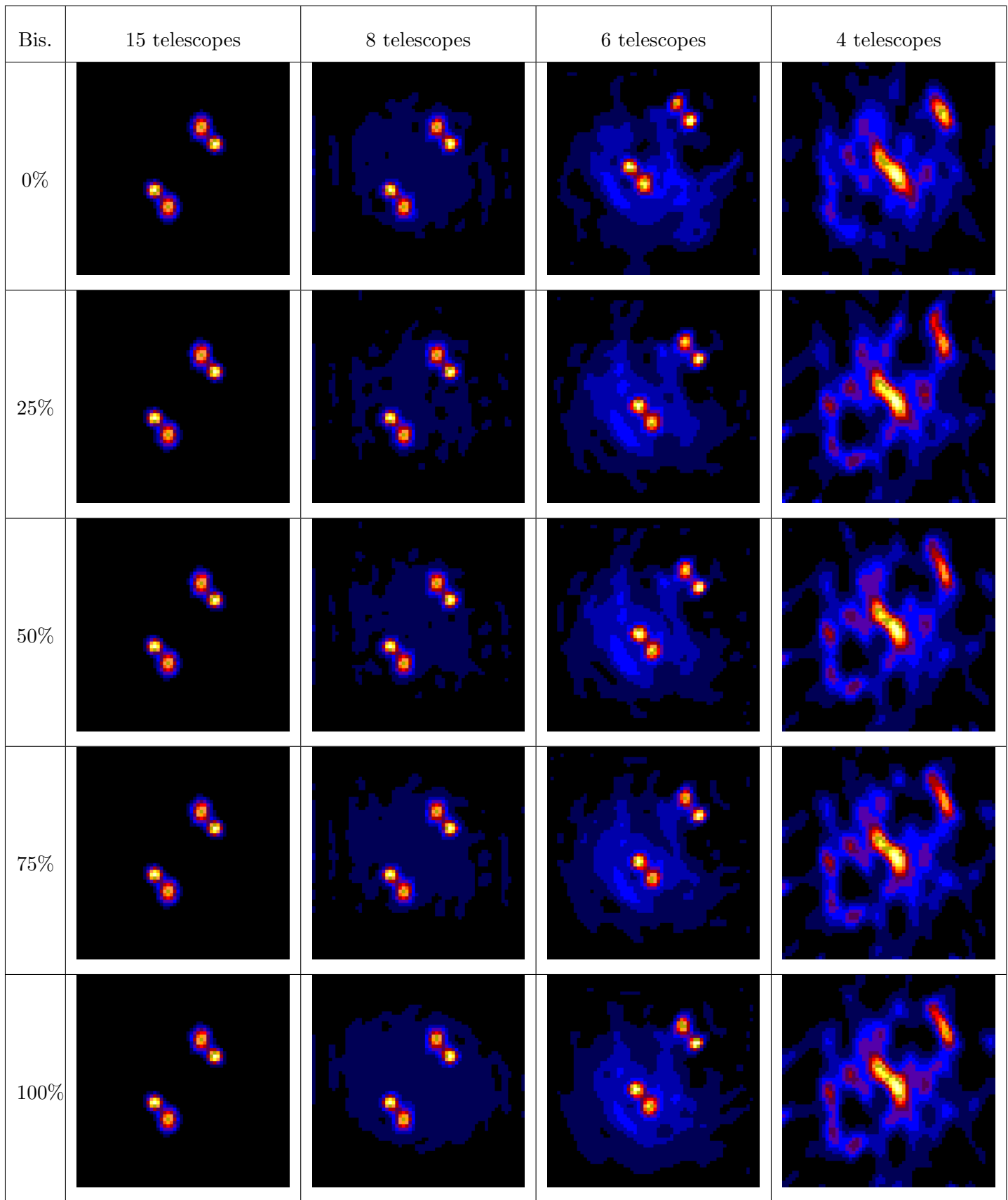
Figure 47: Object 5 at high SNR.

Bis.	15 telescopes	8 telescopes	6 telescopes	4 telescopes
0%				
25%				
50%				
75%				
100%				
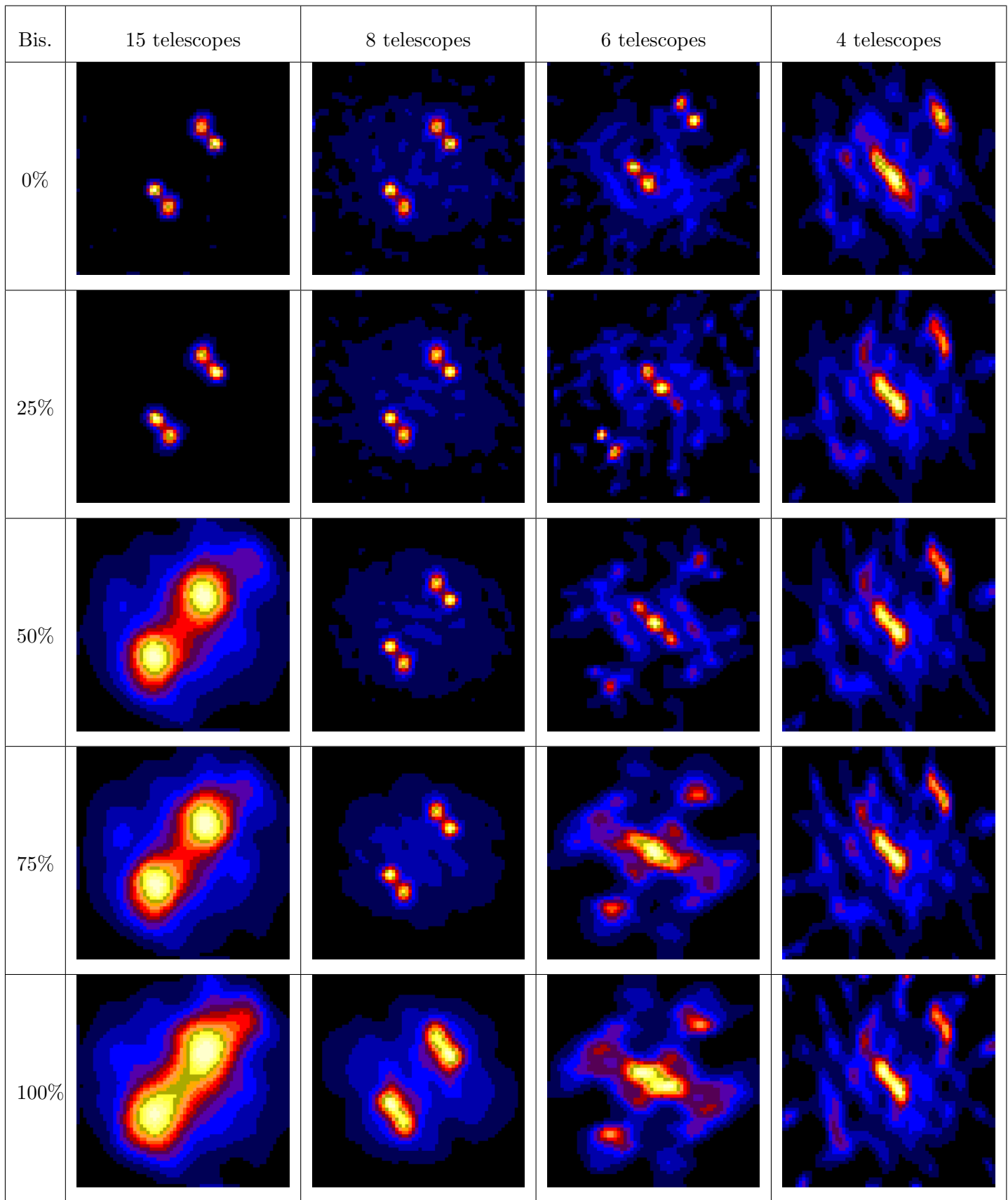
Figure 48: Object 5, low SNR on powerspectrum and high SNR on bispectrum phases.

Bis.	15 telescopes	8 telescopes	6 telescopes	4 telescopes
0%				
25%				
50%				
75%				
100%				
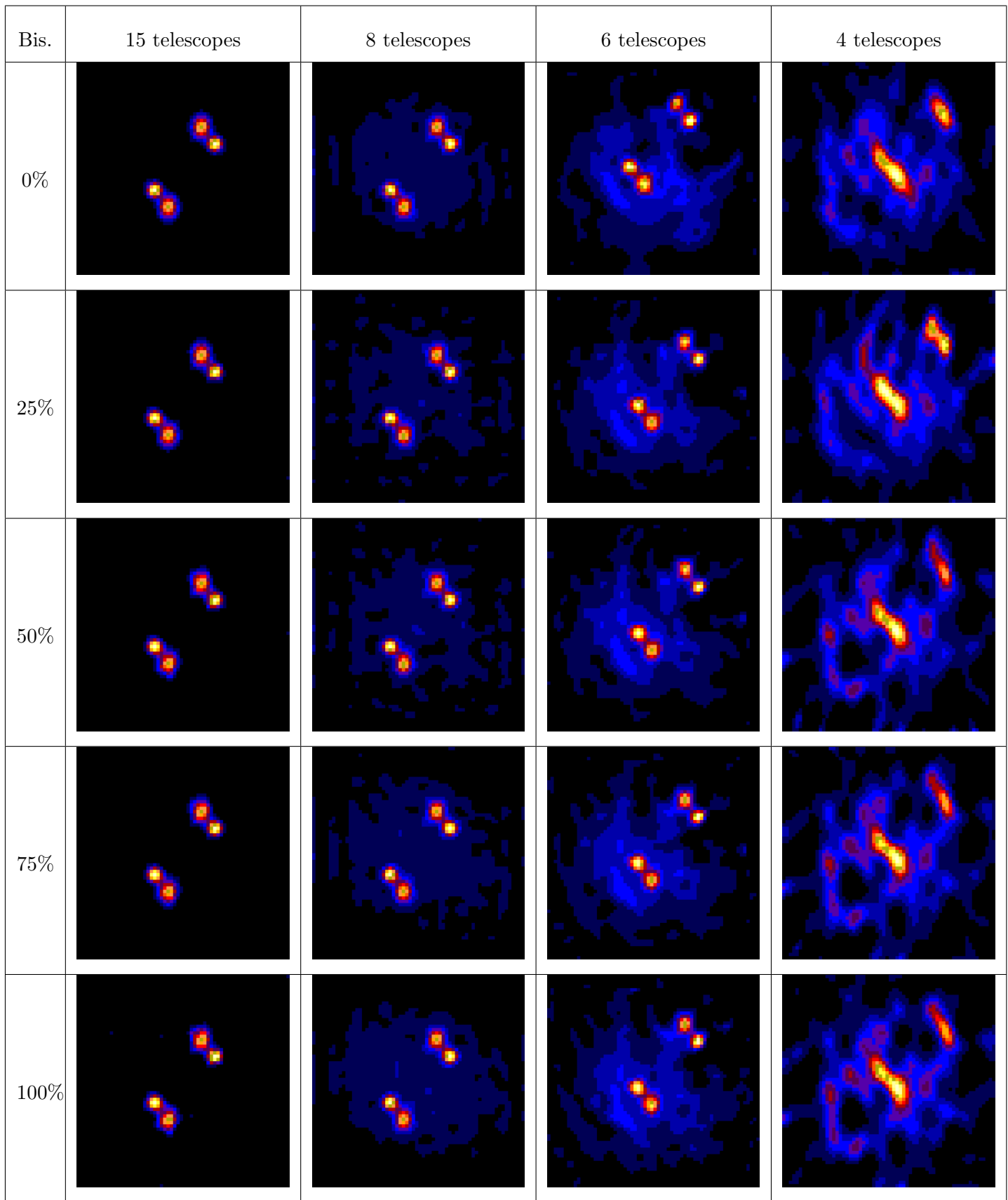
Figure 49: Object 5, high SNR on powerspectrum and low SNR on bispectrum phases.

Bis.	15 telescopes	8 telescopes	6 telescopes	4 telescopes
0%				
25%				
50%				
75%				
100%				
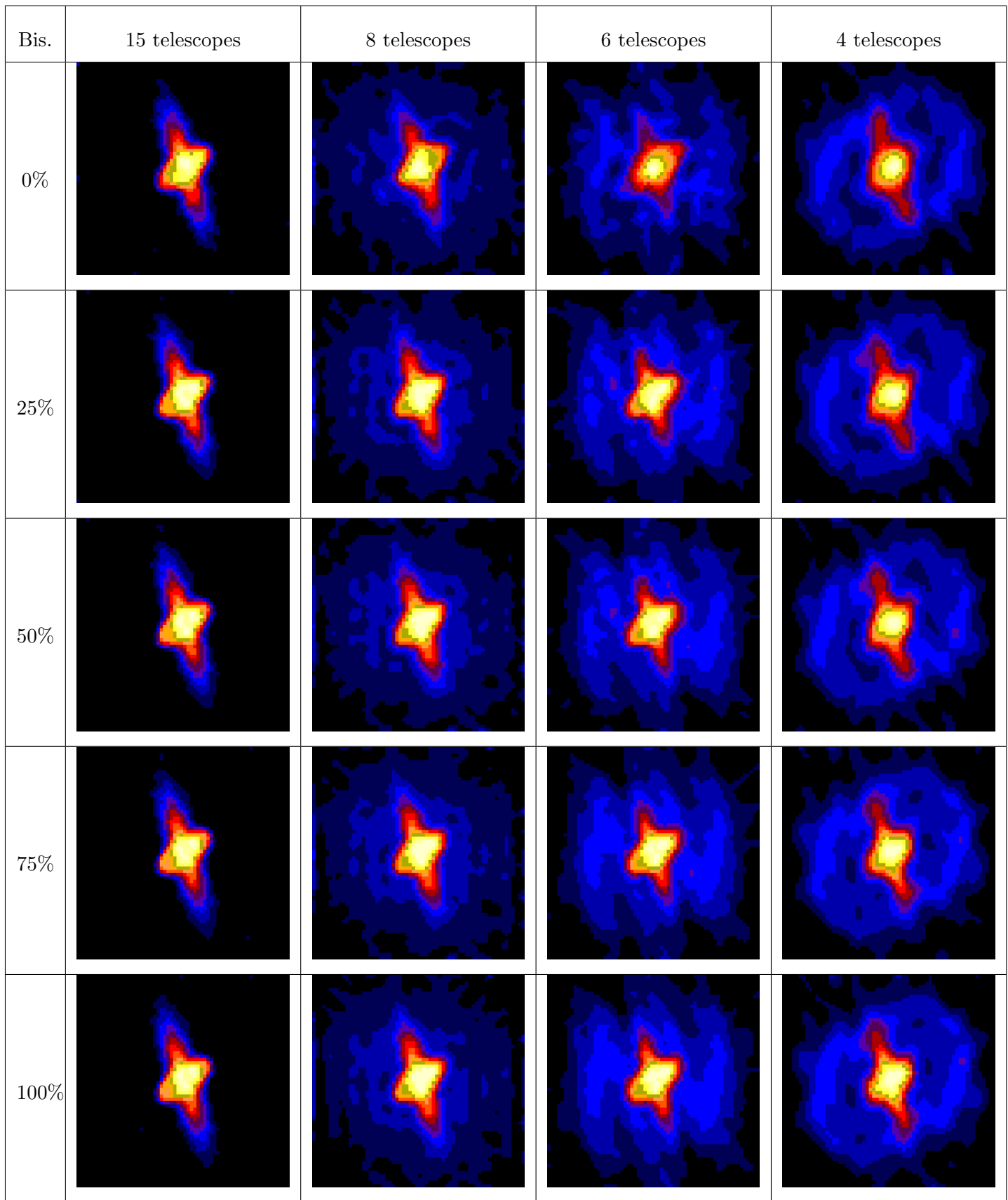
Figure 50: Object 6 at high SNR.

Bis.	15 telescopes	8 telescopes	6 telescopes	4 telescopes
0%				
25%				
50%				
75%				
100%				
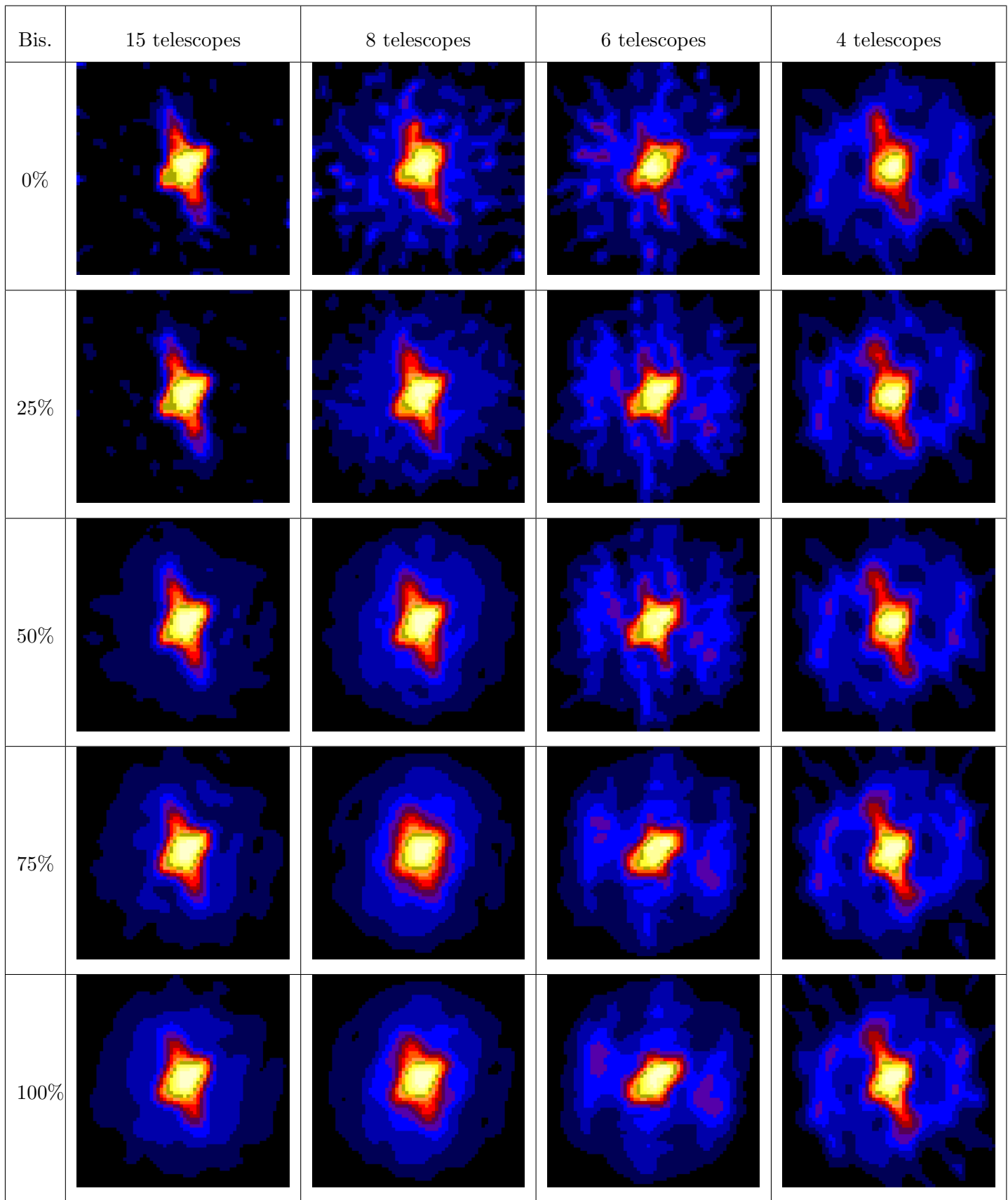
Figure 51: Object 6, low SNR on powerspectrum and high SNR on bispectrum.

Bis.	15 telescopes	8 telescopes	6 telescopes	4 telescopes
0%				
25%				
50%				
75%				
100%				
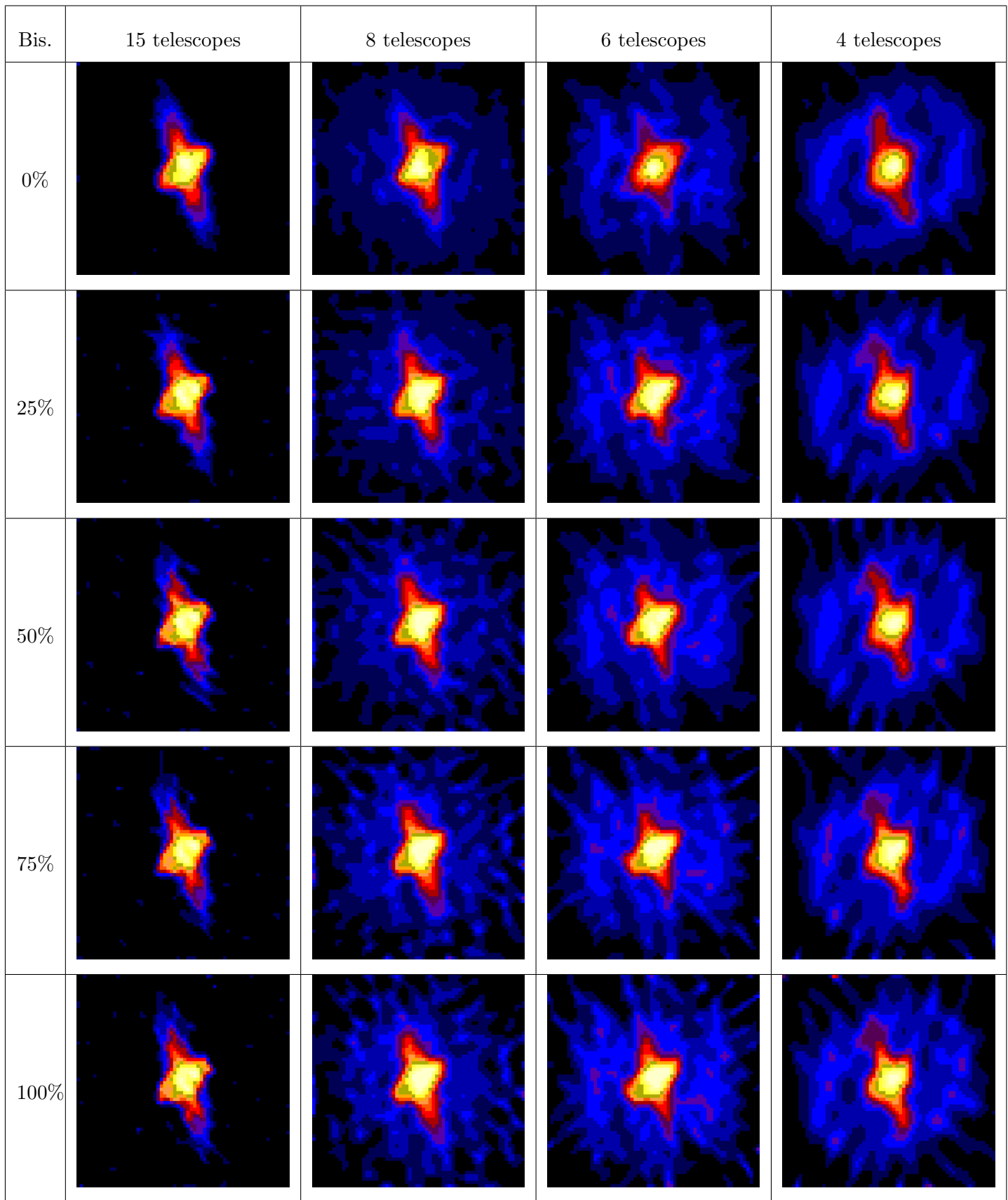
Figure 52: Object 6, high SNR on powerspectrum and low SNR on bispectrum phases.

Pow.	15 telescopes	8 telescopes	6 telescopes	4 telescopes
0%				
25%				
50%				
75%				
100%				
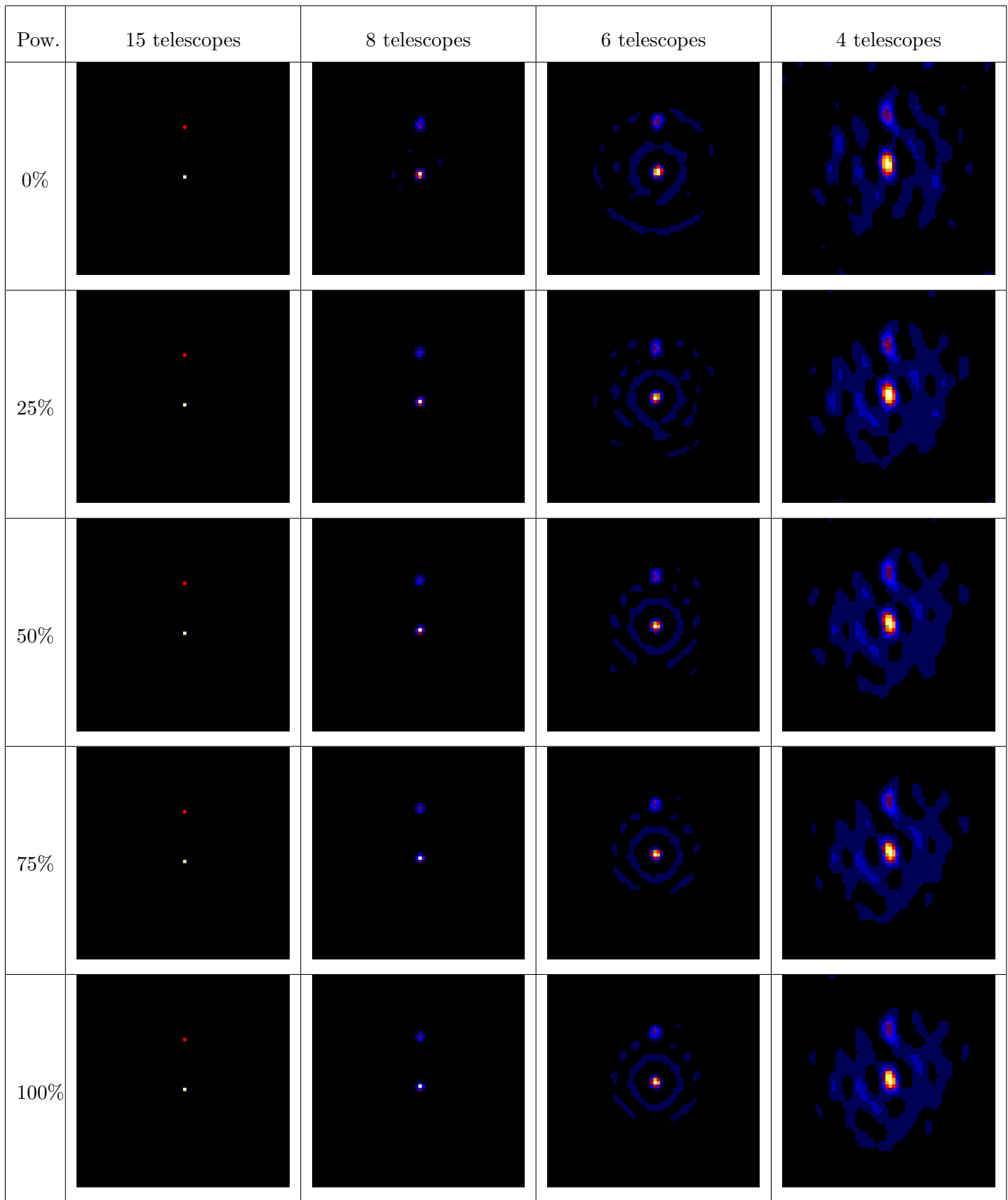
Figure 53: Object 1 at high SNR.

Pow.	15 telescopes	8 telescopes	6 telescopes	4 telescopes
0%				
25%				
50%				
75%				
100%				
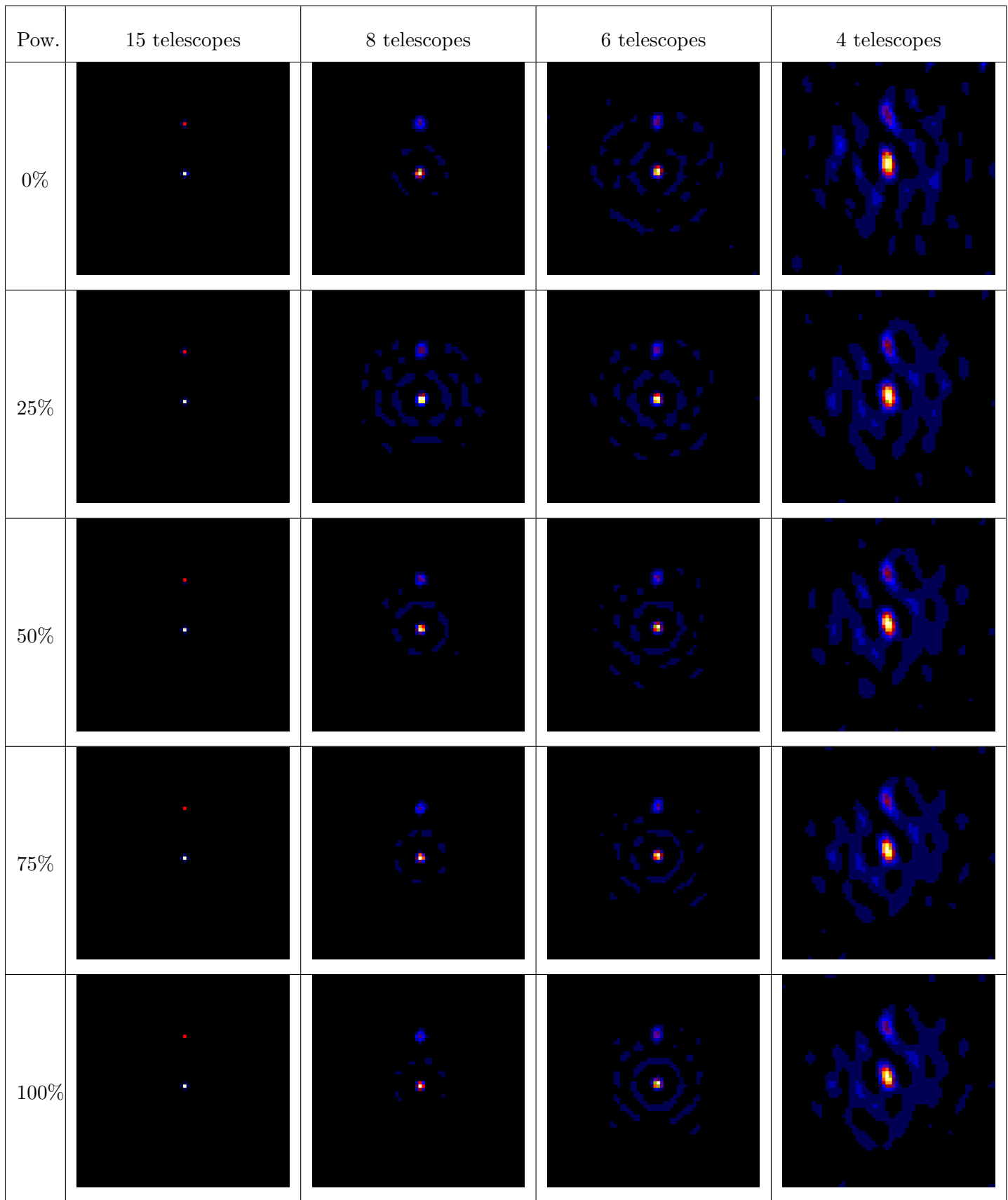
Figure 54: Object 1, low SNR on powerspectrum and high SNR on bispectrum phases.

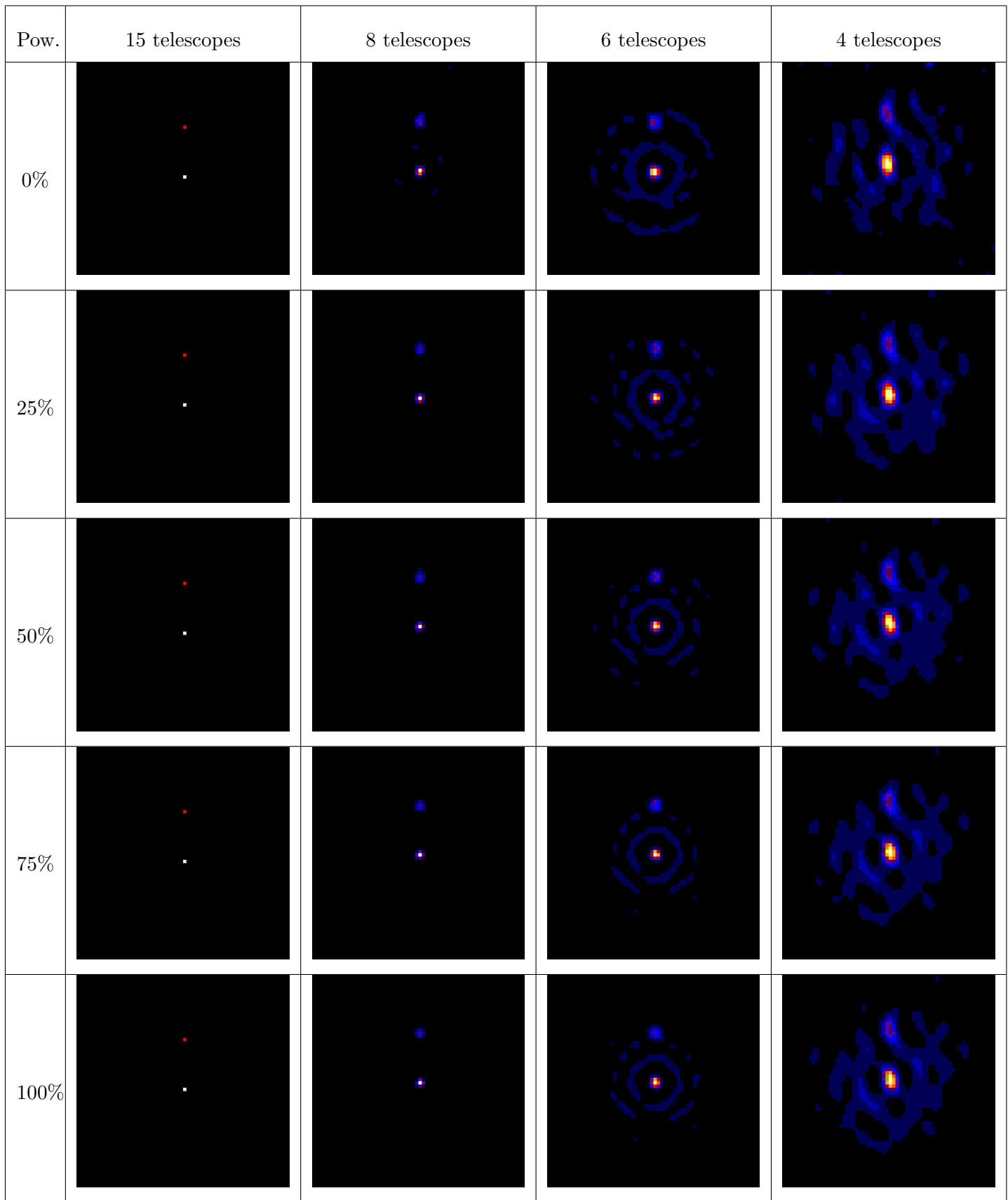| Pow.	15 telescopes	8 telescopes	6 telescopes	4 telescopes
0%				
25%				
50%				
75%				
100%				

Figure 55: Object 1, high SNR on powerspectrum and low SNR on bispectrum phases.

Pow.	15 telescopes	8 telescopes	6 telescopes	4 telescopes
0%				
25%				
50%				
75%				
100%				

Figure 56: Object 2 at high SNR.

Pow.	15 telescopes	8 telescopes	6 telescopes	4 telescopes
0%				
25%				
50%				
75%				
100%				

Figure 57: Object 2, low SNR on powerspectrum and high SNR on bispectrum phases.

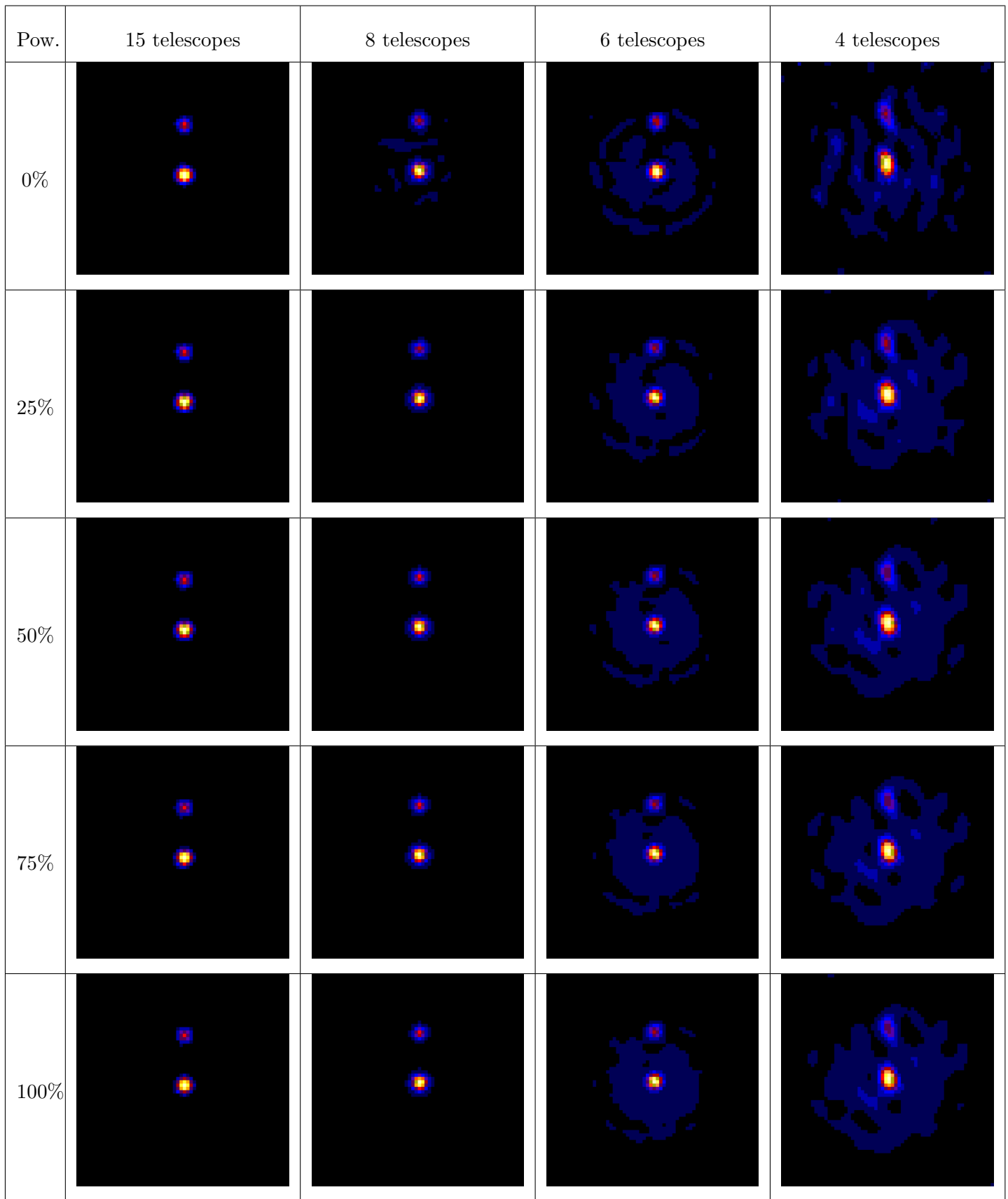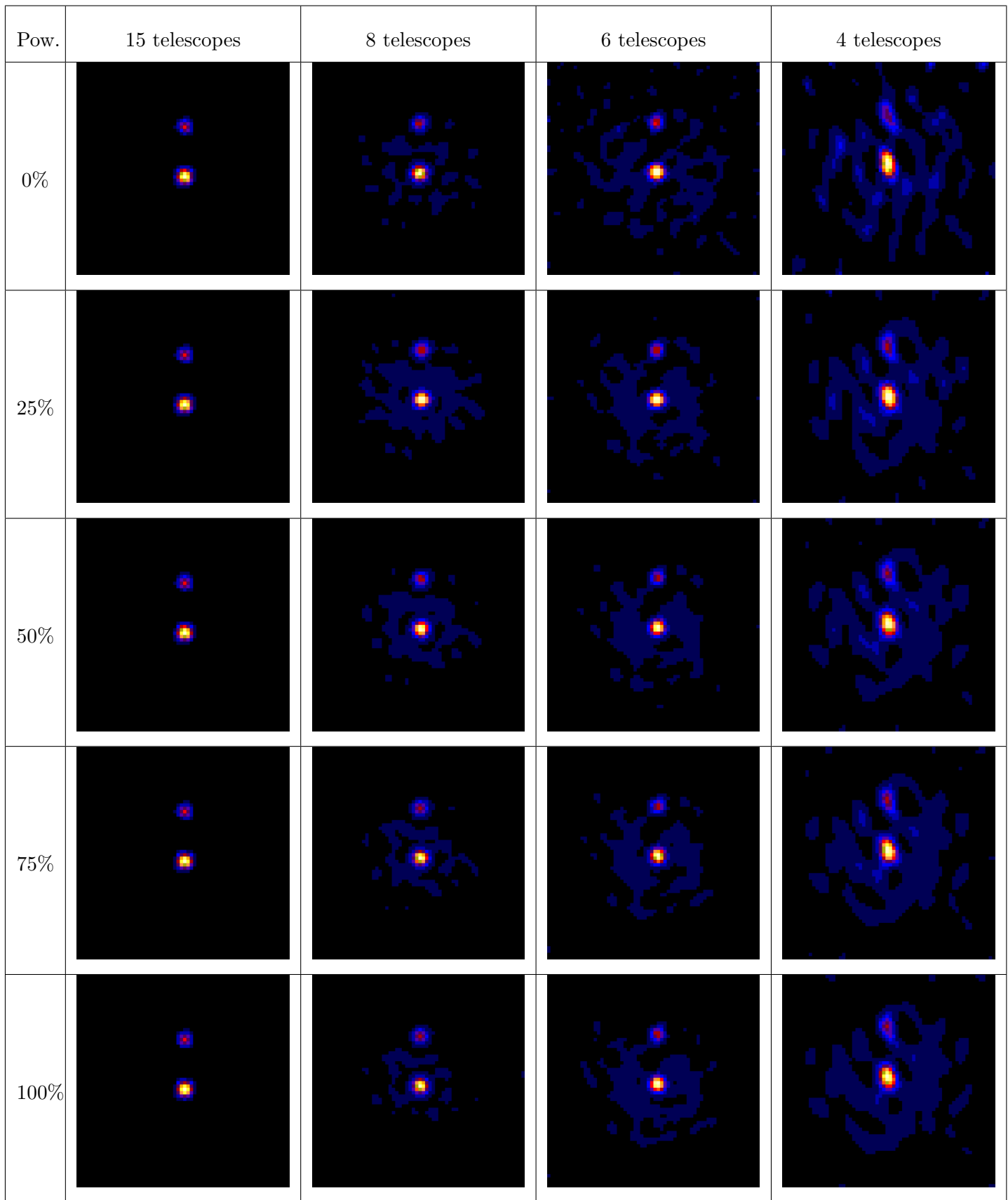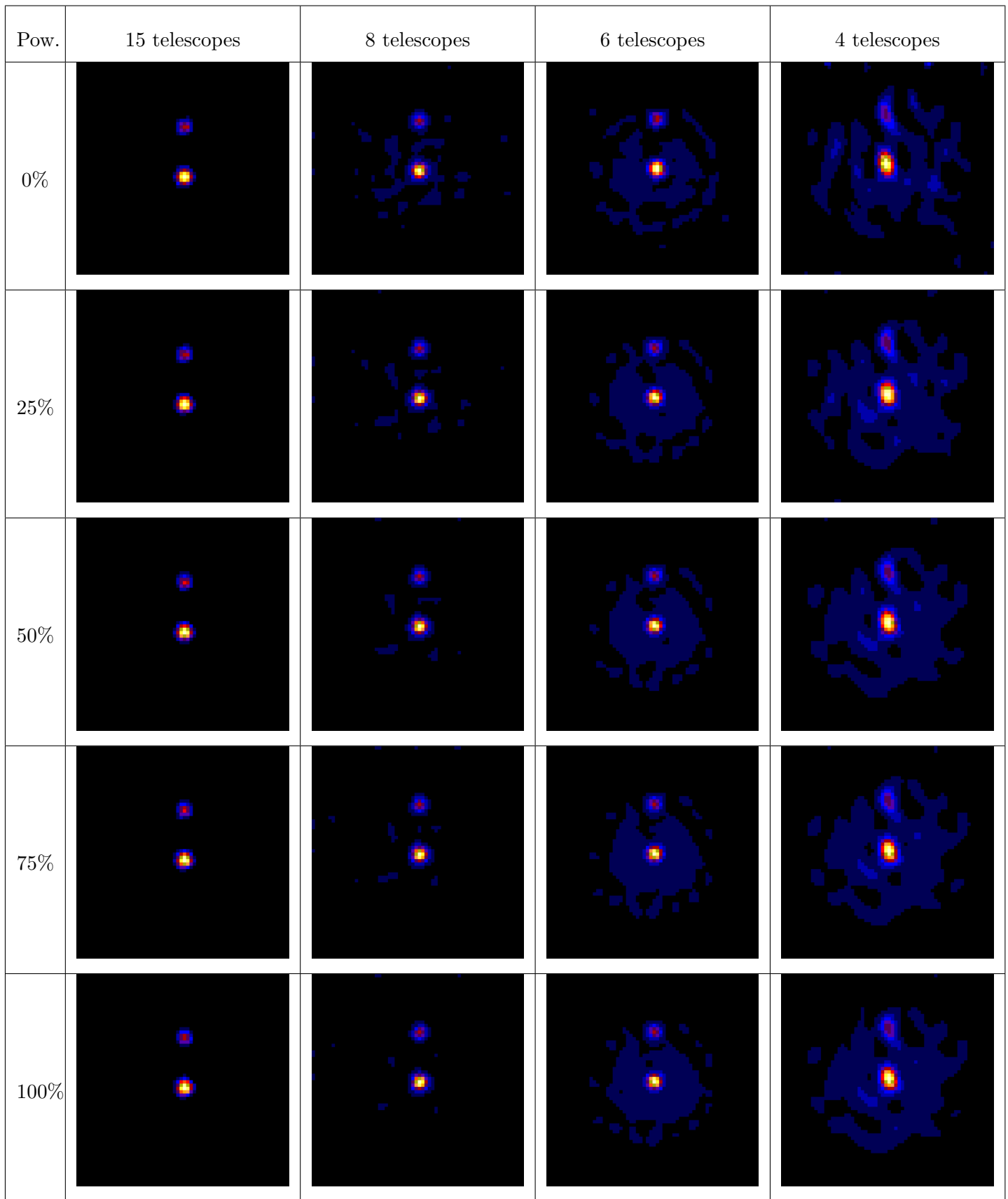Figure 58: Object 2, high SNR on powerspectrum and low SNR on bispectrum phases.

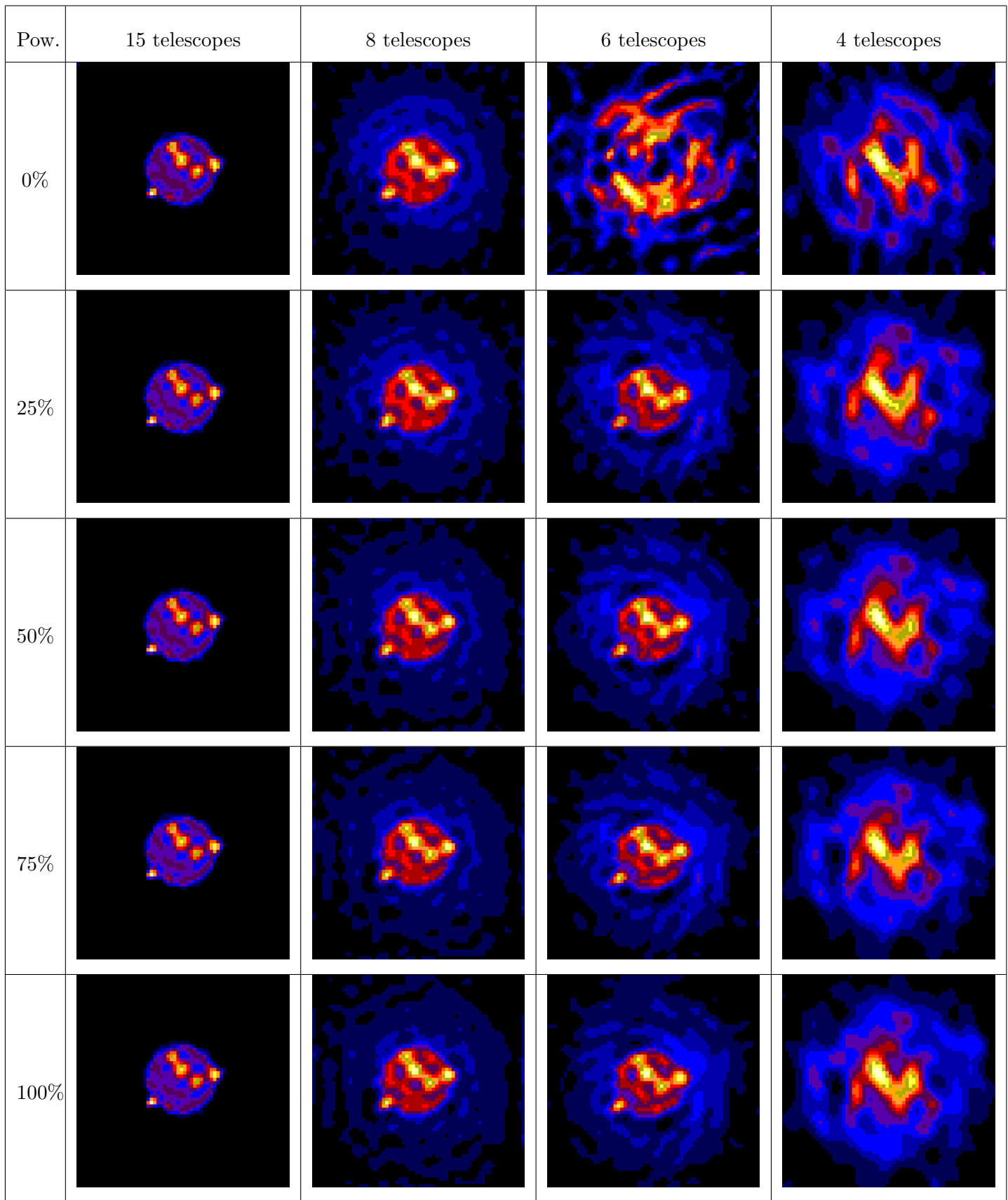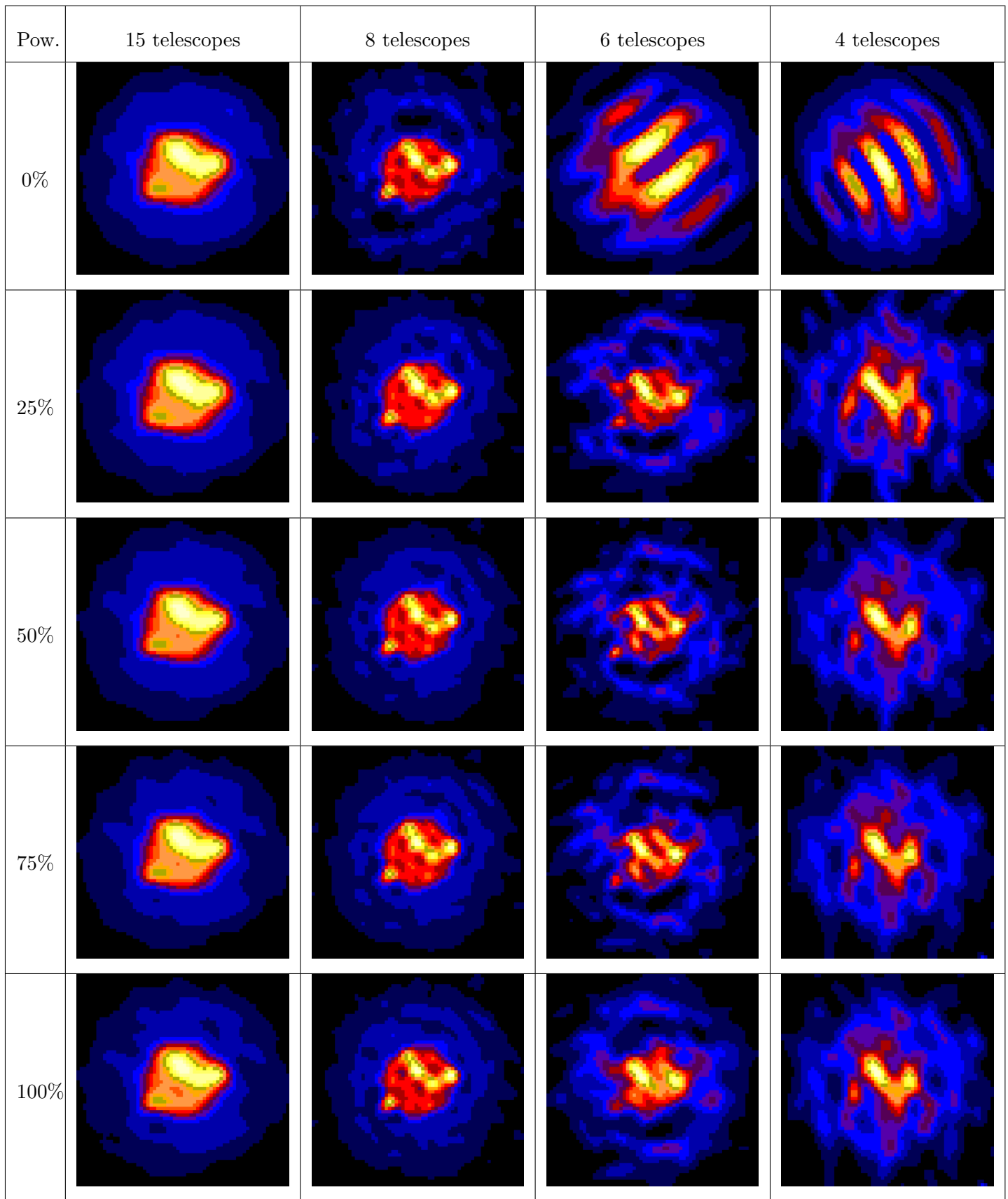| Pow.	15 telescopes	8 telescopes	6 telescopes	4 telescopes
0%				
25%				
50%				
75%				
100%				

Figure 59: Object 3 at high SNR.

Pow.	15 telescopes	8 telescopes	6 telescopes	4 telescopes
0%				
25%				
50%				
75%				
100%				

Figure 60: Object 3, low SNR on powerspectrum and high SNR on bispectrum phases.

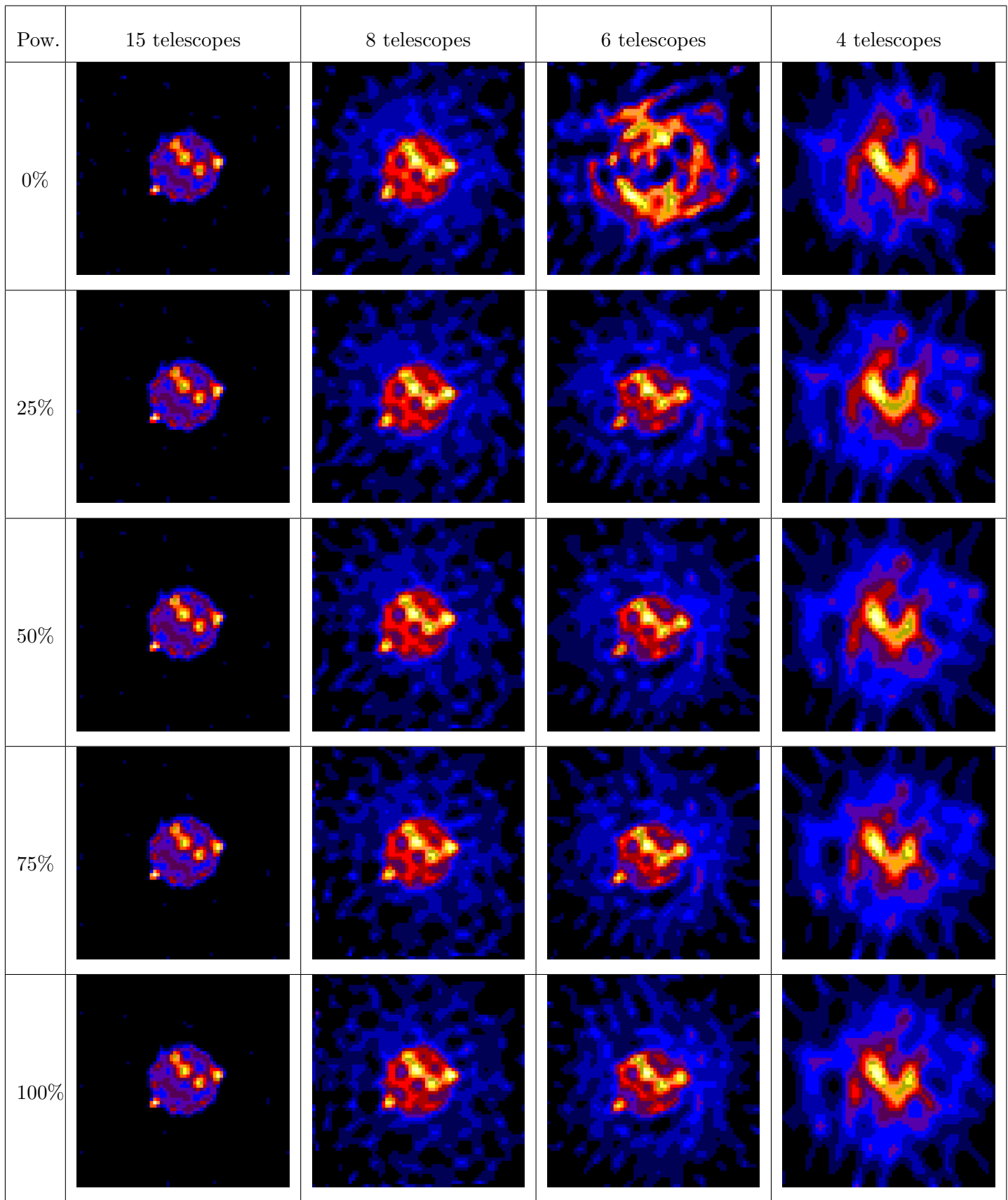| Pow.	15 telescopes	8 telescopes	6 telescopes	4 telescopes
0%				
25%				
50%				
75%				
100%				

Figure 61: Object 3, high SNR on powerspectrum and low SNR on bispectrum phases.
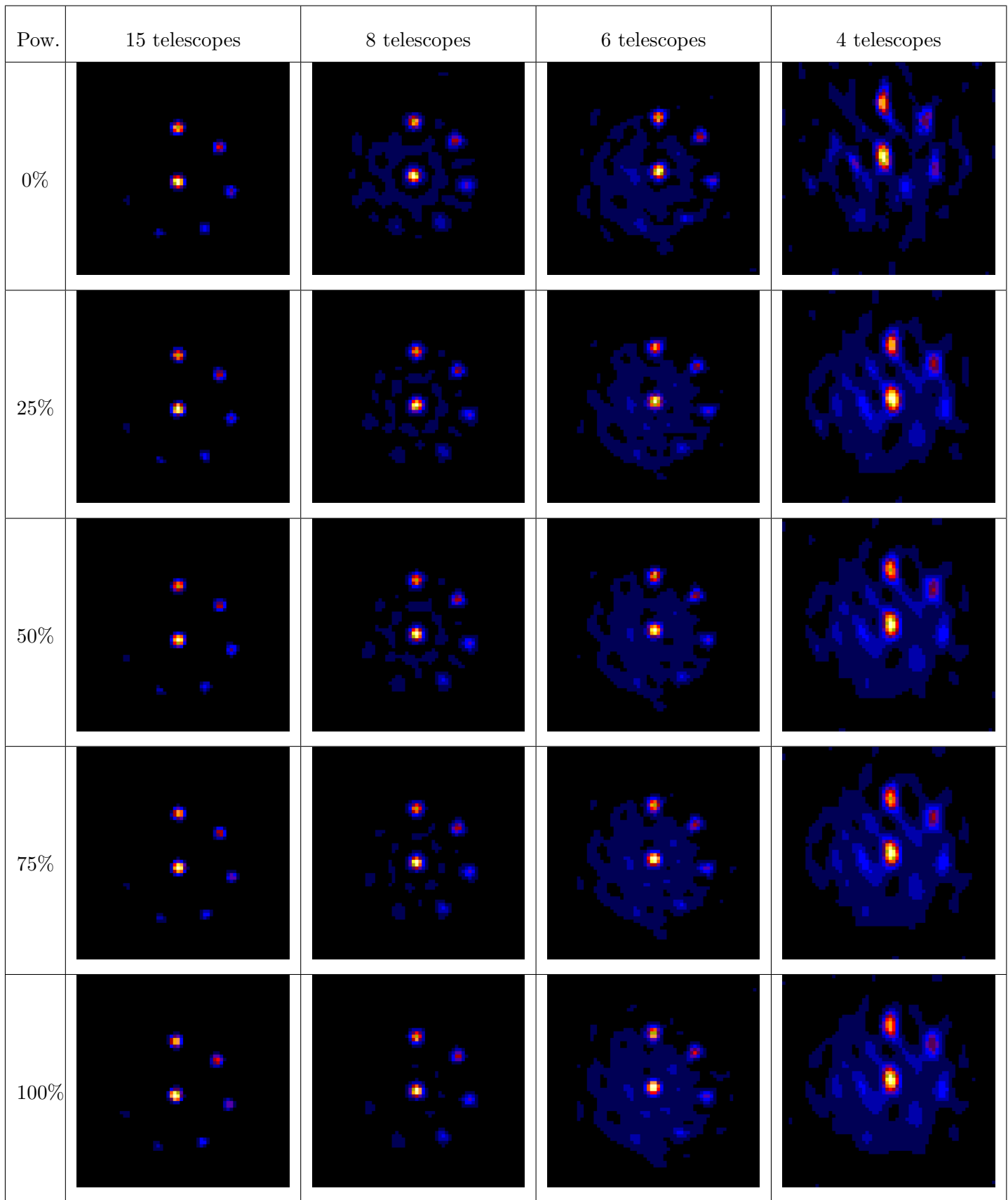
Figure 62: Object 4 at high SNR.

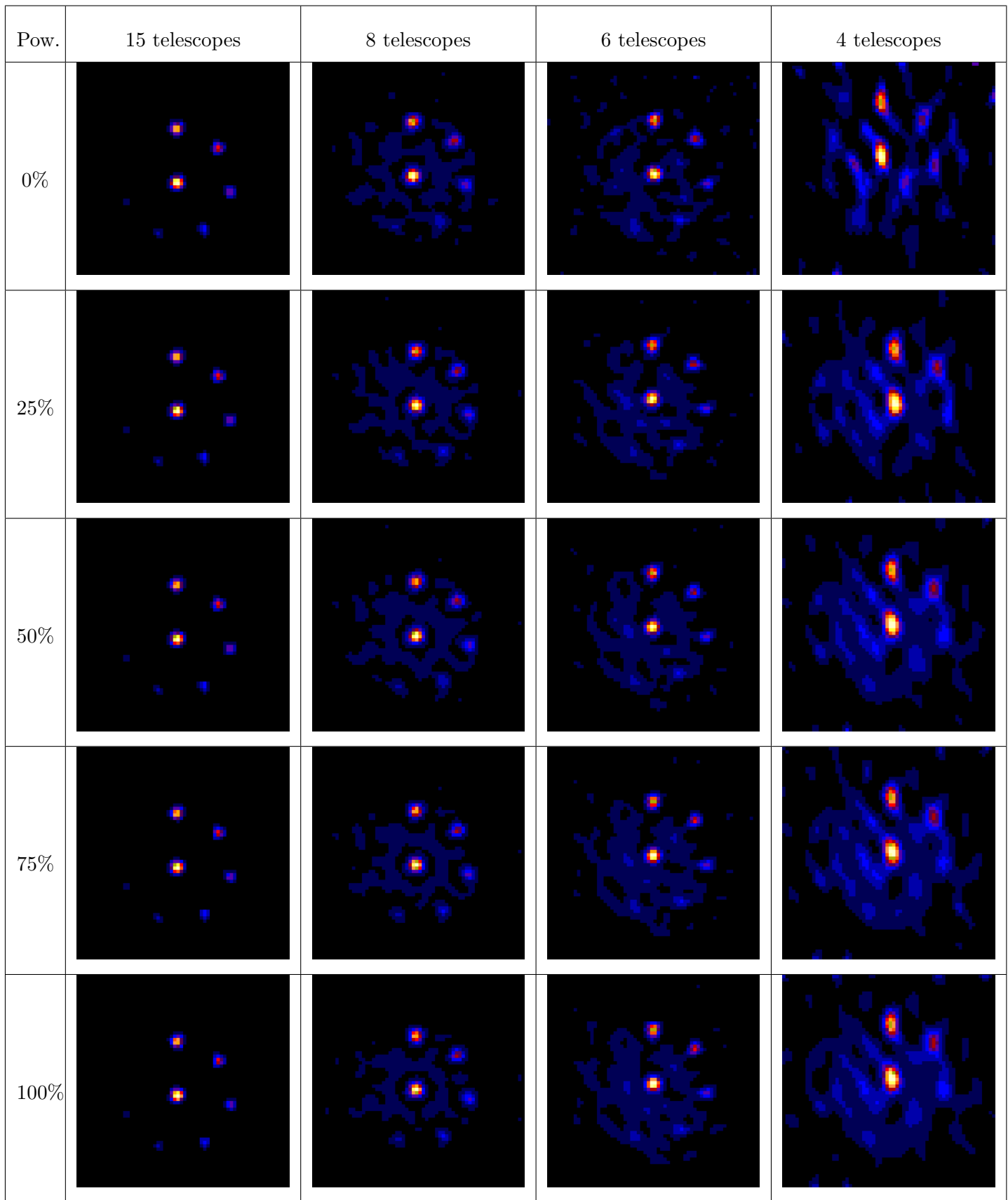| Pow.	15 telescopes	8 telescopes	6 telescopes	4 telescopes
0%				
25%				
50%				
75%				
100%				

Figure 63: Object 4, low SNR on powerspectrum and high SNR on bispectrum phases.

Pow.	15 telescopes	8 telescopes	6 telescopes	4 telescopes
0%				
25%				
50%				
75%				
100%				
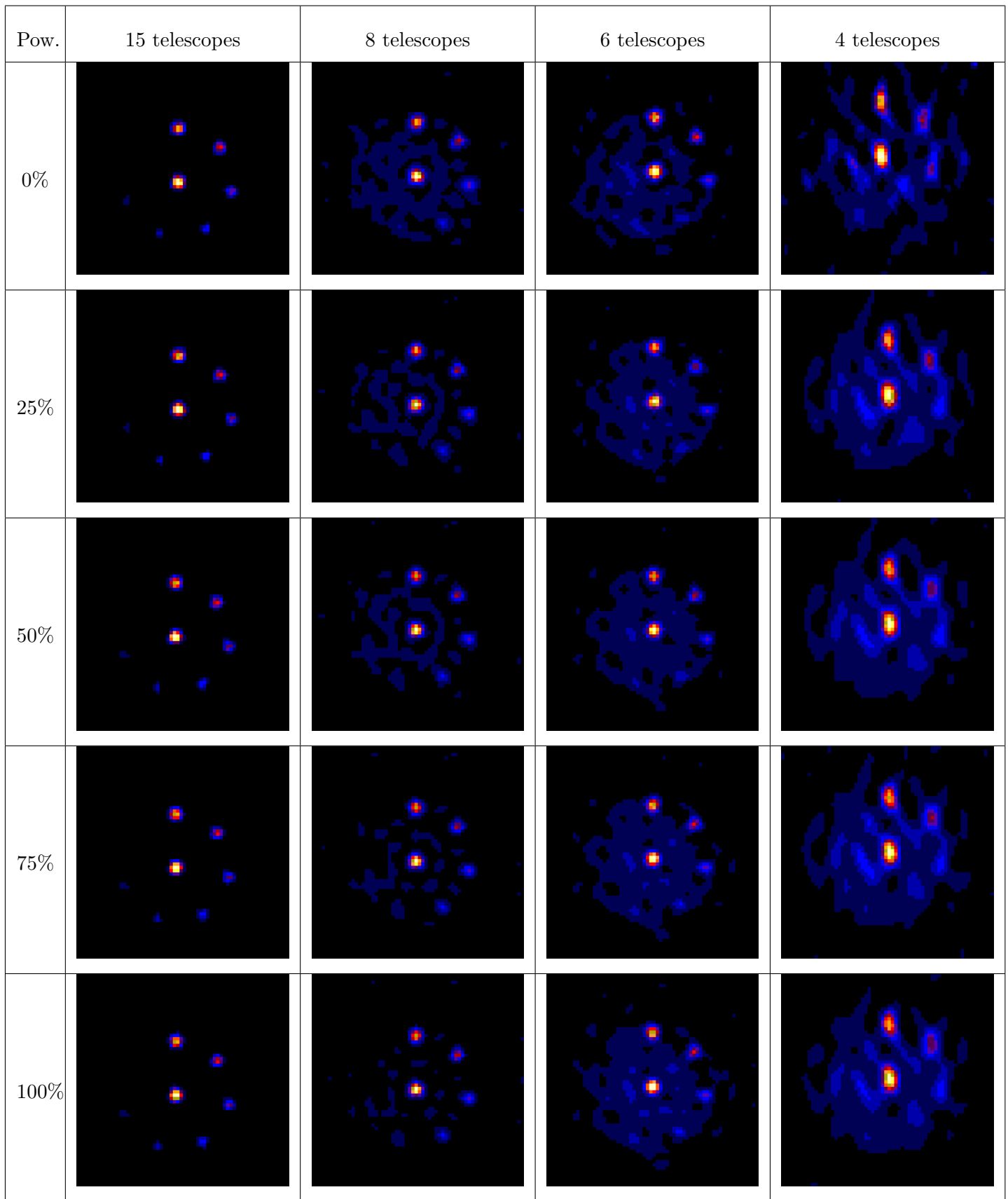
Figure 64: Object 4, high SNR on powerspectrum and low SNR on bispectrum phases.

Pow.	15 telescopes	8 telescopes	6 telescopes	4 telescopes
0%				
25%				
50%				
75%				
100%				
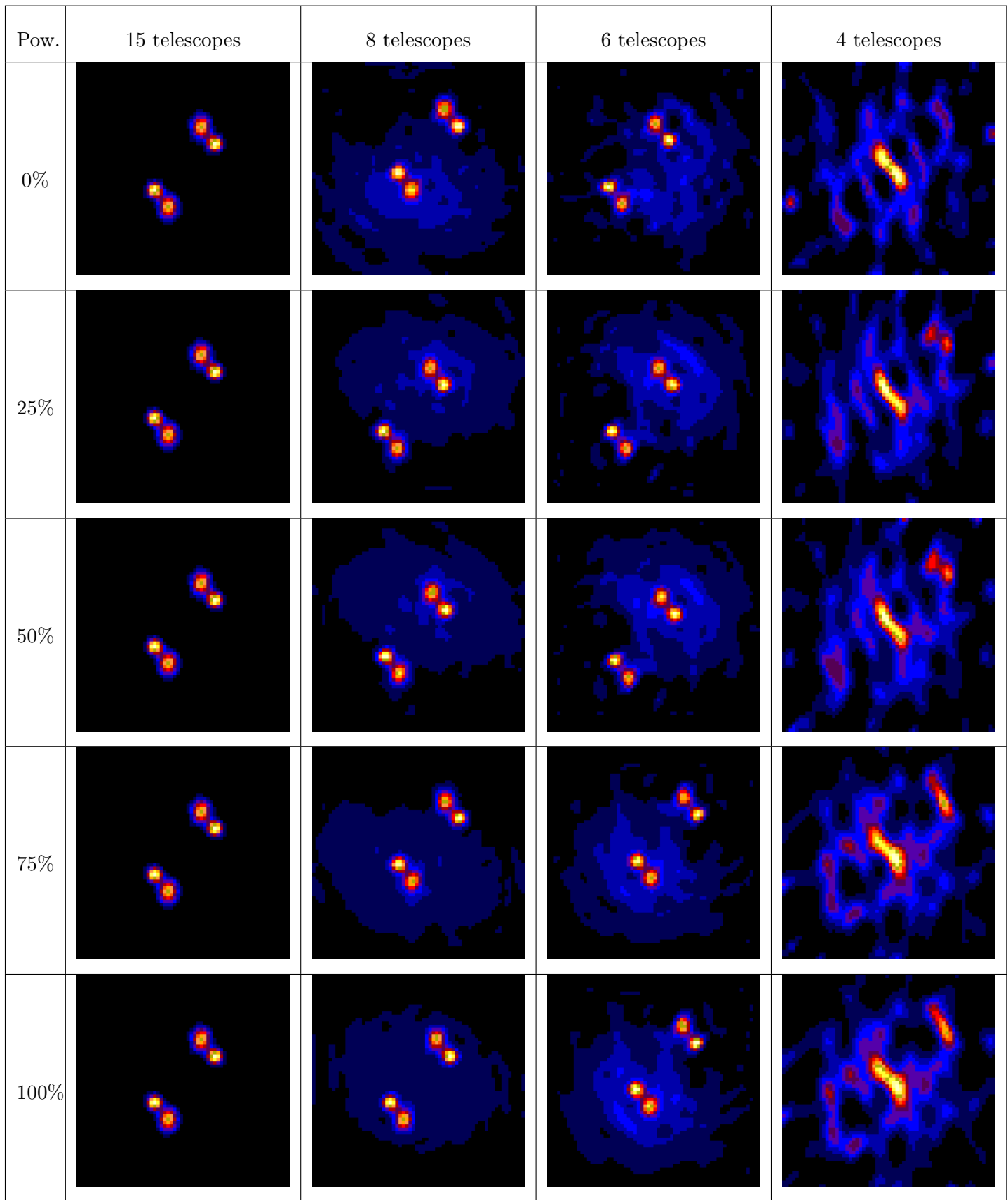
Figure 65: Object 5 at high SNR.

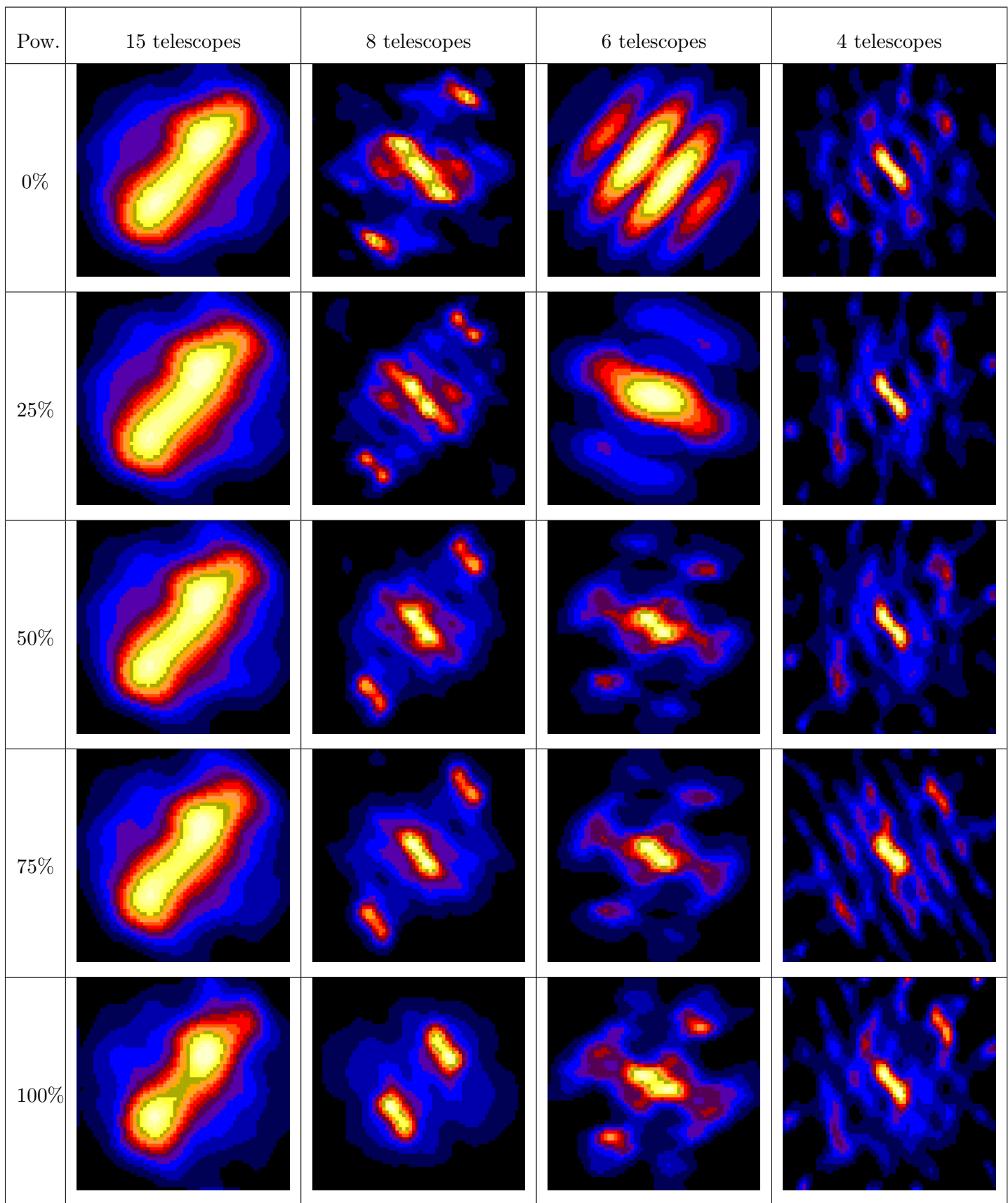| Pow.	15 telescopes	8 telescopes	6 telescopes	4 telescopes
0%				
25%				
50%				
75%				
100%				

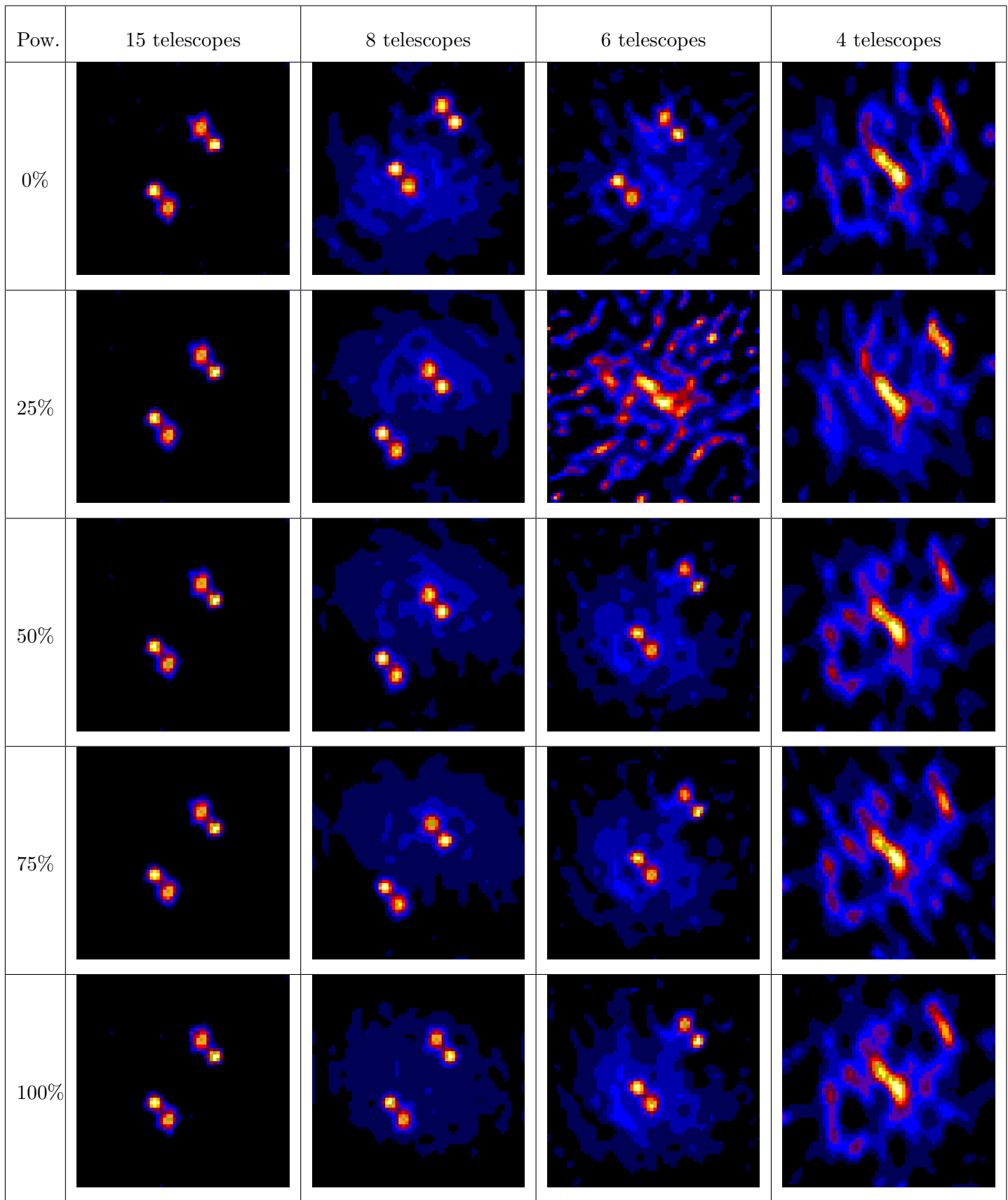Figure 66: Object 5, low SNR on powerspectrum and high SNR on bispectrum phases.

Figure 67: Object 5, high SNR on powerspectrum and low SNR on bispectrum phases.
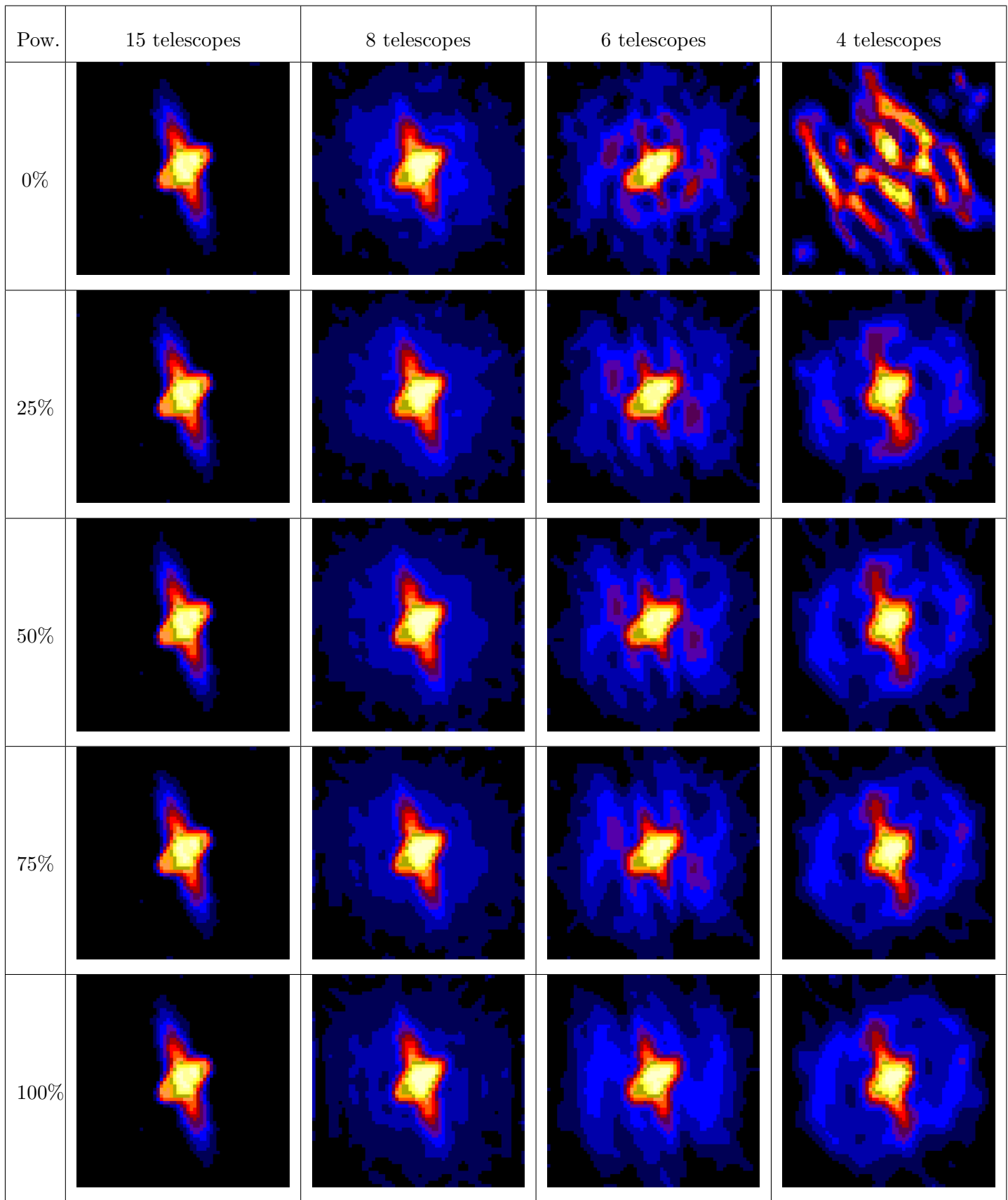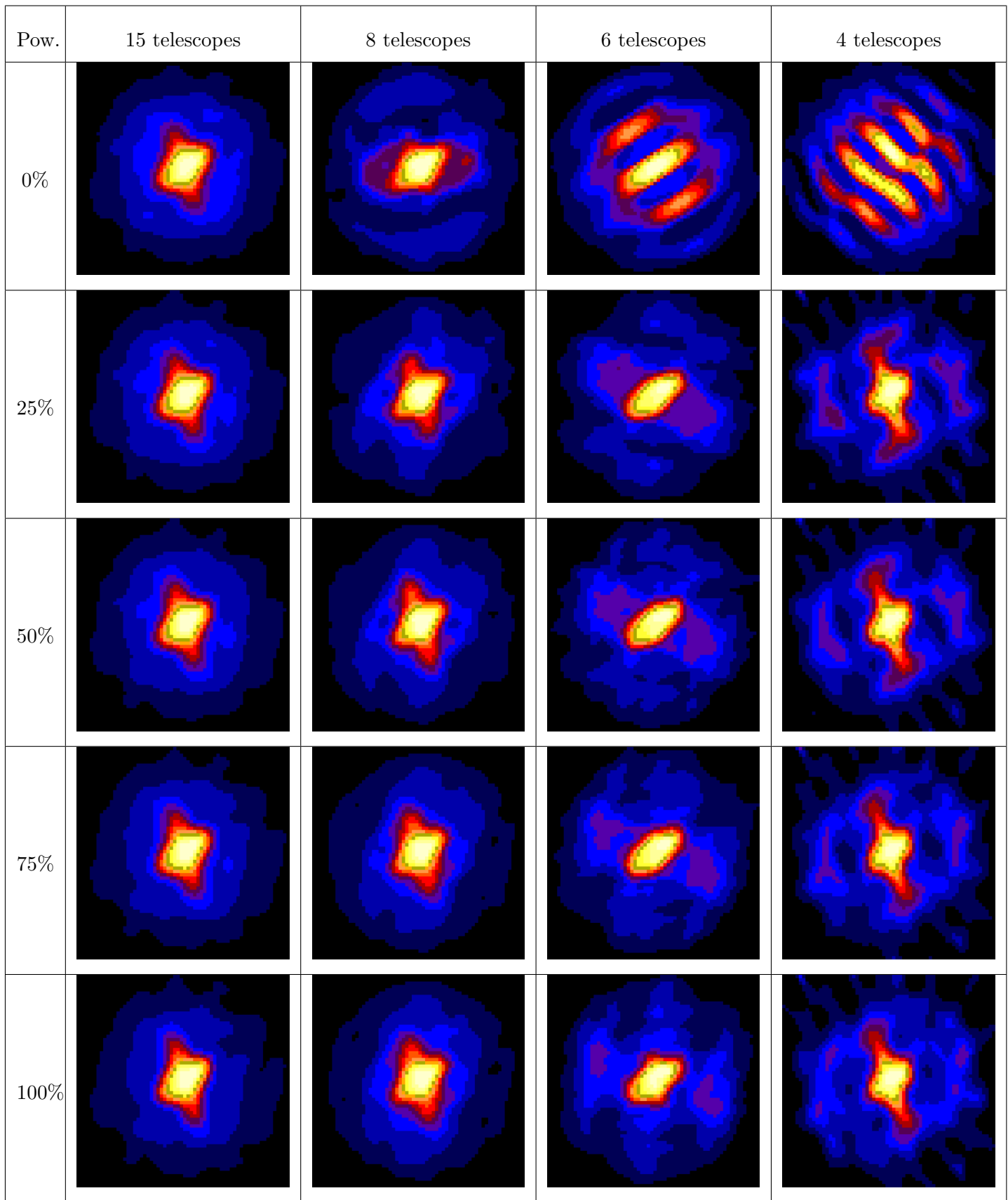
Pow.	15 telescopes	8 telescopes	6 telescopes	4 telescopes
0%				
25%				
50%				
75%				
100%				

Figure 68: Object 6 at high SNR.

Figure 69: Object 6, low SNR on powerspectrum and high SNR on bispectrum phases.

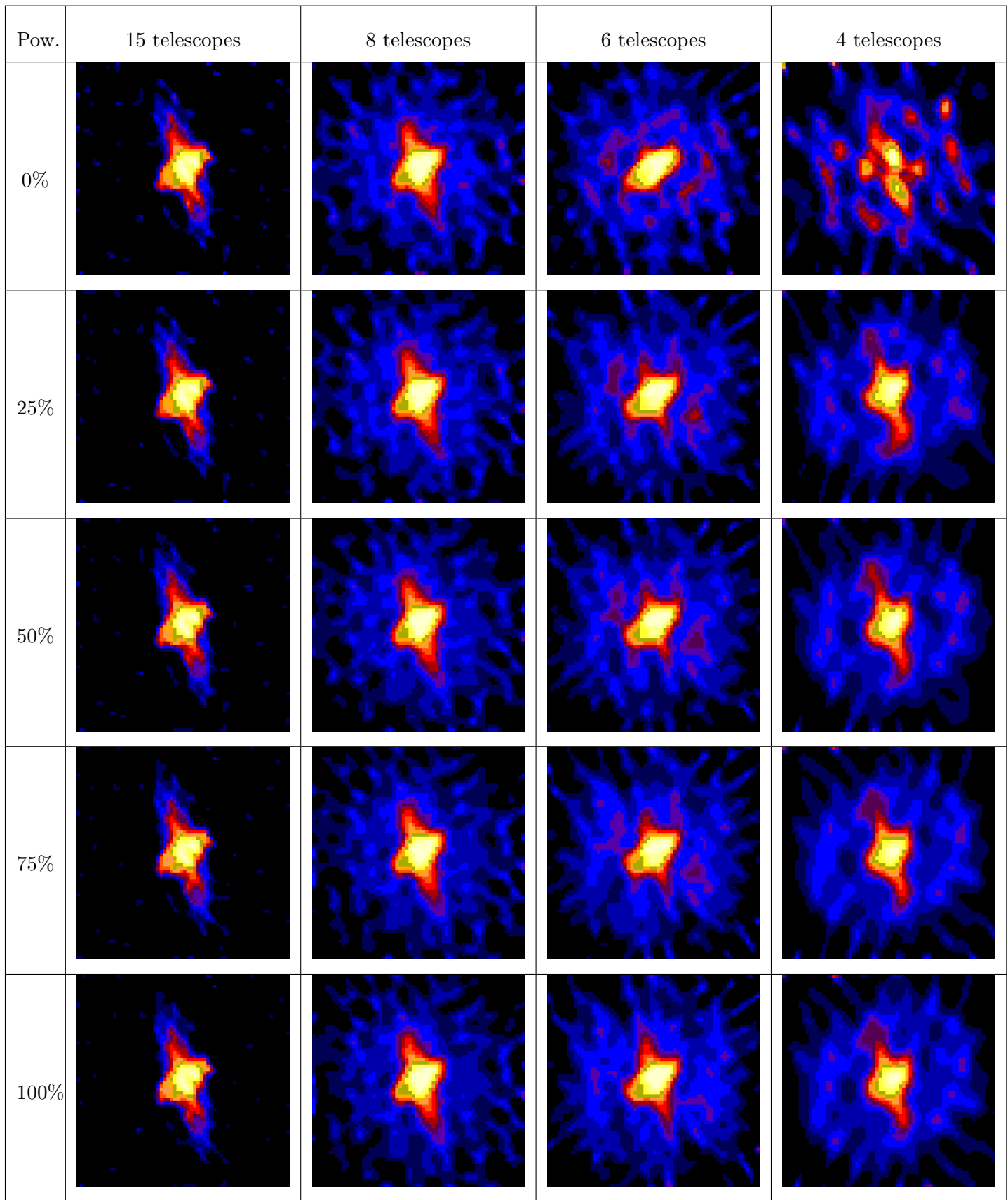| Pow.	15 telescopes	8 telescopes	6 telescopes	4 telescopes
0%				
25%				
50%				
75%				
100%				

Figure 70: Object 6, high SNR on powerspectrum and low SNR on bispectrum phases.

4.3 Influence of entropy method

MEMSYS allows the use of several different entropy methods, which we have reviewed to help the user decide which one is appropriate for a data set of known characteristics.

MEMSYS methods consist of the following ones:

- Method 1: the classic automatic method. This is the default entropy method used by BSMEM;

- Method 2: the classic automatic method with noise scaling, meant to be used when the noise on experimental data is uncertain. This method work well with large datasets only.

- Method 3: the historic entropy method, which tends to give very smooth reconstructed images, and is not advised in the general case.

Detailed explanation of the statistical rationale behind these methods are beyond the scope of this document and can be found in the MEMSYS5 library user manual [1].

Figure 71 shows a representative comparison of all three methods for object 3 and object 4 at different noise levels (noise on visibility amplitudes was used here, but the same behaviour can be observed when using noise on phase).

4.3.1 Performance analysis

When analysing the reconstruction error behaviour on Object 3, Method 1 shows the best performance, as it converges to the solution for high to low SNR data sets (from 10^{-4} to 10^{-2}). Method 2 gives excellent results on the highest SNR data, perhaps even slightly better than those method 1 is able to achieve. However, it proves to be unable to converge for mid-SNR data sets ($> 2.10^{-3}$). Still on Object 1, Method 3 is probably the most robust method as it can still give decent results on some low SNR data sets (at 3.10^{-2}), but the improvement over Method 1 is minor at most.

These results are confirmed on Object 4, where Method 1 and Method 3 give nearly identical results. Again either Method 2 easily converges to the solution or it stays too close to the model.

Additional information is given by repeatability graphs (on the right), showing that overall Method 2 has the best repeatability among all three methods, while Method 3 is the worse contender and Method 1 is in the middle-ground. This proves the user can be confident in Method 2's results when it manages to converge.

4.3.2 Speed issues

Method 1 and 2 are generally very fast, converging in less than 200 iterations in an average case with medium SNR data points. The whole process is on the order of a few tens of seconds.

The actual time taken by a single iteration is much shorter for Method 3 but this advantage is counterbalanced by the greater number of iterations needed to converge to the solution. Overall this makes Method 3 the slowest of all three methods.

4.3.3 Conclusion on entropy methods

When trying a reconstruction on an unknown object for the first time, the BSMEM user has two choices:

- choose method 1 as a general rule, as it offers good performance without major drawback ;

- as an alternative, use method 3 to get a coarse estimate of the reconstructed image as it can give the best image at low SNR. Then use this estimate as a starting model in a reconstruction by method 1 or even method 2 for high SNR cases.

It should be noted that Method 1 was used for all previous tests in this report, as it gives a fair view of BSMEM performance. It is also probably the solution a new user would select most of the time.
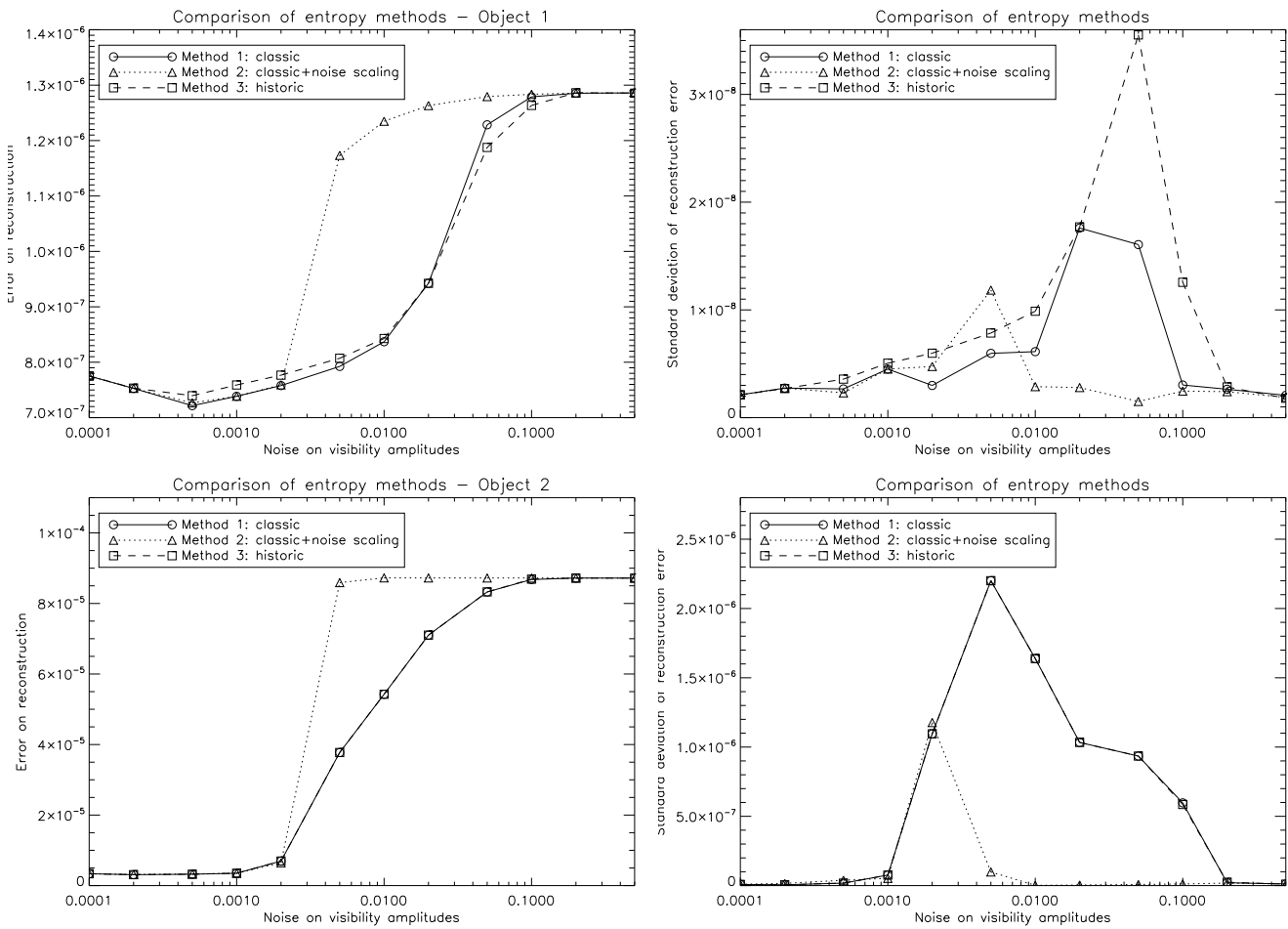
Figure 71: Comparison of entropy methods for object 1 (top) and object 2 (bottom). For each object, there were 100 noise occurrences per point.

4.4 Influence of the prior choice

It may seem strange to have a model-independent software which still uses a model for initialisation. The default BSMEM prior is a Gaussian centred in the field of view and of adjustable size, and the user can also use a flat prior or a custom one. As BSMEM was developed with model-independent reconstruction in mind, the success of a reconstruction rarely depends on the choice of the prior shape. In practise the choice of prior only influences the converging process and its speed. The flat prior do not introduce information and thus is generally preferred when the object is totally unknown. Custom priors, which have not been used for the creation of this report, allow to partially compensate for MEM difficulties when reconstructing extended objects that contain point sources, by creating models that emphasises chosen parts of the image.

Gaussian priors are interesting for two reasons:

- the centre of the image reconstructed from bispectrum and powerspectrum is not fixed, i.e. the translated image is also optimal in the Bayesian sense. To avoid border effects, it is better to force the position of the structures to reconstruct by imposing a Gaussian.

- one generally tries to reconstruct compact structures. If an estimate of the structure extension is known beforehand, using a Gaussian prior is more efficient.

However as the prior behaves like a weighting function, the domain on which the Gaussian prior is non zero should always be larger than the object to be reconstructed. If not, a zero weight would be assigned to pixels which should actually be non-zeros : this can sometimes prevent MEM from converging, or at least slow the converging process. This problem is due to the Gull and Skilling entropy function, and the fact that entropic reconstruction does not behave correctly at zero value points. Note also that in order to avoid border effects, it is wise to adjust the Gaussian prior so that is does not extend outside the field of view.

Priors are only truly required in BSMEM when time is a constraint. The larger the reconstructed image, the longer each iteration will take, and the lower the SNR, the more iteration will be needed to converge. Thus when trying to reconstruct large images from poor data (a typical case would be the Beauty Contest 2006 test object), the converging speed can become an issue and so does the choice of prior. To conclude, the actual performance do not change between adequate priors, but the converging speed can be greatly enhanced with a non-flat one.

5 Conclusion and future of BSMEM reconstruction

The main conclusion of this report is that reconstruction with a small number of stations is difficult but still possible. A 4 telescope array is sufficient for the simplest targets, and a 6 telescope one will generally produce good quality images even with trickier sources. The *uv* coverage and bispectrum acquisition scheme are of course of primary importance for actual performance of model-independent reconstructions, and the development of future facilities with more capabilities in these regards open new fields of possibilities for imaging.

The reader interested by more details on BSMEM internals can directly contact the author of this report at baron@mrao.cam.ac.uk. Additional simulations and interpretations on BSMEM behaviour and on image reconstruction with bispectrum in general can also be found in H. Thorsteinston's paper [5].

Future developments on BSMEM will include:

- a practical and portable Graphical User Interface and a revised makefile system;

- a multi-wavelength reconstruction capability;

- other algorithm improvements if possible : improved entropy function, bi-model point source/extended object, faster minimisation method.

Finally using BSMEM is free for academic use but requires to a license from Maximum Entropy Data Consultants Ltd (www.maxent.co.uk). It is our hope that the user-base will grow, so that feedback from the users would allow us to further improve BSMEM.

Acknowledgements